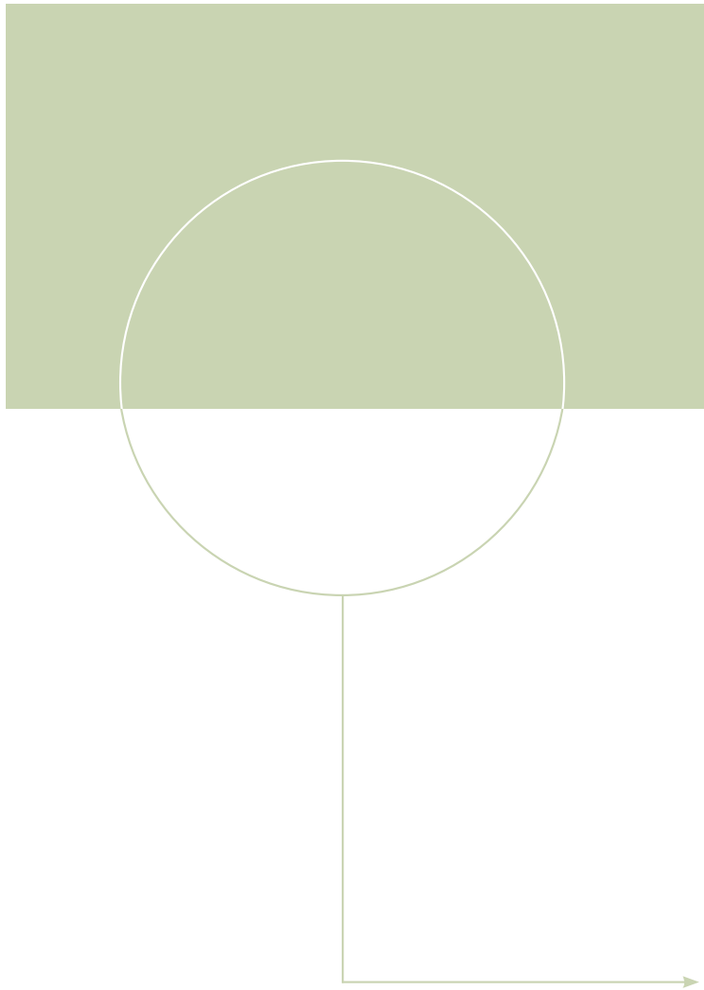

Master's thesis

2019

Lars Rudolfsen

NTNU
Norwegian University of
Science and Technology
Faculty of Information Technology and Electrical
Engineering
Department of Engineering Cybernetics

Lars Rudolfsen

Numerical Realization of Fractional Eddy Current Dynamics

June 2019

NTNU
Norwegian University of
Science and Technology

NTNU
Norwegian University of
Science and Technology

NTNU
Norwegian University of
Science and Technology

Numerical Realization of Fractional Eddy Current Dynamics

Lars Rudolfsen

Master of Science in Cybernetics and Robotics
Submission date: June 2019
Supervisor: Morten Dinhoff Pedersen

Norwegian University of Science and Technology
Department of Engineering Cybernetics

Preface

The thesis supervisor contributed with:

- Developing the *Fractional Electromagnetic Theory* (FET) and formalizing its application to magnetic damping
- Advice and assistance regarding its implementation
- Guidance and discussion along the way
- Proof reading of the final report

The candidate contributed with:

- Realizing the FET numerically
- Case study of its application to *Eddy Current Brakes* (ECBs)
- Validation and verification of the numerical solution
- Evaluation of the numerical method
- Analysis of the dynamical ECB model
- Presentation and discussion of findings and their physical implications
- Implementation of state of the art control algorithms
- Considerations on the applicability of the model and numerical method to engineering applications

Summary

This thesis investigates the formulation of the eddy current phenomenon in thin geometries as a set of two-dimensional fractional diffusion equations in the plane, and how they describe an eddy current braking system. Involved in this is a comprehensive study of the previous work done on analytical modelling of eddy current induction and resulting forces in thin conductive sheets of infinite extent. Furthermore, the spectral method of solving differential equations, extended to the two-dimensional problem in question was successfully implemented to yield a surprisingly accurate numerical realization of an eddy current braking system. The resulting dynamical model for the ECB forces is a novel result, and is examined in detail.

Sammendrag

Denne avhandlingen undersøker de to-dimensjonale fractional diffusion likningene som kan brukes til å beskrive dynamikken til induserte virvelstrømmer i et tynt, strømledende flak som strekker seg uendelig langt ut i planet, og hvordan disse beskriver et virvelstrømbremsesystem. Dette inkluderer et omfattende literaturstudie av eksisterende fremgangsmåter for matematisk modellering av virvelstrømmer og resulterende bremsekraft. Den numeriske løsningsmetoden som ble brukt tilsvarer en to-dimensjonal fouriertransformasjon, og ga et overraskende nøyaktig resultat. Den resulterende dynamiske modellen for en virvelstrømbrems er et nytt resultat, og blir undersøkt i detalj.

Contents

List of Figures

List of Tables

Chapter 1

Introduction

Eddy current induction, given its name for the fluid-like circulating return paths that are formed, has historically been associated with energy losses in the magnetic cores of voltage transformers due to a relative movement between the inductor and core. While often unwanted in electrical systems, there are ways to exploit the energy dissipation of this process for kinetic electro-mechanical systems. Its most common application is *magnetic braking*, in which the relative movement of a conductive body and a magnetic field lead to a dissipation of the kinetic energy.

Contactless magnetic braking systems, or *Eddy Current Brakes* (ECBs), are commonly used in vehicular braking as a supplement to hydraulic brakes for their superior performance in high speed applications. ECBs themselves have no holding force, and are therefore not suitable as the only braking mechanism, but provide excellent resistance for bodies in motion. Applications for ECB technology are not limited to vehicles, however. A major area of use is in resistive torque generation for rotating conductors, which has applications within exercise equipment, hoisting of heavy loads, to name a few.

The impressive railway systems of magnetically levitating trains, currently operational in a number of Asian countries, are largely based on this technology. Alignment, levitation, braking and propulsion of the vessel are all achieved through the use of eddy current induction. Complex engineering applications of the eddy current phenomenon such as this require state of the art mathematical modeling and control algorithms. Currently, these disciplines are very much split. Accurate mathematical models of the process generally require time consuming numerical solutions, making them suited for analysis and not real-time applications. Conversely, the absence of sufficiently accurate models that can be implemented in real-time forces the use of approximate models and robust control methods.

1.1 Research Approach

Main Topics

The most significant research topics of this thesis is given by the following set of questions to answer:

1. *What is the FET, and how is the dynamical ECB model derived?*
2. *Can the numerical realization be validated and/or verified? What are its limitations?*
    - Does the numerical solution agree with established results on ECBs?
    - Which factors are significant for its accuracy?
3. *If the implementation is valid, what are its merits?*
    - What can it tell us about the ECB process that approximate models cannot?
    - How does it compare to other numerical solutions?
    - What are its practical uses?

Assumptions

Simplifications made in the derivation of the dynamical ECB model boil down to a few key assumptions about the thin, conductive sheet:

- *Low Magnetic Reynolds Number:* Corresponding to assumptions on the sheet thickness, a low magnetic Reynolds number means that *skin effects* of the currents induced in the sheet of thickness d are not present. This is true when the skin depth is larger than the total thickness: $\delta_s > d$. This is a fair assumption if the relative velocity between the conductive sheet and a magnetic field is not too large. $\delta_s < d$ implies that the induced currents are confined to a section of the sheet thickness, instead of being evenly distributed.
- *Uniform Conductivity:* The sheet conductivity σ is assumed constant and uniform over the entire sheet volume. In reality the electrical conductance depends on the temperature of the conductor, and kinetic energy is dissipated as heat in the moving conductor for ECB applications.

1.2 Thesis Outline

An outline of the chapters contained in this thesis:

Chapter 1 - Introduction

This chapter presents the real world implications of the topic, aiming to justify the succeeding research. The purpose, goal and structure of the thesis are clearly presented. Significant variables, parameters and conventions used in the following chapters are described.

Chapter 2 - Background

Some fundamental laws of classical electromagnetism are presented, and used to explain the source and result of the eddy current phenomenon. The special case of a thin, conductive sheet extending infinitely in the plane is introduced - which is the geometry for which the succeeding model derivation is based. Finally, a literature study of a few established analytical, approximate and experimental results that are relevant to the research conducted in the following chapters is presented.

Chapter 3 - A Dynamical Model for The Eddy Current Brake

The thin geometry described in chapter 2 is formalized, and the necessary spatial coordinate frames are introduced. The fundamental electromagnetic theory in chapter 2 is applied to the special case of a thin conductive sheet. The FET is described in broad terms, and used in conjunction with the 2D Fourier Transform, Sturm-Liouville Theory and Plancherel's Theorem to derive a dynamical model for the ECB.

Chapter 4 - Spectral Numerical Method

The spectral method for numerical approximation of differential equations is presented, along with arguments for its compatibility with our approach to modeling the ECB in chapter 3. The process and consequences of the spatial discretization needed for its implementation are discussed at length.

Chapter 5 - ECB Model Analysis and Simulation

Analysis of the analytical solution derived in chapter 3 is conducted, where possible. Next, the spectral numerical method described in chapter 4 is implemented, and its accuracy evaluated in detail. After establishing the appropriate design parameters of the method, the fully discretized dynamical model is realized and evaluated.

Chapter 6 - Engineering Applications

Two engineering applications are implemented using the numerical solution: State of the art, robust control algorithms and optimization of the ECB configuration. The merit of the method for each application is discussed.

Chapter 7 - Conclusion

The results of the preceding research are finalized in a brief conclusion. Some topics of further research are outlined.

1.3 Nomenclature

Time-, and space varying scalars and vectors:

Symbol	SI Unit	Description
$\boldsymbol{\xi}$	m	Position in space
$\mathbf{x}$	m	Position in the plane
z	m	Vertical Position
$\mathbf{k}$	m^{-1}	Spatial frequency
t	s	Time
ω	$\mathrm{rad\ s}^{-1}$	Temporal (radial) frequency
$\mathbf{X}$	m	Discrete position in the plane
$\mathbf{K}$	m^{-1}	Discrete spatial frequency
T	s	Discrete time
$\mathbf{B}$	Wb	Net magnetic field
$\mathbf{B}'$	Wb	Induced magnetic field
$\mathbf{C}$	Wb	Controlled magnetic field
$\boldsymbol{\Gamma}$	Wb	In-plane controlled magnetic field
q	$\mathrm{Wb\ or\ A\ m}^{-1}$	Controlled field strength
$\mathbf{P}$	1	Spatial distribution function
$\mathbf{J}$	$\mathrm{A\ m}^{-2}$	Current density
ψ	$\mathrm{A\ m}^{-3}$	Current stream function
$\mathbf{D}$	N	Magnetic damping force
P_{diss}	W	Electrical power dissipation
$\mathbf{r}$	m	Sheet translation
$\mathbf{v}$	$\mathrm{m\ s}^{-1}$	Sheet translation velocity
$\mathbf{v}_r$	1	Relative velocity

Table 1.1: Commonly used variables.

Physical parameters, assumed constant:

Symbol	SI Unit	Description
μ	$\mathrm{Wb(A\ m)^{-1}}$	Magnetic permeability
ϵ	$\mathrm{F\ m^{-1}}$	Permittivity
σ	$\mathrm{S\ m^{-1}}$	Electrical conductivity
ν	$\mathrm{m\ s^{-1}}$	Characteristic recession speed
d	m	Sheet thickness ($d = 2b$)
b	m	Vertical displacement of sheet surfaces ($z = \pm b$)
c	1	Compensation factor
h	m	Vertical displacement of the controlled field
r	m	Radius of pole projection area
V	$\mathrm{m^3}$	Sheet volume of integration

Table 1.2: Commonly used physical parameters.

Subscripts, superscripts and other modifiers:

Modifier	Description
$(\,\cdot\,)_{1,2,z}$	Planar and vertical vector field components
$(\,\hat{\cdot}\,)$	Spatial Fourier transform
$(\,\cdot\,)^{(\omega)}$	Temporal Fourier transform
$(\,\bar{\cdot}\,)$	Stationary value/equilibrium point
$(\,\cdot\,)^{l}$	In lab-frame coordinates
$(\,\cdot\,)^{m}$	In material-frame coordinates
$(\,\cdot\,)^{*}$	Conjugate transpose

Table 1.3: Commonly used modifiers.

Transformations, compositions and other operators:

Operator	Description
$\mathcal{F}_{\mathbf{x}}(\cdot)$	Spatial Fourier transformation
$\mathcal{F}_{t}(\cdot)$	Temporal Fourier transformation
$\lvert\,\cdot\,\rvert$	Euclidian norm ($\lVert\,\cdot\,\rVert_2$)
$\mathcal{L}(\cdot)$	Sturm-Liouville operator
$(\cdot) \circ \varphi$	Planar coordinate transformation

Table 1.4: Commonly used operators.

Chapter 2

Background

Relevant fundamental electromagnetic theory is presented and loosely applied to a simplified case of the ECB for illustration purposes. Established results in the literature on modeling of ECBs are presented as an extended introduction into the eddy current phenomenon, and for validation and/or verification of the later results.

2.1 Electro-/magnetodynamics

This section will provide a brief description of the fundamental theory of electromagnetism required to model the eddy-current braking phenomenon. The classical theory of electrodynamics provides a mathematical foundation on which our understanding of the forces acting between electrically charged particles is built. A natural starting point is *(James Clark) Maxwell's Equations of Electromagnetism*, a set of *Partial Differential Equations* (PDEs) describing the dynamics of electric and magnetic fields **E** and **B** in Euclidean three-

dimensional space. Matrix vector notation:

$$\mathbf{A}(\mathbf{x},t) = [A_x \;\; A_y \;\; A_z]^\intercal \qquad \text{(Arbitrary vector field } \mathbf{A}\text{)}$$

$$\nabla = \left[\frac{\partial}{\partial x} \;\; \frac{\partial}{\partial y} \;\; \frac{\partial}{\partial z}\right]^\intercal \qquad \text{(Gradient Operator)}$$

$$\nabla^\intercal \mathbf{A} = \frac{\partial A_x}{\partial x} + \frac{\partial A_y}{\partial y} + \frac{\partial A_z}{\partial z} \qquad \text{(Divergence of } \mathbf{A}\text{)}$$

$$\mathbf{S}(\nabla)\mathbf{A} = \left[\left(\frac{\partial A_z}{\partial y} - \frac{\partial A_y}{\partial z}\right) \;\; \left(\frac{\partial A_x}{\partial z} - \frac{\partial A_z}{\partial x}\right) \;\; \left(\frac{\partial A_y}{\partial x} - \frac{\partial A_x}{\partial y}\right)\right]^\intercal \qquad \text{(Curl of } \mathbf{A}\text{)}$$

$$\mathbf{S}(\mathbf{x}) = \begin{bmatrix} 0 & -z & y \\ z & 0 & -x \\ -y & x & 0 \end{bmatrix} \qquad \text{(Cross-product operator)}$$

The PDEs, found throughout Maxwell's publications (ex. [1]) and reduced to 4 equations via vector notation, read:

$$\nabla^\intercal \mathbf{D} = \rho \qquad \text{(Gauss' Law)} \qquad (2.1)$$

$$\nabla^\intercal \mathbf{B} = 0 \qquad \text{(Gauss' Law for Magnetism)} \qquad (2.2)$$

$$\mathbf{S}(\nabla)\mathbf{E} = -\frac{\partial \mathbf{B}}{\partial t} \qquad \text{(Faraday's Law of Induction)} \qquad (2.3)$$

$$\mathbf{S}(\nabla)\mathbf{H} = \mathbf{J} + \frac{\partial \mathbf{D}}{\partial t} \qquad \text{(Ampére's Circuital Law)} \qquad (2.4)$$

These equations can be given the following physical interpretations:

Given an arbitrary closed surface $\mathcal{S}$, *Gauss' Law* (2.1) and *Gauss' Law for Electromagnetism* (2.2) state that the divergence of (*i*) the electric field and (*ii*) the magnetic field are required to, (*i*) be proportional to the charge density ρ inside the volume bounded by $\mathcal{S}$ and (*ii*) be equal to zero. Key consequences of these laws are that (*i*) the electric field diverges from positive charge, and converges at negative charge and (ii) magnetic field lines form loops in space (Figure 2.1).

Faraday's Law (2.3) and *Ampére's Law* (2.4) describe the phenomenon of magnetic induction due to a change in either **B** or **E**. A magnetic field that changes in time will cause an opposite proportional circulation the electric field. In a conductor, this corresponds to a an induced voltage (and current). Similarly, the currents moving through a conductor or a changing electric field cause a circulation in the surrounding magnetic field. Noting the negative sign in (2.3), we can see that a current **J** induced by a change in **B** will be circulated by an induced magnetic field that opposes the change in **B**. This agrees with *Lenz's Law*, which states that the orientation of an induced current in a conductor due to a varying

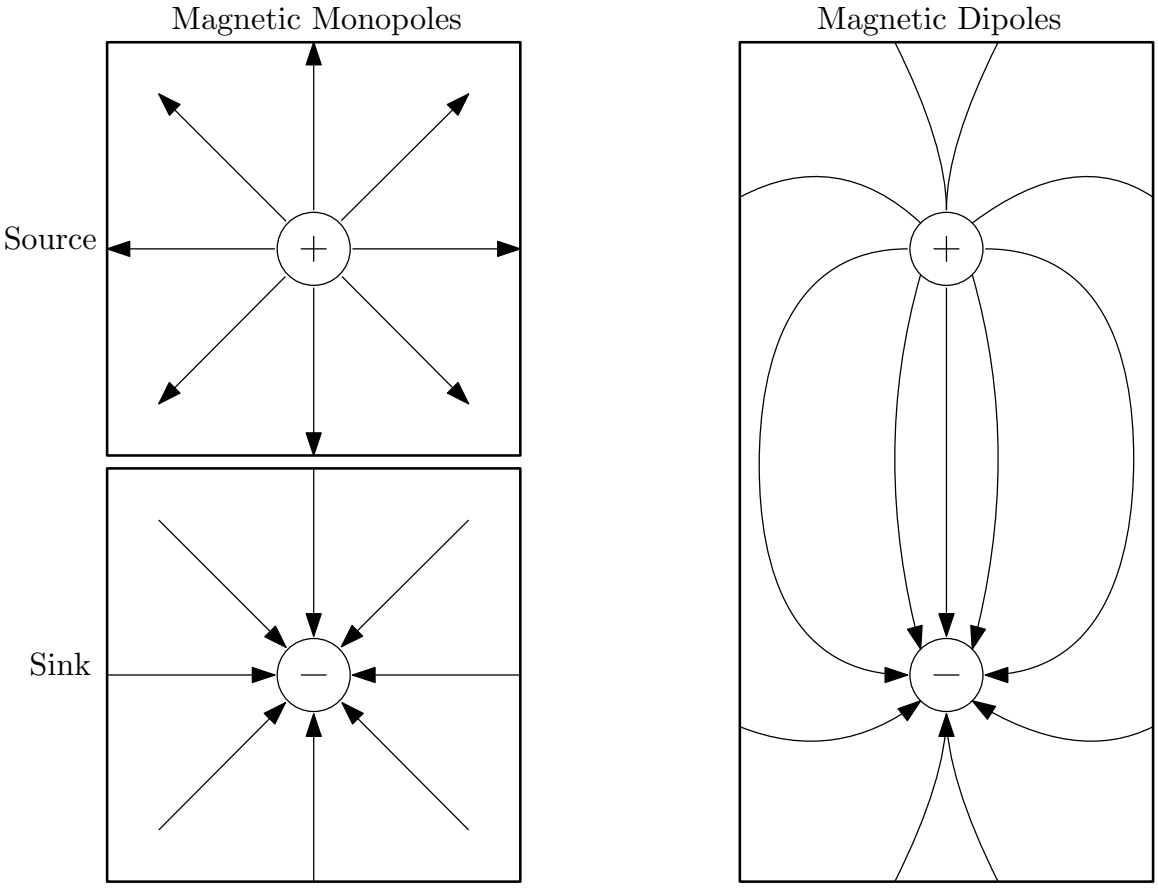

Figure 2.1: Magnetic point charges (left) acting as source/sink of the magnetic field lines always come in pairs (right) in nature.

magnetic field, will always be such that the generated magnetic field will counteract the original change.

In (2.1-2.4), note that the vector fields **E** and **B** represent the actual physical fields affecting charged particles. **E** and **B** are related to the *Electric Displacement Field* **D**, *Polarization* **P**, *Magnetic Auxillary Field* **H** and *Magnetization* **M** by:

$$\mathbf{D} = \epsilon_0 \mathbf{E} + \mathbf{P} \tag{2.5}$$

$$\mathbf{B} = \mu_0 (\mathbf{H} + \mathbf{M}) \tag{2.6}$$

Where the parameters ϵ_0 and μ_0 describe the vacuum *Permittivity* and *Permeability*, respectively. For a linear medium, i.e the pairs **E**, **P** and **H**, **M** are linearly related, (2.5-2.6)

simplify to:

$$\mathbf{D} = \epsilon\mathbf{E}$$
$$\mathbf{B} = \mu\mathbf{H}$$

Where ϵ and μ are the absolute permittivity and permeability of the given medium. The vector formulation of *Ohm's Law* relates the electric field $\mathbf{E}$ to the current density $\mathbf{J}$ in a medium of *Conductivity* σ:

$$\mathbf{J} = \sigma\mathbf{E} \tag{2.7}$$

Finally, the force acting on a volume element with charge q due to the fields $\mathbf{E}$ and $\mathbf{B}$ is called the *Lorentz Force* and is given by:

$$\mathbf{f} = q\mathbf{E} + q\mathbf{S}(\mathbf{v})\mathbf{B} = q\mathbf{E} + \mathbf{S}(\mathbf{J})\mathbf{B} \tag{2.8}$$

Where $\mathbf{v}$ is the average velocity of the volume elements relative to the magnetic field $\mathbf{B}$. The total magnetic force acting on a volume is found by integrating (2.8) over the total volume V:

$$\mathbf{F} = \int_V \mathbf{f} dV \tag{2.9}$$

2.2 Eddy Current Braking

Before proceeding to reformulating and solving Maxwell's equations for thin, conductive sheets - this section will attempt to explain the not so obvious eddy-current braking phenomenon. It is well documented that a conductor moving with a velocity $\mathbf{v}$ relative to an external magnetic field $\mathbf{B}$, will experience damping forces due to the resulting magnetic field generated by the induced currents. Furthermore, With the help of (2.1-2.4) and (2.8), we can gain an intuitive understanding of how and why this phenomenon occurs.

We will consider the case of a conductor that extends infinitely in the plane, and has a small and uniform thickness. Let a constant and uniform external magnetic field $\mathbf{B}$ exist in a finite region of the plane, and let the vertical component (perpendicular to the plane/sheet surface) of this field be nonzero. Finally, let the sheet translate in the plane with velocity $\mathbf{v}$. This corresponds to the setup of a conductive sheet moving through the air-gap of a magnetic dipole, where the area projected by the poles onto the sheet is much smaller than the full sheet size. Existing literature on eddy current braking use this configuration almost exclusively, as the results can be accurately applied to ex. the linear braking of trains on conductive rails and braking torque of sufficiently large disks.

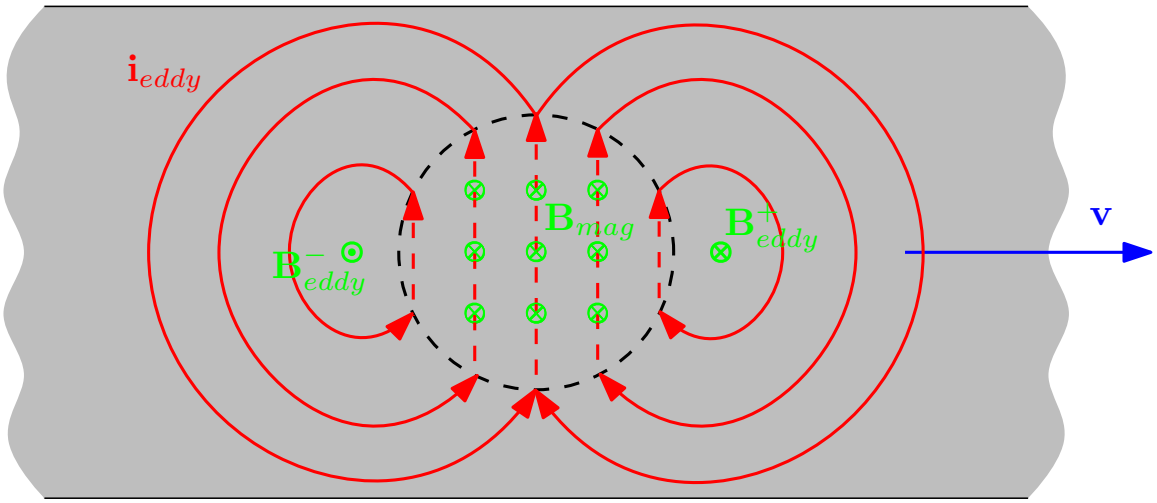

Figure 2.2: Planar cross-section of a conductive sheet moving linearly through a circular pole projection area. Blue, green and red vectors denote the sheet velocity, induced magnetic fields and eddy current return paths, respectively. Figure source: [2].

For simplicity, let us only consider a constant and uniform vertical component of **B**, and the velocity along one axis in the plane (Figure 2.2). At any given time t, volume elements (locked to the sheet material) will flow at equal rates into the magnetic field in one end (*i*), and out of the magnetic field at the other end (*ii*) of the pole projection area. The resulting rate of change $\frac{\partial}{\partial t}\mathbf{B}$ onto these volume elements will be directed: (*i*) *with* **B** and (*ii*) *opposite* to **B**. From Faraday's Law (2.3), it is clear that the changing vertical component of **B** is accompanied by rotating electric fields **E** and currents $\mathbf{J} = \sigma\mathbf{E}$ in the plane which have opposite direction for (*i*, *ii*) - these circulating currents in the plane are the *Eddy Currents*.

We know from Ampére's Law (2.4) and Lenz's Law that the induced currents **J** in turn generate magnetic fields in the conductor, and that these fields will be directed such that they oppose the original change $\frac{\partial}{\partial t}\mathbf{B}$: The generated fields will (*i*) *oppose* and (*ii*) *assist* the external field **B**. The resulting drag force opposing **v** is readily seen by the magnetic forces of attraction and repulsion of the parallel fields: The volume elements of the sheet will be (*i*) *repelled by* and (*ii*) *attracted to* the fixed external field **B**. The sum of these magnetic forces clearly opposes the relative velocity **v**.

In practice, the magnetic field in the air-gap will have non-zero in-plane components due to *fringing* of magnetic field lines in space. These planar components give rise to a vertical damping force, or *lift*, in addition to the drag generated by the vertical component. This magnetic lift force is the enabling physical process for magnetic levitation. It is readily seen that magnetic braking and magnetic levitation are essentially two sides of the coin,

and can be given the collective term *magnetic damping*. While the following research topics are focused towards magnetic braking, there is an implicit applicability of the presented theory and methods to magnetic levitation.

2.3 Previous Work

Existing literature on the analytical modelling of eddy-currents and/or the resulting damping forces in conductive sheets may serve as a source of insight as well as verification. Some key results will be presented here. Numerous publications on modelling the drag force exerted by the induced eddy-currents in a conductive material affected by a varying magnetic field already exist. The earliest of these publications [3–5] predate the widespread use of Maxwell's equations (2.1-2.4), the discovery of the electron and modern computing tools. As a consequence the methods described in these publications are somewhat obscure and unfamiliar to the modern reader, but nevertheless provide a few key interpretations of the eddy-current phenomenon that have maintained relevancy.

2.3.1 Receding Image Construction

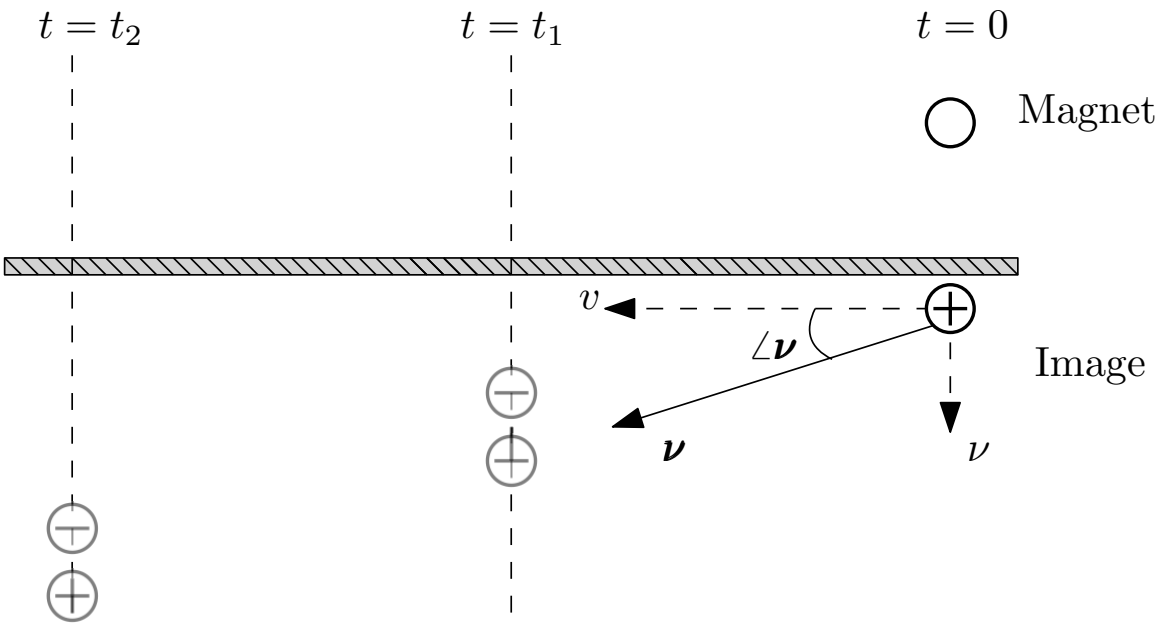

Figure 2.3: The receding image construction.

Maxwell was one of the first to investigate the induction of eddy currents in infinite, thin, conductive sheets [3]. One of his key contributions was the *Receding Image Construction* (Figure 2.3), which is an elegant and intuitive interpretation of the source and decay of induced currents and magnetic fields:
Consider a thin conductive sheet moving with velocity v in the plane relative to a magnet/-electromagnet suspended above the sheet. At time instant $t = 0$, imagine a *positive image* of the electromagnet appearing on the opposite side of the sheet. This imagined magnet represents the induced magnetic field according to Lenz' Law. At the next time-instant $t = t_1$, the positive image will translate horizontally with the sheet away from the real magnet while simultaneously translating vertically away from the sheet. Again, according to Lenz' Law, a *negative image* is formed and is of equal strength and opposite polarity of the first image. For the succeeding time-instances, the dipole formed by the pair of images continues translating away from the sheet and the magnet which induced them. Maxwell defines the vertical velocity with which the images *Recede* from the sheet as a constant velocity ν called the *Characteristic Recession Velocity*. Maxwell did not quantify this velocity in [3], but it appears explicitly in [4, 6, 7] for instance, where it is characterized by the sheet thickness d, sheet conductivity σ and vacuum permeability μ_0:

$$\nu = \frac{2}{\mu_0 \sigma d} \tag{2.10}$$

An interesting quantity to consider is the angle formed by the velocity vector of the images

$$\boldsymbol{\nu} = \begin{bmatrix} v \\ \nu \end{bmatrix}$$

with the horizontal line:

$$\tan\left(\angle \boldsymbol{\nu}\right) = \frac{\nu}{v} \tag{2.11}$$

The trail of receding images produced by the magnet describe the continuous decay of the magnetic field generated by the eddy-currents, when the step size between each time instant approaches zero.

2.3.2 Solution Methods

Some publications on eddy current braking have used Maxwell's Equations in order to uncover the induced magnetic field $\mathbf{B}'$ of the eddy-currents due to an external field $\mathbf{C}$, which can be integrated over a volume to directly yield the resulting forces. In these publications, Maxwell's Equations are typically reduced to the following first order PDEs for the vertical

component above and below the sheet surface, which is of greatest interest in braking applications:

$$\frac{\partial(B'_z + C_z)}{\partial t} = \pm\nu\frac{\partial B'_z}{\partial z} \tag{2.12}$$

(2.12) is obtained by assuming axial symmetry about both planar axes for the induced magnetic fields, in which case differentiation of the integral form of Ampére's Law yields (on the top surface):

$$\mu_0 J_x = -2B'_y, \quad \mu_0 J_y = 2B'_x \tag{2.13}$$

Combining (2.13) with Ohm's Law (2.7) and Faraday's Law (2.3), yields the first order PDEs (2.12). This first order PDE formulation is nearly ubiquitous in the literature on analytical modelling of eddy currents in braking applications (see [7–11], for instance). Publications vary greatly in their solution methods and boundary condition formulations, however. A few results considered in this paper are presented in some detail in the following subsections.

Approximate Solutions

Smythe [8] and Scheiber [9] solved (2.12) for disk shaped conductive sheets rotating with angular velocity Ω through a uniform vertical magnet air-gap, assuming that the magnitude of the induced field B'_z is small enough to were it does not interfere significantly with the total magnetic field in the air-gap. This implies that the resulting model is confined to low angular speeds, where the induced fields are negligible compared to the external field.

Smythe's drag force/torque model is a linear damper, and was found by Wouterse [12] to agree with the approximate model obtained by assuming a disk shaped PPA surrounded by an imagined ring of infinite conductivity. The PPA contains a vertical, uniform magnetic field B_0 perpendicular to the velocity of the sheet v. With this idealized configuration, the eddy current return paths are confined to the cylindrical volume

$$V = \pi r^2 d$$

of the sheet under the PPA. The dissipation due to the induced currents is given by the volume integral of the electrical power density $1/\sigma J^2$, where $J = \sigma E = -\sigma v B_0$ from Ohm's Law and Lorentz Force balance:

$$P_{\text{diss}} = \int_V \frac{1}{\sigma} J^2 dV = \pi\sigma r^2 d B_0^2 v^2 \tag{2.14}$$

Assuming that the kinetic energy dissipation due to the magnetic braking is entirely in the form of heat produced by the eddy currents, and introducing the compensation factor

$$c = \frac{1}{2}\left(1 - \frac{1}{4}\frac{1}{(1+\frac{r}{R_{\text{disk}}})^2(\frac{R_{\text{disk}}-R_{\text{arm}}}{2r})^2}\right) \tag{2.15}$$

the braking force is given by:

$$F_D = \frac{P_{\text{diss}}}{v} = \pi\sigma r^2 d B_0^2 v c \tag{2.16}$$

Where r is the radius of the PPA, R_{arm} is the distance from the disk center to the PPA center, and R_{disk} is the disk radius. Due to its simplicity, this approximate model is often is in engineering applications of ECBs, despite being inaccurate for high speeds.

Analytical Solutions

Reitz [6] used Maxwell's receding image construction to derive an analytical result for the stationary drag and lift forces experienced by a magnetic monopole translating parallel to a conductive sheet surface. Differential equations are bypassed by evaluating the torque given by the magnetic dipole moment, which for a monopole corresponds to a force:

$$F_L = qB_z' = \frac{\mu_0 q^2}{16\pi h^2}\left(1 - \frac{\nu}{\sqrt{v^2+\nu^2}}\right) \tag{2.17a}$$

$$F_D = \frac{\nu}{v}F_L = \frac{\mu_0 q^2}{16\pi h^2}\frac{\nu}{v}\left(1 - \frac{\nu}{\sqrt{v^2+\nu^2}}\right) \tag{2.17b}$$

Where the monopole has strength (magnetic moment per unit length) q, is suspended a constant height h above the sheet, and is moving with velocity v relative to the sheet. B_z' is the total vertical magnetic field generated by the trail of receding images.

2.3.3 Demagnetization

Smythe [8] noted that for higher sheet velocities, the magnitude of induced magnetic fields is great enough that they will weaken the external field that created them - resulting in a loss of braking force. In [12], theoretical results of the asymptotic behaviour of the braking force as a function of sheet speed were presented. Most notably, the vertical component of the total magnetic field in a magnet air-gap was shown to approach zero as the speed

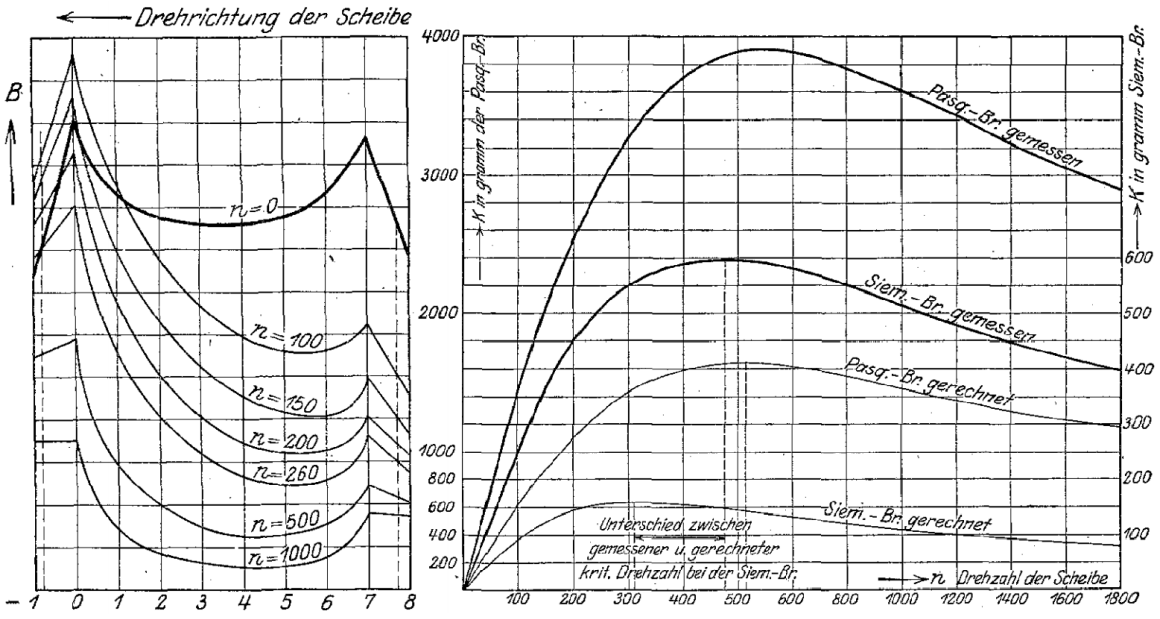

Figure 2.4: Left: The total magnetic induction in the cross section of a round PPA tangential to the disk rotation (*drehrichtung; rotational direction*) for a range of speeds n. Source: [13, pp.151]. Right: Rüdenbergs results [5] (*gerechnet; expected*) compared with experimental results (*gemessen; measured*). The plot [13, pp.144] shows braking force as a function of disk velocity.

approaches infinity. As a consequence, the magnetic braking force will decay for large v as well. The asymptotic braking force behaviour for $v \in [0, \infty)$ is characterized by

$$F_D \propto \begin{cases} v, & v < v_{cr} \\ v^{-1}, & v > v_{cr} \end{cases} \tag{2.18}$$

based on analytic results in the low speed region [8, 9], and on experimental results for the high speed region [13] (Figure 2.4). Observe Reitz' drag force model (2.17) satisfies this asymptotic behaviour [2]:

$$\lim_{v\to 0}\left[\frac{\nu}{v}\left(1-\frac{\nu}{(v^2+\nu^2)^{1/2}}\right)\right] = \lim_{v\to 0}\left(\frac{\nu(v^2+\nu^2)^{1/2}-\nu^2}{v(v^2+\nu^2)^{1/2}}\right) \sim \left[\frac{0}{0}\right]$$

$$\text{(L'Hôpital's rule)} \rightarrow = \lim_{v\to 0}\left(\frac{\nu v}{2\cdot 2v^2+2\nu^2}\right) = \lim_{v\to 0}\frac{v}{2\nu}$$

$$\lim_{v\to\infty}\left[\frac{\nu}{v}\left(1-\frac{\nu}{(v^2+\nu^2)^{1/2}}\right)\right] = \lim_{v\to\infty}\frac{\nu}{v}$$

The critical speed v_{cr} for which the braking force reaches its maximum, was predicted by Wouterse to be given by:

$$v_{cr} = \nu\sqrt{\frac{1}{\xi c}}\sqrt{\frac{l_g}{2r}} \tag{2.19}$$

Where l_g is the vertical air-gap length, and ξ is a proportionality factor, assumed equal to unity. (2.19) is supported by an experimental result in [13] noting a 'slower than proportional ascent' of the critical velocity as a function of the air-gap. of According to (2.19), a critical recession angle (2.11) can be predicted by:

$$\angle\boldsymbol{\nu}_{cr} = \frac{\nu}{v_{cr}} = \sqrt{2\frac{\xi cr}{l_g}} \tag{2.20}$$

Chapter 3

A Dynamical Model for the Eddy Current Brake

This chapter presents the geometrical and kinematic framework used to describe the thin sheet geometry. The FET, loosely described during the course of the solution strategy, is employed to yield two-dimensional fractional diffusion equations for the dynamics of the magnetic fields and currents in the sheet. These are integrated over the spectral plane by Plancherel's theorem to yield the magnetic damping force vector.

3.1 Problem Formulation

The laws of electromagnetism will be applied to the thin sheet configuration described in (Section 2.2), aiming to compute the total magnetic field density $\mathbf{B} = \mathbf{B}' + \mathbf{C}$ - the sum of the induced magnetic field $\mathbf{B}'$ and an external (controlled) magnetic field $\mathbf{C}$. First, some necessary preliminaries on the sheet and pole geometries in space as well as coordinate schemes and reference frames are presented.

3.1.1 Sheet Geometry and Coordinate Frames

Due to the thin geometry being considered, and for later transformations during the solution strategy, it will be useful to separate the space $\mathbb{R}^3$ into planar and vertical components

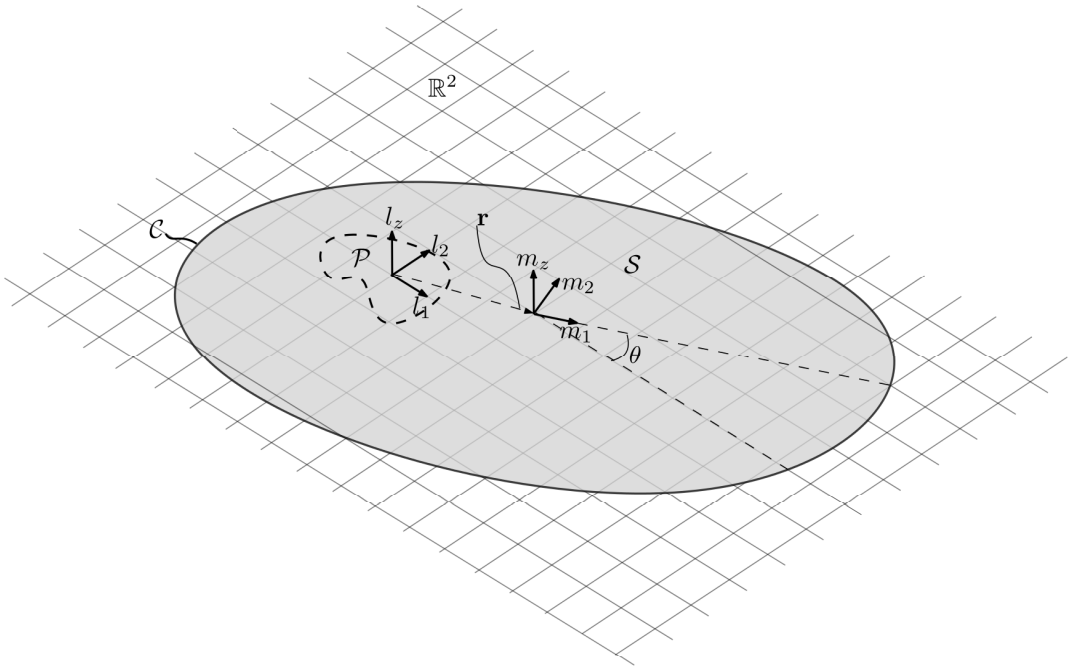

Figure 3.1: $\mathcal{S}$ and $\mathcal{P}$ centered at $z = 0$ in their respective material-/lab-frames.

$\mathbf{x} \in \mathbb{R}^2$ and $z \in \mathbb{R}$. The position vector $\boldsymbol{\xi} \in \mathbb{R}^3$ is written as:

$$\boldsymbol{\xi} = \begin{bmatrix} \mathbf{x} \\ z \end{bmatrix}, \quad \mathbf{x} = \begin{bmatrix} x_1 \\ x_2 \end{bmatrix}$$

We let the conductive sheet inhabit a volume given by the subspace $V \subset \mathbb{R}^3$:

$$V = \{\boldsymbol{\xi} : \mathbf{x} \in \mathcal{S},\ |z| \leq b\} \tag{3.1}$$

Where $\mathcal{S}$ is a planar surface that extends indefinitely in $\mathbb{R}^2$, but is bounded by some closed curve $\mathcal{C}$ (Figure 3.1). Another planar surface $\mathcal{P}$ represents the projection onto $\mathcal{S}$ of the field excited by a magnetic pole suspended some height above the sheet.

The free bodies (sheet, magnet) represented by their 2D projections $\mathcal{S}$ and $\mathcal{P}$ each have their own reference frame: The *material* frame m and the *laboratory* (lab) frame l, locked to the sheet and pole projection centroids respectively. The time-varying, planar transformation between these frames is specified by the operator:

$$\begin{aligned} &\varphi : \mathbf{x}^l \to \mathbf{x}^m \\ &\mathbf{x}^m = \mathbf{R}_{z,\theta(t)}\mathbf{x}^l + \mathbf{r}^l(t) = \varphi(\mathbf{x}^l, \theta, \mathbf{r}^l) \\ &\mathbf{x}^l = \mathbf{R}_{z,-\theta(t)}\mathbf{x}^m - \mathbf{r}^m(t) = \varphi^{-1}(\mathbf{x}^m, \theta, \mathbf{r}^m) \end{aligned} \tag{3.2}$$

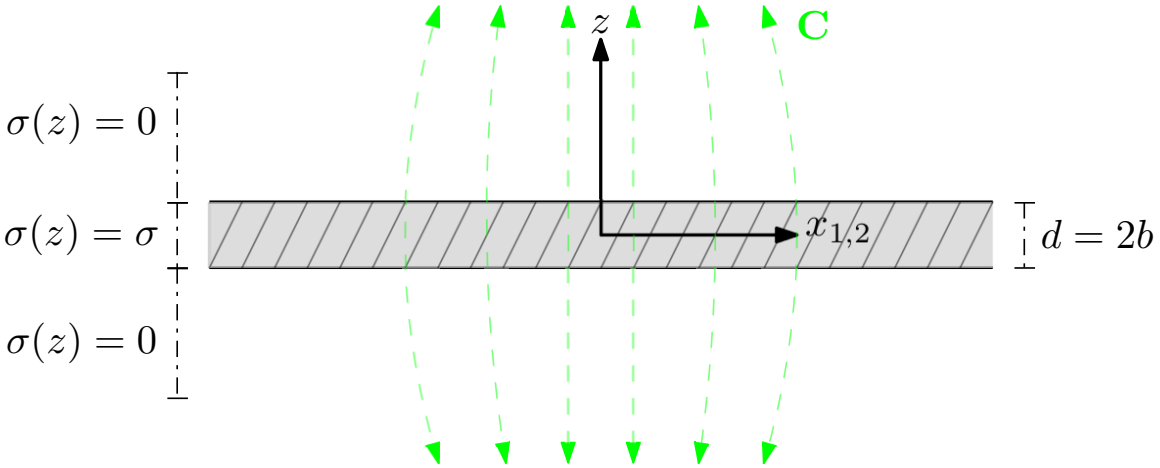

Figure 3.2: Vertical cross-section of the conductive sheet and possible distribution of the external field **C**.

Simply put, a translation $\mathbf{r} = [r_1 \;\; r_2]^\intercal$ in the plane and a counter-clockwise rotation θ about the shared vertical axis z:

$$\mathbf{R}_{z,\theta} = \begin{bmatrix} \cos\theta & -\sin\theta \\ \sin\theta & \cos\theta \end{bmatrix}$$

3.1.2 Magnetic Field PDEs

For the following derivation of PDEs for the total magnetic field **B**, we will use the shorthand $\boldsymbol{\xi} = \boldsymbol{\xi}^m$ such that all vectors are given in the material frame unless otherwise stated. Consider a sheet of thickness $2b$ and let the conductivity in space be a function of z, such that

$$\sigma(\boldsymbol{\xi}) = \sigma(z) = \begin{cases} \sigma & |z| \leq b \\ 0 & |z| > b \end{cases}$$

In other words, the conductive sheet is surrounded (above and below) by an entirely non-conductive medium such that induced currents are contained in the sheet. We also assume, for simplicity, that $\mu(\boldsymbol{\xi}) = \mu_0$ - where the constant μ_0 is the vacuum permeability. This is a good approximation as long as the sheet material is relatively non-magnetic ($\mu_s \approx \mu_0$), which is the case for many conductive metals such as aluminium - for instance. Furthermore, we assume linear electric and magnetic fields in and around the sheet. Maxwell's equations for the linear medium, assuming the electric field is in equilibrium $\left(\frac{\partial \mathbf{E}}{\partial t} = \mathbf{0}\right)$,

can be written as:

$$\nabla^\intercal \mathbf{E} = \frac{\rho}{\epsilon} \tag{3.3}$$

$$\nabla^\intercal \mathbf{B} = 0 \tag{3.4}$$

$$\mathbf{S}(\nabla)\mathbf{E} = \frac{\partial \mathbf{B}}{\partial t} \tag{3.5}$$

$$\mathbf{S}(\nabla)\mathbf{B} = \mu_0 \mathbf{J} \tag{3.6}$$

Equations (3.3-3.6) describe spatial and temporal dynamics of the magnetic field density $\mathbf{B}(\boldsymbol{\xi}, t)$ and electric field $\mathbf{E}(\boldsymbol{\xi}, t)$. We proceed by reducing these equations to a set of 3-Dimensional PDEs for $\mathbf{B}$ only. Inserting *Ohm's Law* (2.7) into the modified *Ampére's Law* (3.6) yields:

$$\begin{aligned} \mathbf{S}(\nabla)\mathbf{B} &= \mu_0 \sigma(z)\mathbf{E} \\ \Rightarrow \mathbf{E} &= \frac{1}{\mu_0 \sigma(z)} \mathbf{S}(\nabla)\mathbf{B} \end{aligned}$$

Which, inserted into *Faraday's Law* (3.5), yields:

$$\mathbf{S}(\nabla)(\mathbf{S}(\nabla)\mathbf{B}) = \mathbf{S}(\nabla)^2\mathbf{B} = \mu_0 \sigma \mathbf{S}(\nabla)\mathbf{E} = -\mu_0 \sigma \frac{\partial \mathbf{B}}{\partial t}$$

Using the vector identity,

$$\mathbf{S}(\nabla)^2 \boldsymbol{\xi} = \left(-\nabla^\intercal \nabla \mathbf{I} + \nabla \nabla^\intercal\right) \boldsymbol{\xi} = \left(-\Delta \mathbf{I} + \nabla \nabla^\intercal\right) \boldsymbol{\xi}$$

where $\Delta = \frac{\partial^2}{\partial x_1^2} + \frac{\partial^2}{\partial x_2^2} + \frac{\partial^2}{\partial z^2}$ is the operator known as the *Laplacian*, we end up with the following set of PDEs:

$$\mu_0 \sigma(z) \frac{\partial \mathbf{B}}{\partial t} = \Delta \mathbf{B} - \nabla \left(\nabla^\intercal \mathbf{B}\right) = \Delta \mathbf{B} \tag{3.7}$$

Where $\nabla^\intercal \mathbf{B} = 0$ due to *Gauss' Law for Magnetism* (3.4). Let us express the total magnetic flux density $\mathbf{B}$ as the sum of the external (controlled) magnetic field $\mathbf{C}$ and the resulting magnetic field $\mathbf{B}'$ induced by the eddy-currents in the sheet interior: $\mathbf{B} = \mathbf{B}' + \mathbf{C}$. We may separate the problem into two cases: *(i)* The sheet *interior* ($|z| \leq b$) and *(ii)* the sheet *exterior* ($|z| > b$). Using the superposition principle, we may assume that the controlled external field $\mathbf{C}$ is entirely a consequence of some external process - e.g an electromagnetic circuit. Likewise, the induced magnetic field $\mathbf{B}'$ is entirely a consequence of the current

density **J** confined to the sheet interior.

(i), $|z| \leq b$:

$$\begin{aligned}
&\nabla^\intercal \mathbf{B} = \nabla^\intercal \mathbf{B}' + \nabla^\intercal \mathbf{C} = 0 \\
&\mathbf{S}(\nabla)\mathbf{B} = \mu_0 \sigma \mathbf{E} = \mu_0 \mathbf{J} = \mathbf{S}(\nabla)\mathbf{B}' \\
&\Delta \mathbf{B} = -\mathbf{S}(\nabla)^2 \mathbf{B} = \Delta \mathbf{B}' \\
&\Delta \mathbf{C} = \mathbf{0} \\
&\Delta \mathbf{B}' = -\mu_0 \sigma \mathbf{S}(\nabla)\mathbf{E} = \mu_0 \sigma \frac{\partial \mathbf{B}}{\partial t}
\end{aligned}$$

(ii), $|z| > b$:

$$\begin{aligned}
&\nabla^\intercal \mathbf{B} = \nabla^\intercal \mathbf{B} + \nabla^\intercal \mathbf{C} = 0 \\
&\mathbf{S}(\nabla)\mathbf{B} = \mu_0 \cdot 0 \cdot \mathbf{E} = \mathbf{0} \\
&\Delta \mathbf{B} = \Delta \mathbf{B}' = \mu_0 \cdot 0 \cdot \frac{\partial \mathbf{B}}{\partial t} = \mathbf{0}
\end{aligned}$$

Thus, the set of PDEs simplify to the time-dependent and time-independent diffusion equations:

$$\mu_0 \sigma \left(\frac{\partial \mathbf{B}'}{\partial t} + \frac{\partial \mathbf{C}}{\partial t} \right) = \Delta \mathbf{B}' \qquad \textit{(i)} \tag{3.8a}$$

$$\mathbf{0} = \Delta \mathbf{B}' \qquad \textit{(ii)} \tag{3.8b}$$

In particular, the problem is equivalent to the 3-dimensional heat and Laplace equations in the sheet interior/exterior, respectively. If we consider only the z-component B_z, which is the component of **B** responsible for the drag force during horizontal movement of the sheet, we get the following second order PDEs:

$$\frac{\partial B_z'}{\partial t} + \frac{\partial C_z}{\partial t} = \frac{1}{\mu_0 \sigma} \left(\frac{\partial^2}{\partial x_1^2} + \frac{\partial^2}{\partial x_2^2} + \frac{\partial^2}{\partial z^2} \right) B_z' \qquad \textit{(i)} \tag{3.9a}$$

$$0 = \left(\frac{\partial^2}{\partial x_1^2} + \frac{\partial^2}{\partial x_2^2} + \frac{\partial^2}{\partial z^2} \right) B_z' \qquad \textit{(ii)} \tag{3.9b}$$

If we successfully solve equations (3.8), the current density **J** follows directly from (3.6). Finally, net forces **F** can be integrated from (2.8):

$$\mathbf{F} = \int_V q\mathbf{E} dV + \int_V \mathbf{S}(\mathbf{J})(\mathbf{B}' + \mathbf{C}) dV = \int_V \mathbf{S}(\mathbf{J})(\mathbf{B}' + \mathbf{C}) dV \tag{3.10}$$

Where the first integral term disappears, since the net electric field in a conductor such as our sheet is always zero.

$f(\mathbf{x})$	$\hat{f}(\mathbf{k})$	**Description**
$f(\mathbf{x}-\mathbf{x}_0)$	$e^{-i\mathbf{k}^{\mathrm{T}}\mathbf{x}_0}\hat{f}(\mathbf{k})$	Shifting Theorem
$f(\mathbf{R}_z\mathbf{x})$	$\hat{f}(\mathbf{R}_z\mathbf{k})$	Rotation Theorem
$f(\mathbf{x})*g(\mathbf{x})$	$\hat{f}(\mathbf{k})\hat{g}(\mathbf{k})$	Convolution Theorem
$f(\mathbf{x})g(\mathbf{x})$	$f(\mathbf{k})*g(\mathbf{k})$	Inverse Convolution Theorem

Table 3.1: Some relevant properties of the 2D Fourier Transform used throughout this thesis (see [15]).

3.2 Solution Strategy

The interior problem currently requires the solution of a three-dimensional, time-varying set of PDEs (3.8). This section details how, through the use of a two-dimensional *Fourier Transform* (FT) as well as an evaluation of the resulting eigenvalue problem through *Sturm-Liouville* (SL) theory, the interior problem can be regarded as a set of linear dynamic equations evaluated over the sheet spectrum without significant loss of accuracy. The 3D PDEs (3.8) are effectively reduced to a 2D problem by exploiting the harmonic behaviour of the magnetic fields in the exterior. The following description of the solution strategy is a less rigorous than, but agrees with the method presented in an upcoming publication [14].

3.2.1 2D Fourier Transform

Each component of the diffusion equations (3.8) for the magnetic field $\mathbf{B}$ can be reduced further by *Fourier Transformation* (FT) in the plane. For this purpose we define the 2-Dimensional FT of an integrable function f as the operator:

$$\mathcal{F}_x : f(\mathbf{x}) \to \hat{f}(\mathbf{k})$$
$$f \in \mathbb{R},\ \hat{f} \in \mathbb{C},\ (\mathbf{x},\mathbf{k}) \in \mathbb{R}^2$$

The forward and inverse transforms are given by:

$$\mathcal{F}_x\Big(f(\mathbf{x})\Big) = \int_{\mathbb{R}^2} f(\mathbf{x})e^{-i\mathbf{k}^{\mathrm{T}}\mathbf{x}}d\mathbf{x} = \hat{f}(\mathbf{k}) \tag{3.11a}$$

$$\mathcal{F}_x^{-1}\left(\hat{f}(\mathbf{k})\right) = \frac{1}{(2\pi)^2}\int_{\mathbb{R}^2} \hat{f}(\mathbf{k})e^{i\mathbf{k}^{\mathrm{T}}\mathbf{x}}d\mathbf{k} = f(\mathbf{x}) \tag{3.11b}$$

The variable transformation $\mathbf{x} \to \mathbf{k}$ in (3.11) corresponds to a transformation from whichever

domain x belongs to (time, space, or other) to the inverse domain (temporal frequency, spatial frequency, ...). In our case, we will refer to the transformation pair $\mathbf{x} \rightarrow \mathbf{k}$ as the *spatial* and *spectral* plane variables, respectively. The FT of $\mathbf{B}(x_1, x_2, z, t)$ for each fixed (z, t) is then given by the spectra:

$$\hat{\mathbf{B}}(k_1, k_2, z, t) = \int_{-\infty}^{\infty} \int_{-\infty}^{\infty} \mathbf{B}(x_1, x_2, z, t) e^{-i(k_1 x_1 + k_2 x_2)} dx_1 dx_2 \tag{3.12}$$

A property of the FT that is instrumental in the reduction of differential equations, is the equivalence of differentiation in the original domain and multiplication in the inverse domain:

$$\mathcal{F}_x \left(\frac{\partial}{\partial x_{1,2}} f(\mathbf{x}) \right) = \int_{\mathbb{R}^2} \frac{\partial}{\partial x_{1,2}} f(\mathbf{x}) e^{-i\mathbf{k}^{\mathrm{T}}\mathbf{x}} d\mathbf{x} = ik_{1,2} \int_{\mathbb{R}^2} f(\mathbf{x}) e^{-i\mathbf{k}^{\mathrm{T}}\mathbf{x}} d\mathbf{x} = ik_{1,2} \hat{f}(\mathbf{k})$$

Which can be shown easily by integration by parts. This allows for the transformation of the differential variables (x_1, x_2) into algebraic variables (k_1, k_2), and makes for a less complex set of equations. Thus, by applying the FT to both sides of (3.8), we get the following set of equations:

$$\frac{\partial \hat{\mathbf{B}}'}{\partial t} + \frac{\partial \hat{\mathbf{C}}}{\partial t} = \frac{1}{\mu_0 \sigma} \left(-k_1^2 - k_2^2 + \frac{\partial^2}{\partial z^2} \right) \hat{\mathbf{B}}' \qquad \textit{(i)} \tag{3.13a}$$

$$0 = \left(-k_1^2 - k_2^2 + \frac{\partial^2}{\partial z^2} \right) \hat{\mathbf{B}}' \qquad \textit{(ii)} \tag{3.13b}$$

We rewrite (3.13) by introducing the change of variables:

$$|\mathbf{k}|^2 = k_1^2 + k_2^2$$

$$\nu = \frac{2}{\mu_0 \sigma \cdot 2b} = \frac{1}{\mu_0 \sigma b}$$

$$\zeta = \frac{z}{b} \tag{3.14}$$

$$\boldsymbol{\kappa} = \mathbf{k} b \tag{3.15}$$

$$\tau = t \frac{\nu}{b} \tag{3.16}$$

Where ν is the characteristic velocity and ζ, $\boldsymbol{\kappa}$, τ are the dimensionless vertical coordinate, spectral coordinates and time, respectively. Such that:

$$\frac{\partial \hat{\mathbf{B}}'}{\partial \tau} + \frac{\partial \hat{\mathbf{C}}}{\partial \tau} = \left(-|\boldsymbol{\kappa}|^2 + \frac{\partial^2}{\partial \zeta^2} \right) \hat{\mathbf{B}}' \qquad \textit{(i)} \tag{3.17a}$$

$$0 = \left(-|\mathbf{k}|^2 + \frac{\partial^2}{\partial z^2} \right) \hat{\mathbf{B}}' \qquad \textit{(ii)} \tag{3.17b}$$

3.2.2 Boundary Conditions

As with all PDEs, the interior problem of (3.17) has an infinite number of solutions. In order to identify unique, non-trivial solutions for the magnetic field density spectra $\hat{\mathbf{B}}'$ we must identify boundary conditions for the remaining differential variable z. For instance, Dirichlet boundary conditions for the interior system are specified by $\hat{\mathbf{B}}'(\mathbf{k}, \pm b, t) = f$. The magnetic field density induced by eddy currents has no obvious direct function value at the sheet boundaries, however. The only obvious property of the variation of $\hat{\mathbf{B}}'$ along the vertical axis, is that it will decay towards zero as we move away from the sheet - since the exterior problem is a stationary diffusion equation along the z-axis for all values of (k_1, k_2):

$$\lim_{|z|\to\infty} \hat{\mathbf{B}}' = \mathbf{0}$$

From this point onward, we investigate the vertical and planar spectra $\left(\hat{B}'_z, \hat{B}'_{1,2}\right)$ separately. A *Boundary Value Problem* (BVP) will be derived for each component.

Vertical BVP

The vertical component of the spectral exterior problem (3.17) reads:

$$\frac{\partial^2}{\partial z^2}\hat{B}'_z(\mathbf{k}, z, t) = |\mathbf{k}|^2 \hat{B}'_z(\mathbf{k}, z, t), \qquad |z| > b \tag{3.18}$$

Thanks to the elimination of spatial differential variables in the plane, (3.18) has been reduced to a second order ODE for each fixed $(\mathbf{k}, t)$. If we say that the equation evaluated for $|z| > b$ has some unique, unknown initial values for each $(\mathbf{k}, t)$:

$$\hat{B}'_z(\mathbf{k}, b, t) = \hat{B}'_b$$
$$\hat{B}'_z(\mathbf{k}, -b, t) = \hat{B}'_{-b}$$

The unique solutions of (3.18) on either side of the sheet exterior are:

$$\hat{B}'_z = \begin{cases} e^{-|\mathbf{k}|(z-b)}\hat{B}'_b, & z \geq b \\ e^{|\mathbf{k}|(z+b)}\hat{B}'_{-b}, & z \leq -b \end{cases} \tag{3.19}$$

The initial values $\hat{B}'_{\pm b}$ correspond to Dirichlet boundary conditions for the sheet interior PDE evaluated for $z \in [-b, b]$, but are yet unknown. Robin-type boundary conditions can

however be determined by taking the z-derivative of (3.19):

$$\begin{aligned}
&\frac{\partial}{\partial z}\hat{B}'_z = -\text{sgn}(z)|\mathbf{k}|\hat{B}'_z \\
&\frac{\partial}{\partial z}\hat{B}'_z \pm |\mathbf{k}|\hat{B}'_z = 0, \qquad\qquad z = \pm b
\end{aligned} \tag{3.20}$$

The resulting BVP for $\hat{B}'_z$, using dimensionless variables, is given by:

$$\frac{\partial}{\partial \tau}\hat{B}'_z + |\boldsymbol{\kappa}^2|\hat{B}'_z - \frac{\partial^2}{\partial \zeta^2}\hat{B}'_z = -\frac{\partial}{\partial \tau}\hat{C}_z, \qquad |\zeta| \leq 1 \tag{3.21a}$$

$$\frac{\partial}{\partial \zeta}\hat{B}'_z \pm |\boldsymbol{\kappa}|\hat{B}'_z = 0, \qquad \zeta = \pm 1 \tag{3.21b}$$

Planar BVP

Equivalent Robin-type boundary conditions can be derived for each of the in-plane magnetic field components $\hat{B}'_{1,2}$ by repeating the process for the vertical BVP. We instead consider the exterior magnetic field a product of a *harmonic* potential $\hat{\Phi}$, meaning it solves the Laplace equation and is twice continuously differentiable:

$$\Delta\hat{\Phi} = \left(-|\mathbf{k}|^2 + \frac{\partial^2}{\partial z^2}\right)\hat{\Phi} = 0, \quad \hat{\Phi} \in C^{(2)}$$

Let such a potential decay to zero as $|z| \to \infty$, and let it satisfy:

$$\nabla\hat{\Phi} = \begin{bmatrix} \frac{\partial\hat{\Phi}}{\partial x_1} & \frac{\partial\hat{\Phi}}{\partial x_2} & \frac{\partial\hat{\Phi}}{\partial z} \end{bmatrix}^{\mathsf{T}} = \hat{\mathbf{B}}'$$

$$\frac{\partial\hat{\Phi}}{\partial z} = \hat{B}'_z, \quad ik_1\hat{\Phi} = \hat{B}'_1, \quad ik_2\hat{\Phi} = \hat{B}'_2$$

Recall from the previous section the derivative equation for solutions of the Laplace equation:

$$\begin{aligned}
\frac{\partial\hat{\Phi}}{\partial z} &= \hat{B}'_z = -\text{sgn}(z)|\mathbf{k}|\hat{\Phi} \\
ik_{1,2}&\left(\hat{B}'_z + \text{sgn}(z)|\mathbf{k}|\hat{\Phi}\right) = 0 \\
\Rightarrow ik_{1,2}&\hat{B}'_z + \text{sgn}(z)|\mathbf{k}|\hat{B}'_{1,2} = 0
\end{aligned} \tag{3.23}$$

The Dirichlet-type boundary conditions for the in-plane fields can be inferred from the vertical boundary value $\hat{B}'_z|_{z=\pm b}$:

$$ik_{1,2}\hat{B}'_z \pm |\mathbf{k}|\hat{B}'_{1,2} = 0, \qquad z = \pm b$$

BVPs for the in-plane fields with dimensionless variables inserted are thus given by:

$$\frac{\partial}{\partial\tau}\hat{B}'_{1,2} + |\boldsymbol{\kappa}|^2\hat{B}'_{1,2} - \frac{\partial^2}{\partial\zeta^2}\hat{B}'_{1,2} = -\frac{\partial}{\partial\tau}\hat{C}_{1,2}, \qquad |\zeta| < 1 \tag{3.24a}$$

$$i\kappa_{1,2}\hat{B}'_z \pm |\boldsymbol{\kappa}|\hat{B}'_{1,2} = 0, \qquad \zeta = \pm 1 \tag{3.24b}$$

3.2.3 Sturm-Liouville Theory

Solving the BVPs for the sheet interior can be viewed as an eigenvalue problem through *Sturm-Liouville* (SL) theory. SL theory (see for example [16, ch. 8]) defines the real, linear, second-order differential operator:

$$\mathcal{L}(x) = p_0(x)\frac{d^2}{dx^2} + p_1(x)\frac{d}{dx} + p_2(x) \tag{3.25}$$

Where the parameters satisfy $p_i \in C^{(1)}$ for a free variable x. The SL eigenvalue problem is an alternative formulation of ODEs, and takes the form:

$$\mathcal{L}\phi(x) = \lambda\phi(x) \tag{3.26}$$

If $\mathcal{L}$ is *Self-adjoint* and the functions ϕ on which it operates satisfy some boundary conditions, it is a *Hermitian* operator. Hermitian operators have some key properties motivating the eigenvalue problem formulation, such as:

1. $\mathcal{L}$ has only real valued eigenvalues $\lambda_0 < \lambda_1 < ... < \lambda_n < ... \to \infty$.
2. Corresponding eigenfunctions ϕ_i are all unique solutions of the ODE.
3. Unique eigenfunctions are all orthogonal and normalized: $\langle \phi_i, \phi_j \rangle = 0, \quad \forall i \neq j$ and $\langle \phi_i, \phi_i \rangle = 1$.

The unweighted complex inner product for continuous functions bounded by the sheet is defined as:

$$\langle f, g \rangle = \int_{-1}^{1} f^*(\zeta)g(\zeta)d\zeta \tag{3.27}$$

For (3.27), a self-adjoint operator $\mathcal{L}$ must satisfy:

$$\langle f, \mathcal{L}g \rangle = \langle \mathcal{L}^* f, g \rangle = \langle \mathcal{L}f, g \rangle$$

It can be shown that (3.25) is self-adjoint if $\frac{d}{dx}p_0(x) = p_1(x)$.

In both our BVPs (3.21, 3.24), we recognize the operator

$$\mathcal{L}(\zeta) = |\boldsymbol{\kappa}|^2 - \frac{\partial^2}{\partial \zeta^2} \tag{3.28}$$

with $p_0 = |\boldsymbol{\kappa}|^2$, $p_1 = 0$, $p_2 = 1$. Clearly, $\frac{\partial}{\partial \zeta}p_0 = p_1 = 0$, hence (3.28) is self-adjoint. The vertical BVP can be written as:

$$\frac{\partial}{\partial \tau}\hat{B}'_z + \mathcal{L}\hat{B}'_z = -\frac{\partial}{\partial \tau}\hat{C}_z, \qquad |\zeta| \leq 1 \tag{3.29a}$$

$$\frac{\partial}{\partial \zeta}\hat{B}'_z \pm |\boldsymbol{\kappa}|\hat{B}'_z = 0, \qquad \zeta = \pm 1 \tag{3.29b}$$

If we let ϕ_n denote the nth solution of (3.29), the PDE reduces to the first order dynamic equation with boundary conditions:

$$\frac{\partial}{\partial \tau}\phi_n + \lambda_n \phi_n = -\frac{\partial}{\partial \tau}\hat{C}_z, \qquad |\zeta| \leq 1 \tag{3.30a}$$

$$\frac{\partial}{\partial \zeta}\phi_n \pm |\boldsymbol{\kappa}|\phi_n = 0, \qquad \zeta = \pm 1 \tag{3.30b}$$

The eigenvalue problem of identifying the eigen-value/-function pairs is then given by:

$$\left(|\boldsymbol{\kappa}|^2 - \frac{\partial^2}{\partial \zeta^2}\right)\phi = \lambda \phi, \qquad |\zeta| \leq 1 \tag{3.31a}$$

$$\frac{\partial}{\partial \zeta}\phi \pm |\boldsymbol{\kappa}|\phi = 0, \qquad \zeta = \pm 1 \tag{3.31b}$$

Since $\lambda \in \mathbb{R}$, we can separate (3.31) into three cases:

1. $\lambda < |\boldsymbol{\kappa}|^2$
2. $\lambda = |\boldsymbol{\kappa}|^2$
3. $\lambda > |\boldsymbol{\kappa}|^2$

Solving (3.31) for ϕ yields only the trivial solution $\phi = 0$ for the first two cases, while the third case yields:

$$\phi = A\cos\left(\zeta\sqrt{\lambda - |\boldsymbol{\kappa}|^2}\right) + B\sin\left(\zeta\sqrt{\lambda - |\boldsymbol{\kappa}|^2}\right) \tag{3.32}$$

Inserting (3.32) into the boundary condition equation, yields:

$$-\left(\frac{A|\boldsymbol{\kappa}|+B\sqrt{\lambda-|\boldsymbol{\kappa}|^2}}{B|\boldsymbol{\kappa}|-A\sqrt{\lambda-|\boldsymbol{\kappa}|^2}}\right)=\tan\left(\sqrt{\lambda-|\boldsymbol{\kappa}|^2}\right), \qquad \zeta=1$$

$$-\left(\frac{-A|\boldsymbol{\kappa}|+B\sqrt{\lambda-|\boldsymbol{\kappa}|^2}}{B|\boldsymbol{\kappa}|+A\sqrt{\lambda-|\boldsymbol{\kappa}|^2}}\right)=\tan\left(\sqrt{\lambda-|\boldsymbol{\kappa}|^2}\right), \qquad \zeta=-1$$

And the equality

$$\frac{A|\boldsymbol{\kappa}|+B\sqrt{\lambda-|\boldsymbol{\kappa}|^2}}{-B|\boldsymbol{\kappa}|+A\sqrt{\lambda-|\boldsymbol{\kappa}|^2}}=\frac{A|\boldsymbol{\kappa}|-B\sqrt{\lambda-|\boldsymbol{\kappa}|^2}}{B|\boldsymbol{\kappa}|+A\sqrt{\lambda-|\boldsymbol{\kappa}|^2}}, \qquad |\zeta|=1$$

has non-trivial solutions only for $(A=0,\ B\neq 0)\ ||\ (A\neq 0,\ B=0)$ as the roots of:

$$\sqrt{\lambda-|\boldsymbol{\kappa}|^2}\sin\left(\sqrt{\lambda-|\boldsymbol{\kappa}|^2}\right)-|\boldsymbol{\kappa}|\cos\left(\sqrt{\lambda-|\boldsymbol{\kappa}|^2}\right)=0, \qquad b=0 \tag{3.33a}$$

$$\sqrt{\lambda-|\boldsymbol{\kappa}|^2}\cos\left(\sqrt{\lambda-|\boldsymbol{\kappa}|^2}\right)+|\boldsymbol{\kappa}|\sin\left(\sqrt{\lambda-|\boldsymbol{\kappa}|^2}\right)=0, \qquad a=0 \tag{3.33b}$$

Solving (3.33) for λ leads to periodically spaced eigenvalues
$|\boldsymbol{\kappa}|^2<\lambda_0(|\boldsymbol{\kappa}|)<\lambda_1(|\boldsymbol{\kappa}|)<...<\lambda_n(|\boldsymbol{\kappa}|)<...\to\infty$.

The thin geometry in question allows us to treat the norm of the dimensionless spectral variable as small

$$|\boldsymbol{\kappa}|<<1$$

such that the periodic eigenvalues can be approximated by

$$\lambda_n\approx\frac{\pi n}{2},\ \ n>0$$
$$\lambda_0\simeq|\boldsymbol{\kappa}|+|\boldsymbol{\kappa}|^2\approx|\boldsymbol{\kappa}|$$

It follows that the zero'th order eigenfunction can be approximated by the first order Taylor expansion

$$\phi_0=\cos\left(\zeta\sqrt{|\boldsymbol{\kappa}|}\right)\simeq 1-\frac{\zeta^2}{2!}|\boldsymbol{\kappa}|$$

Eigenfunction Expansion

Eigenfunction expansion of the vertical magnetic field spectra

$$\hat{B}_z'=\phi_n\langle\phi_n,\hat{B}_z'\rangle$$
$$\hat{C}_z=\phi_n\langle\phi_n,\hat{C}_z\rangle$$

inserted into (3.29), yields the model:

$$\begin{aligned}&\frac{\partial}{\partial\tau}\phi_n\langle\phi_n,\hat{B}'_z\rangle+\mathcal{L}\phi_n\langle\phi_n,\hat{B}'_z\rangle=-\frac{\partial}{\partial\tau}\phi_n\langle\phi_n,\hat{C}_z\rangle\\ \Rightarrow&\frac{\partial}{\partial\tau}\langle\phi_n,\hat{B}'_z\rangle+\lambda_n\langle\phi_n,\hat{B}'_z\rangle=-\frac{\partial}{\partial\tau}\langle\phi_n,\hat{C}_z\rangle\end{aligned}$$

Again, for a thin sheet it is reasonable to assume that the controlled field **C** does not vary much over the vertical axis. We may only consider the perturbations in the system caused by the zero'th order eigenfunction to closely approximate the system behaviour. We let $\lambda_0 \approx |\boldsymbol{\kappa}|$:

$$\frac{\partial}{\partial\tau}\langle\phi_0,\hat{B}'_z\rangle+|\boldsymbol{\kappa}|\langle\phi_0,\hat{B}'_z\rangle=-\frac{\partial}{\partial\tau}\langle\phi_0,\hat{C}_z\rangle$$

Which can be averaged over the sheet thickness $\zeta \in [-1,1]$ with little loss of accuracy, to yield the set of decoupled equations for the dynamical model:

$$\frac{\partial}{\partial\tau}\hat{B}'_{z_{av}}+|\boldsymbol{\kappa}|\hat{B}'_{z_{av}}=-\frac{\partial}{\partial\tau}\hat{C}_z \tag{3.34}$$

Replacing the dimensionless variables (3.14-3.16), (3.35) becomes:

$$\begin{aligned}&\frac{b}{\nu}\frac{\partial}{\partial t}\hat{B}'_{z_{av}}+b|\mathbf{k}|\hat{B}'_{z_{av}}=-\frac{b}{\nu}\frac{\partial}{\partial t}\hat{C}'_z\\ \Rightarrow&\frac{\partial}{\partial t}\hat{B}'_{z_{av}}+\nu|\mathbf{k}|\hat{B}'_{z_{av}}=-\frac{\partial}{\partial t}\hat{C}_z\end{aligned} \tag{3.35}$$

3.2.4 In-Plane Fields and Currents

We are less concerned with modeling the in-plane fields, as they do not contribute significantly to the magnetic braking forces. We let the in-plane fields in the interior be given by the continuous extension of the boundary values (3.23) to the sheet interior:

$$\hat{B}'_{1,2}=-\text{sat}\left(\frac{z}{b}\right)\frac{ik_{1,2}}{|\mathbf{k}|}\hat{B}'_z=-\frac{ik_{1,2}}{|\mathbf{k}|}\hat{B}'_z\times\begin{cases}\text{sgn}(z), & |z|>b\\ \frac{z}{b}, & |z|\leq b\end{cases} \tag{3.36}$$

The harmonic differentiation equation of $\hat{B}'_z$ at the boundaries (3.20) also has the continuous extension:

$$\frac{\partial}{\partial z}\hat{B}'_z=-\frac{z}{b}\hat{B}'_z, \qquad |z|\leq b$$

As previously stated, the thin geometry permits the statement

$$\begin{aligned} &\hat{B}'_z(\mathbf{k}, z) \simeq \hat{B}'_{z_{av}}(\mathbf{k}), && |z| \leq b \\ \Rightarrow &\frac{\partial}{\partial z}\hat{B}'_z \simeq 0, && |z| \leq b \end{aligned}$$

Which yields the following, for Gauss' law for magnetism (2.2) in the interior:

$$\nabla^{\intercal}\hat{\mathbf{B}}' = ik_1\hat{B}'_1 + ik_2\hat{B}'_2 + \frac{\partial}{\partial z}\hat{B}'_z = ik_1\hat{B}'_1 + ik_2\hat{B}'_2 = 0$$

Eddy Currents

The eddy current spectra may now be expressed in terms of $\hat{B}'_z$ by Ampere's Law (3.6):

$$\begin{aligned} \mu_0\mathbf{J} &= \mathbf{S}(\nabla)\mathbf{B}' \\ \mu_0 J_1 &= \frac{\partial}{\partial x_2}B'_z - \frac{\partial}{\partial z}B'_2 \\ \mu_0 J_2 &= \frac{\partial}{\partial z}B'_1 - \frac{\partial}{\partial x_1}B'_z \\ \mu_0 J_z &= \frac{\partial}{\partial x_1}B'_2 - \frac{\partial}{\partial x_2}B'_1 \end{aligned}$$

We get:

$$\begin{aligned} \mu_0\hat{J}_1 &= -ik_2\frac{\partial}{\partial z}\left(-\frac{z}{b}\frac{1}{|\mathbf{k}|}\hat{B}'_z\right) + ik_2\hat{B}'_z \\ &= -ik_2\left(\frac{z}{b}\frac{1}{|\mathbf{k}|}\frac{z}{b}|\mathbf{k}|\hat{B}'_z - \frac{1}{b}\frac{1}{|\mathbf{k}|}\hat{B}'_z - \hat{B}'_z\right) = -ik_2\left(\frac{z^2}{b^2} - \frac{1}{b|\mathbf{k}|} - 1\right)\hat{B}'_z \qquad (3.37a) \\ \mu_0\hat{J}_2 &= ik_1\frac{\partial}{\partial z}\left(-\frac{z}{b}\frac{1}{|\mathbf{k}|}\hat{B}'_z\right) - ik_1\hat{B}'_z = ik_1\left(\frac{z^2}{b^2} - \frac{1}{b|\mathbf{k}|} - 1\right)\hat{B}'_z \qquad (3.37b) \\ \mu_0\hat{J}_z &= ik_1\hat{B}'_2 - ik_2\hat{B}_1 = \left(\frac{z}{b}\frac{k_1k_2}{|\mathbf{k}|} - \frac{z}{b}\frac{k_1k_2}{|\mathbf{k}|}\right)\hat{B}'_z = 0 \qquad (3.37c) \end{aligned}$$

3.2.5 Vertical Line Averaging

Following the line of thought that the vertical field spectra are close to uniform much the vertical axis, we will "flatten" the sheet such that the fields and currents evaluated at $z = 0$

are interpreted as their average values for the upper and lower boundaries $z = \pm b$. We get that:

$$\mu_0 \hat{J}_{1_{av}} = -ik_2 \left(\frac{b^2}{b^2} - \frac{1}{b|\mathbf{k}|} - 1 \right) \hat{B}'_z = ik_2 \frac{1}{b|\mathbf{k}|} \hat{B}'_z$$
$$\mu_0 \hat{J}_{2_{av}} = -ik_1 \frac{1}{b|\mathbf{k}|} \hat{B}'_z$$
$$\mu_0 \hat{J}_{z_{av}} = 0$$

We define:

$$\hat{\psi} = \frac{1}{b\mu_0 |\mathbf{k}|} \hat{B}'_z \tag{3.38}$$

Which clearly describes a stream-function for the in-plane eddy current averages:

$$\hat{J}_{1_{av}} = ik_2 \hat{\psi}, \qquad J_{1_{av}} = \frac{\partial}{\partial x_2} \psi$$
$$\hat{J}_{2_{av}} = -ik_1 \hat{\psi}, \qquad J_{2_{av}} = -\frac{\partial}{\partial x_1} \psi$$

For the magnetic field density spectrum, the in-plane components disappear due to their asymmetric boundary conditions about $z = 0$. (3.23):

$$\hat{B}'_{1_{av}} = \left(-\frac{b}{2b} \frac{ik_1}{|\mathbf{k}|} + \frac{b}{2b} \frac{ik_1}{|\mathbf{k}|} \right) \hat{B}'_z = 0$$
$$\hat{B}'_{2_{av}} = \left(-\frac{b}{2b} \frac{ik_2}{|\mathbf{k}|} + \frac{b}{2b} \frac{ik_2}{|\mathbf{k}|} \right) \hat{B}'_z = 0$$
$$\hat{B}'_{z_{av}} \simeq \hat{B}'_z$$

For the controlled field, we define the vector:

$$\hat{\mathbf{C}}_{av} = \begin{bmatrix} \hat{C}_{1_{av}} \\ \hat{C}_{2_{av}} \\ \hat{C}_z \end{bmatrix} = \begin{bmatrix} \hat{\mathbf{\Gamma}} \\ \hat{C}_z \end{bmatrix} \tag{3.39}$$

3.2.6 Fractional Laplacian

The sheet flattening described in (Section 3.2.5) results in fields evaluated on the plane $z = 0$. Let $g(\boldsymbol{\xi})$ denote a 3D, harmonic field in the sheet interior:

$$\Delta g(\boldsymbol{\xi}) = 0, \quad \boldsymbol{\xi} \in V$$
$$\lim_{|\boldsymbol{\xi}| \to \infty} g(\boldsymbol{\xi}) = 0$$

It follows that g is also harmonic evaluated at any fixed plane $z_0 \in [-b, b]$, or in our case: $g(\mathbf{x}, z_0 = 0)$ is harmonic. It is shown in [17] that the normal derivative of such a field g is given by the principal value integral

$$\frac{\partial}{\partial z} g(\boldsymbol{\xi}) = \text{P.V} \int_{\mathbb{R}^2} \frac{g(\mathbf{x}, z_0) - g(\mathbf{x}', z_0)}{2\pi |\mathbf{x} - \mathbf{x}'|^3} d\mathbf{x}' \tag{3.40}$$

which corresponds to the *Fractional Laplacian* operator of order $2s = 1$, as identified by Bucur and Valdinoci [18]:

$$(-\Delta_{\mathbf{x}})^s = (-\Delta_{\mathbf{x}})^{1/2} \tag{3.41}$$

Where $\Delta_{\mathbf{x}}$ is the planar Laplacian operator:

$$\Delta_{\mathbf{x}} = \frac{\partial^2}{\partial x_1^2} + \frac{\partial^2}{\partial x_2^2}$$

This shows that the normal derivative of a function g, harmonic on any fixed plane $z = z_0$, is given by:

$$\frac{\partial}{\partial z} g(\boldsymbol{\xi}) = (-\Delta_{\mathbf{x}})^{1/2} g(\mathbf{x}, z_0) \tag{3.42}$$

The fractional Laplacian (3.41) can be expressed neatly in the spatial fourier domain by:

$$\mathcal{F}_{\mathbf{x}}\Big((-\Delta_{\mathbf{x}})^{1/2} g(\mathbf{x}, z_0) \Big) = |\mathbf{k}| \hat{g}(\mathbf{k}, z_0) \tag{3.43}$$

The spectral fractional Laplacian operator $|\mathbf{k}|$ appears in many places during the preceding solution strategy.

Since all magnetic 3D field components of $\mathbf{B}$, $\mathbf{B}'$ and $\mathbf{C}$ are harmonic functions in the sheet interior, the derived dynamical equation (3.35) can be classified as a fractional diffusion equation [18]. Inverse Fourier transformation of the fractional dynamics yields:

$$\begin{gathered} \frac{\partial}{\partial t} \hat{B}'_z + \nu |\mathbf{k}| \hat{B}'_z = -\frac{\partial}{\partial t} \hat{C}_z \\ \mathcal{F}_{\mathbf{x}}^{-1}(\cdot) \Downarrow \\ \frac{\partial}{\partial t}(B'_z + C_z) = \pm \nu \frac{\partial}{\partial z} B'_z, \quad z = \pm 0 \end{gathered} \tag{3.44}$$

Observe that the spatial form of the dynamical equation agrees with the common PDE (2.12) in ECB literature evaluated at fixed planes. Finally, the gradient for harmonic functions evaluated in thin geometries is given by

$$\nabla = \begin{bmatrix} \nabla_{\mathbf{x}} \\ (-\Delta_{\mathbf{x}})^{1/2} \end{bmatrix} \Rightarrow \begin{bmatrix} i\mathbf{k} \\ |\mathbf{k}| \end{bmatrix} \tag{3.45}$$
$$\mathcal{F}_{\mathbf{x}}(\cdot)$$

3.3 The Dynamical ECB Model

The finalized dynamical system describing the ECB will be presented in this section, and transformed to a suitable coordinate frame to consider the relative movement of the sheet and

3.3.1 Force Integration

We are now ready to express the force generated by the ECB. Using the vertical averages found in (Section 3.2.5), the Lorentz force (2.8) in space can be expressed as:

$$\begin{aligned}\mathbf{f} = \mathbf{S}(\mathbf{J}_{av})(\mathbf{B}'_{av} + \mathbf{C}_{av}) &= \begin{bmatrix} -\frac{\partial}{\partial x_1}\psi(B'_z + C_z) \\ -\frac{\partial}{\partial x_2}\psi(B'_z + C_z) \\ \frac{\partial}{\partial x_2}\psi C_{2_{av}} + \frac{\partial}{\partial x_1}\psi C_{1_{av}} \end{bmatrix} \\ &= \begin{bmatrix} -(B'_z + C_z)\nabla_x \\ \mathbf{\Gamma}^\intercal \nabla_x \end{bmatrix} \psi \end{aligned} \tag{3.46}$$

Where ∇_x denotes the planar gradient:

$$\nabla_x = \begin{bmatrix} \frac{\partial}{\partial x_1} \\ \frac{\partial}{\partial x_2} \end{bmatrix}$$

Integrating over the sheet volume V (3.1) and reversing the sign yields the damping forces $\mathbf{D}(t) = [D_1(t) \;\; D_2(t) \;\; D_z(t)]^{\mathrm{T}}$:

$$\begin{aligned}\mathbf{D}(t) = -\int_V \mathbf{f} dV &= \int_V \begin{bmatrix} (B'_z + C_z)\nabla_x \\ -\mathbf{\Gamma}^\intercal \nabla_x \end{bmatrix} \psi = 2b \int_{\mathcal{S}} \begin{bmatrix} (B'_z + C_z)\nabla_x \\ -\mathbf{\Gamma}^\intercal \nabla_x \end{bmatrix} \psi d\mathbf{x} \\ &= 2b \int_{\mathbb{R}^2} \psi \begin{bmatrix} -\nabla_x (B'_z + C_z) \\ \nabla_x^\intercal \mathbf{\Gamma} \end{bmatrix} d\mathbf{x} \end{aligned} \tag{3.47}$$

The last equality can be shown by integration by parts. We may compute (3.47) from the spectral fields and stream-functions integrated over the spectral plane by Plancherel's theorem, for the 2D FT (3.11):

$$\int_{\mathbb{R}^2} f(\mathbf{x}) g^*(\mathbf{x}) d\mathbf{x} = \frac{1}{(2\pi)^2} \int_{\mathbb{R}^2} \hat{f}(\mathbf{k}) \hat{g}^*(\mathbf{k}) d\mathbf{k} \tag{3.48}$$

Letting $g = \psi$ and noting that the stream-function is real valued in space $\psi^* = \psi$, the damping forces are ultimately given by the integral:

$$\mathbf{D}(t) = \frac{2b}{(2\pi)^2} \int_{\mathbb{R}^2} \hat{\psi}^* \begin{bmatrix} -i\mathbf{k}(\hat{B}'_z + \hat{C}_z) \\ i\mathbf{k}^\intercal \hat{\mathbf{\Gamma}} \end{bmatrix} d\mathbf{k} \tag{3.49}$$

3.3.2 Dynamical Model and Kinematics

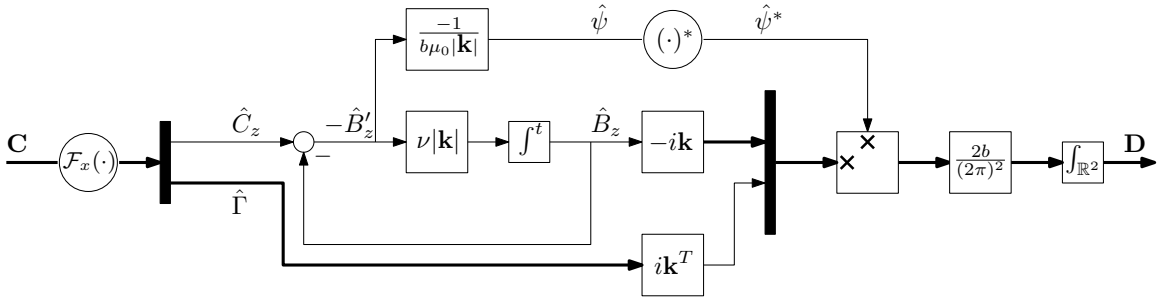

Figure 3.3: Block diagram for the dynamical ECB model.

In the preceding sections we have derived a dynamical model for the force output of an ECB (Figure 3.3). The force dynamics are governed by the dynamical model for the magnetic field (3.35), uniquely defined for each point in the spectral plane, $\mathbf{k} \in \mathbb{R}^2$. The underlying magnetic dynamics are given by:

$$\frac{\partial}{\partial t}\hat{B}'_z + \nu|\mathbf{k}|\hat{B}'_z = -\frac{\partial}{\partial t}\hat{C}_z \tag{3.50}$$

If we instead consider the dynamics of the net magnetic field spectrum $\hat{B}_z = \hat{B}'_z + \hat{C}_z$, a linear state space structure is acquired:

$$\frac{\partial}{\partial t}\hat{B}_z = -\nu|\mathbf{k}|\hat{B}_z + \nu|\mathbf{k}|\hat{C}_z \tag{3.51}$$

Recall that the fields in (3.50) are given in the material-frame, locked to the sheet. It is often times desirable to express the dynamics viewed from the lab-frame. Consider the compositions with the frame transformation φ (3.2):

$$B_z^m = B_z^l \circ \varphi^{-1}$$
$$C_z^m = C_z^l \circ \varphi^{-1}$$

In our case, the coordinate transformation φ is well defined for the Fourier transform due to the shifting and 2D rotation theorems (Table 3.1). This permits the composition of φ with the spectral fields in (3.52). We let φ describe only a translation $\mathbf{r}$ between the two frames:

$$\varphi(\mathbf{x}^l, \mathbf{r}) = \mathbf{x}^l + \mathbf{r}$$
$$\varphi(\mathbf{x}^m, \mathbf{r}) = \mathbf{x}^m - \mathbf{r}$$

Inserting into (3.51), we get:

$$\frac{\partial}{\partial t}(\hat{B}_z^l \circ \varphi^{-1}) + \nu|\mathbf{k}|\hat{B}_z^l \circ \varphi^{-1} - \nu|\mathbf{k}|\hat{C}_z^l \circ \varphi^{-1} = 0$$
$$\left(\frac{\partial}{\partial t}\hat{B}_z^l \circ \varphi^{-1} + \frac{\partial}{\partial \mathbf{x}^l}\hat{B}_z^l \circ \varphi^{-1}\frac{\partial \varphi^{-1}}{\partial t}\right) + \nu|\mathbf{k}|(\hat{B}_z^l - \hat{C}_z^l) \circ \varphi^{-1} = 0$$
$$\left(\frac{\partial}{\partial t}\hat{B}_z^l + \frac{\partial}{\partial \mathbf{x}^l}\hat{B}_z^l\frac{\partial \varphi^{-1}}{\partial t} \circ \varphi + \nu|\mathbf{k}|(\hat{B}_z^l - \hat{C}_z^l)\right) \circ \varphi^{-1} = 0$$

Taking the composition $\circ\, \varphi$ with both sides of the equation, and using

$$\frac{\partial}{\partial \mathbf{x}^l}\hat{B}_z^l = \nabla_x^{\mathrm{T}}\hat{B}_z^l = i\mathbf{k}^{\mathrm{T}}\hat{B}_z^l$$
$$\frac{\partial \varphi^{-1}}{\partial t} \circ \varphi = \big(-\dot{\mathbf{r}}(t)\big) \circ \varphi = -\dot{\mathbf{r}}(t)$$

yields the linear dynamic equation for the net magnetic field in the lab-frame:

$$\frac{\partial}{\partial t}\hat{B}_z^l = \left(i\mathbf{k}^{\mathrm{T}}\dot{\mathbf{r}} - \nu|\mathbf{k}|\right)\hat{B}_z^l + \nu|\mathbf{k}|\hat{C}_z \tag{3.52}$$

The stationary response of (3.52) will be used to verify the model with existing stationary models, and is clearly given by:

$$\bar{\hat{B}}_z^l = \frac{-\nu|\mathbf{k}|}{i|\mathbf{k}|^{\mathrm{T}}\dot{\mathbf{r}} - \nu|\mathbf{k}|}\hat{C}_z^l \tag{3.53}$$

3.3.3 A Stationary Example

We will now consider the case of a magnetic monopole standing still at fixed height h above the conductive sheet at $z = 0$, which is moving at a constant translational velocity

$$\mathbf{v} = \begin{bmatrix} v_1 \\ 0 \end{bmatrix} \tag{3.54}$$

along the x_1-axis. This is equivalent to the framework used in [6] for the analytical, stationary nonlinear damping force model (2.17). First, we express the controlled field as a monopole. The analytical expression of a monopole magnetic field distribution is given by the limit of infinitely long and thin solenoids [6], which corresponds to the potential:

$$\mathbf{C}(\boldsymbol{\xi}) = \nabla\left(\frac{-q_m}{|\boldsymbol{\xi} - \boldsymbol{\xi}_m|}\right) \tag{3.55}$$

Where $\boldsymbol{\xi}$ and $\boldsymbol{\xi}_m$ are the positions of the sheet centroid and monopole, respectively:

$$\boldsymbol{\xi} = \begin{bmatrix} x_1 \\ x_2 \\ 0 \end{bmatrix}, \quad \boldsymbol{\xi}_m = \begin{bmatrix} 0 \\ 0 \\ h \end{bmatrix}$$

Hence, (3.55) becomes.

$$\mathbf{C}(\mathbf{x}) = -q_m \nabla \left(\frac{1}{4\pi\sqrt{x_1^2 + x_2^2 + h^2}} \right)$$

Letting ∇ denote the fractional gradient operator (3.45) for the harmonic field evaluated at $z = 0$, the 2D FT is given by:

$$\begin{aligned} \hat{\mathbf{C}}(\mathbf{k}) &= -q_m \begin{bmatrix} i\mathbf{k} \\ \text{sgn}(h)|\mathbf{k}| \end{bmatrix} \mathcal{F}_x \left(\frac{1}{4\pi\sqrt{x_1^2 + x_2^2 + h^2}} \right) \\ \begin{bmatrix} \hat{\mathbf{\Gamma}}(\mathbf{k}) \\ \hat{C}_z(\mathbf{k}) \end{bmatrix} &= -q_m \begin{bmatrix} i\mathbf{k} \\ \text{sgn}(h)|\mathbf{k}| \end{bmatrix} \frac{e^{-|\mathbf{k}||h|}}{2|\mathbf{k}|} \end{aligned} \tag{3.56}$$

The stationary responses, seen from the magnet (3.53), is given by letting $\dot{\mathbf{r}} = [-v_1 \;\; 0]^{\mathrm{T}}$:

$$\begin{aligned} \bar{\hat{B}}_z &= \frac{\nu|\mathbf{k}|}{ik_1 v_1 + \nu|\mathbf{k}|} \hat{C}_z \\ \bar{\hat{B}}'_z &= \hat{B}_z - \hat{C}_z = \frac{ik_1 v_1}{ik_1 v_1 + \nu|\mathbf{k}|} \left(q_m \text{sgn}(h) \frac{e^{-|\mathbf{k}||h|}}{2} \right) \\ \bar{\hat{\psi}} &= \frac{1}{b\mu_0|\mathbf{k}|} \hat{B}'_z = \frac{\text{sgn}(h) q_m}{2b\mu_0} \frac{ik_1 v_1 e^{-|\mathbf{k}||h|}}{|\mathbf{k}|(ik_1 v_1 + \nu|\mathbf{k}|)} \end{aligned}$$

Where we have used the shorthand $\hat{(\cdot)}^{l} = \hat{(\cdot)}$. Inserting the stationary spectral field and stream-function into (3.49), yields the stationary force vector:

$$\begin{aligned} \bar{\mathbf{D}} &= \frac{1}{(2\pi)^2} \int_{\mathbb{R}^2} \frac{v_r k_1 e^{-2|\mathbf{k}||h|} q_m^2}{2\mu_0(|\mathbf{k}|^2 + v_r^2 k_1^2)} \begin{bmatrix} \mathbf{k} \\ \text{sgn}(h)(v_r k_1 - i|\mathbf{k}|) \end{bmatrix} d\mathbf{k} \\ \begin{bmatrix} \bar{D}_1 \\ \bar{D}_2 \\ \bar{D}_z \end{bmatrix} &= \frac{q_m^2}{16\pi h^2 \mu_0} \begin{bmatrix} \frac{v_r}{1+v_r^2+\sqrt{1+v_r^2}} \\ 0 \\ \left(1 - \frac{1}{\sqrt{1+v_r^2}} \text{sgn}(h) \right) \end{bmatrix} \end{aligned} \tag{3.57}$$

Where we have introduced the relative velocity

$$v_r = \frac{v_1}{\nu}$$

This result agrees agrees with Reitz' drag and lift force model (REF EQ) for a monopole strength given in $[\mathrm{Tm}^2]$:

$$q_m = \mu_0 \cdot q_{\text{Reitz}}$$

Chapter 4

Spectral Numerical Method

This chapter contains presentation and discussion of the design and analysis of the numerical method used to implement an accurate digital simulation of the derived ECB model. Some important considerations of the consequences of its use are also discussed, regarding the effects of spatial discretization and periodic boundary conditions.

4.1 Spectral Method

In this section we define the 2D spectral numerical method in accordance with [17], where it was used for an analogous thin geometry wind flow application. The spectral method refers to the process of expressing a set of differential equations in terms of their Fourier transforms, and exploiting the excellent convergence properties of the *Fast Fourier Transform* (FFT) to solve them numerically. The 2D spectral method described in this section is posed as an alternate numerical method to the time consuming 2D *Finite Element Method* (FEM), commonly used in existing publications on numerical solution of thin geometry ECB models [19–21]. The method is primarily enabled by the *Discrete Fourier Transform* (DFT) and the FFT algorithm which efficiently and accurately approximates the bounded DFT. The general, unbounded (or, semi-discrete) 2D DFT has the definition [22, ch. 2]:

$$\hat{f}(\mathbf{k}) = h_1 h_2 \sum_{n=-\infty}^{\infty} \sum_{m=-\infty}^{\infty} f[x_{1_n}, x_{2_m}] e^{-i(k_1 x_{1_n} + k_2 x_{2_m})}, \quad k_{1,2} \in \left[-\frac{\pi}{h_{1,2}}, \frac{\pi}{h_{1,2}} \right] \tag{4.1}$$

Where $f(\mathbf{x})$ is sampled with finite step-sizes $h_{1,2} > 0$ along each axis, over the entire plane $\mathbb{R}^2$, resulting in a bounded but continuous spectrum $\hat{f}(\mathbf{k})$. Its inverse is given by:

$$f[x_{1_n}, x_{2_m}] = \frac{1}{(2\pi)^2} \int_{-\pi/h}^{\pi/h} \int_{-\pi/h}^{\pi/h} \hat{f}(\mathbf{k}) e^{i(k_1 x_{1_n} + k_2 x_{2_m})} dk_1 dk_2 \tag{4.2}$$

4.1.1 Motivation

As it stands, simulation of the dynamical ECB model (Figure 3.3) requires us to evaluate the underlying dynamics (3.52) for each $\mathbf{k} \in \mathbb{R}^2$. Likewise, the forces (3.49) are integrated over the infinite plane. A discrete representation of the sheet plane and its spectrum in $N \in \mathbb{N}$ finite points is required to make this computable. Considering the diagonalized structure of the set of spectral dynamical models in the material frame (3.50),

$$\frac{\partial}{\partial t} \begin{bmatrix} \hat{B}_z(\mathbf{k}_1, t) \\ \hat{B}_z(\mathbf{k}_2, t) \\ \vdots \end{bmatrix} = \begin{bmatrix} -\nu|\mathbf{k}_1| & 0 & \dots \\ 0 & -\nu|\mathbf{k}_2| & \\ \vdots & & \ddots \end{bmatrix} \begin{bmatrix} (\hat{B}_z - \hat{C}_z)(\mathbf{k}_1, t) \\ (\hat{B}_z - \hat{C}_z)(\mathbf{k}_2, t) \\ \vdots \end{bmatrix}, \quad \mathbf{k}_n = \begin{bmatrix} k_1 \\ k_2 \end{bmatrix}_n \tag{4.3}$$

and that the drag forces can be integrated directly from the states of this spectral system by employing Plancherel's theorem (3.48), there's an incentive to isolate numerical operations to the spectral domain. It is clear that we may time-step the system (4.3) without needing to perform the numerically expensive forward and inverse Fourier transformations mid simulation. Additionally, the convolution theorem (Table 3.1) states that each multiplication $f(\mathbf{k})g(\mathbf{k})$ in the spectral system (4.3) corresponds to a convolution in space, which is another expensive operation

$$f(\mathbf{x}) * g(\mathbf{x}) = \int_{\mathbb{R}^2} f(\mathbf{x}')g(\mathbf{x} - \mathbf{x}')d\mathbf{x}'$$

that we bypass when using the spectral method.

4.1.2 Spatial and Spectral Discretization

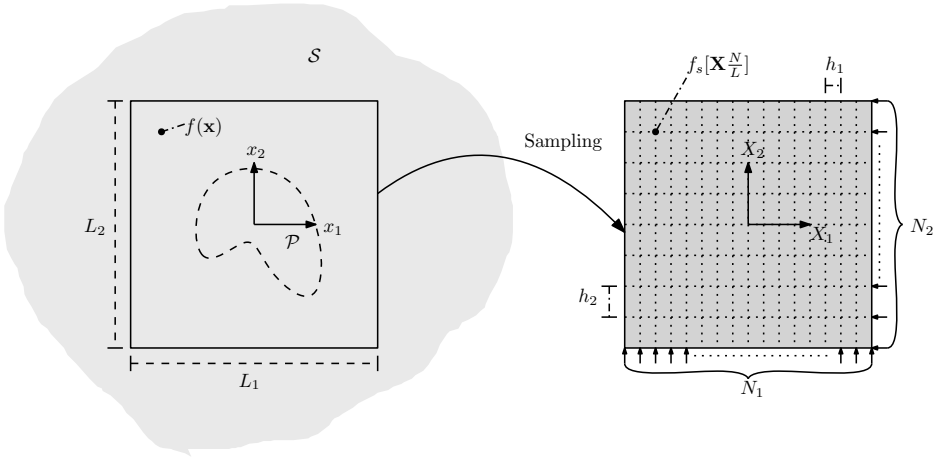

Figure 4.1: The continuous sheet surface sampled through a rectangular grid of finite dimension and resolution.

The semi-discrete DFT (4.1) is bounded by sampling the surface within a finite region in $\mathbb{R}^2$. We call this the *Sampling Grid*. An arbitrary continuous field given by the function $f(\mathbf{x})$ sampled through a rectangular grid with side lengths $L_1,\ L_2$ and resolution of $N_1 \times N_2$ evenly spaced points, where we assume $N_i = 2^{n_i}$ and $n_i \in \mathbb{N}$, is given by:

$$f_s[m_1, m_2] = f\left(\frac{L_1}{N_1}m_1, \frac{L_2}{N_2}m_2\right), \quad m_i = \{-\frac{N_i}{2}, \ \dots, 0, \ \dots, \frac{N_i}{2} - 1\} \tag{4.4}$$

Taking the DFT of (4.4) yields the spectrum of a function that is assumed to be periodic on its boundaries [22, ch. 3] (Figure 4.2). Also, a periodic sampling grid of bounded dimensions and resolution corresponds to a bounded and discrete spectral plane. Noting that the sampling step-size is given by

$$h_{1,2} = \frac{L_{1,2}}{N_{1,2}}$$

we get the following forward and inverse transform pair for the bounded DFT:

$$\hat{f}_s[l_1, l_2] = \frac{L_1 L_2}{N_1 N_2} \sum_{m_1=-\frac{N_1}{2}}^{\frac{N_1}{2}-1} \sum_{m_2=-\frac{N_2}{2}}^{\frac{N_2}{2}-1} f_s[m_1, m_2] e^{-i(\frac{m_1}{N_1}l_1 + \frac{m_2}{N_2}l_2)} \tag{4.5a}$$

$$f_s[m_1, m_2] = \frac{N_1 N_2}{L_1 L_2} \sum_{l_1=-\frac{N_1}{2}}^{\frac{N_1}{2}-1} \sum_{l_2=-\frac{N_2}{2}}^{\frac{N_2}{2}-1} \hat{f}[l_1, l_2] e^{i(\frac{m_1}{N_1}l_1 + \frac{m_2}{N_2}l_2)} \tag{4.5b}$$

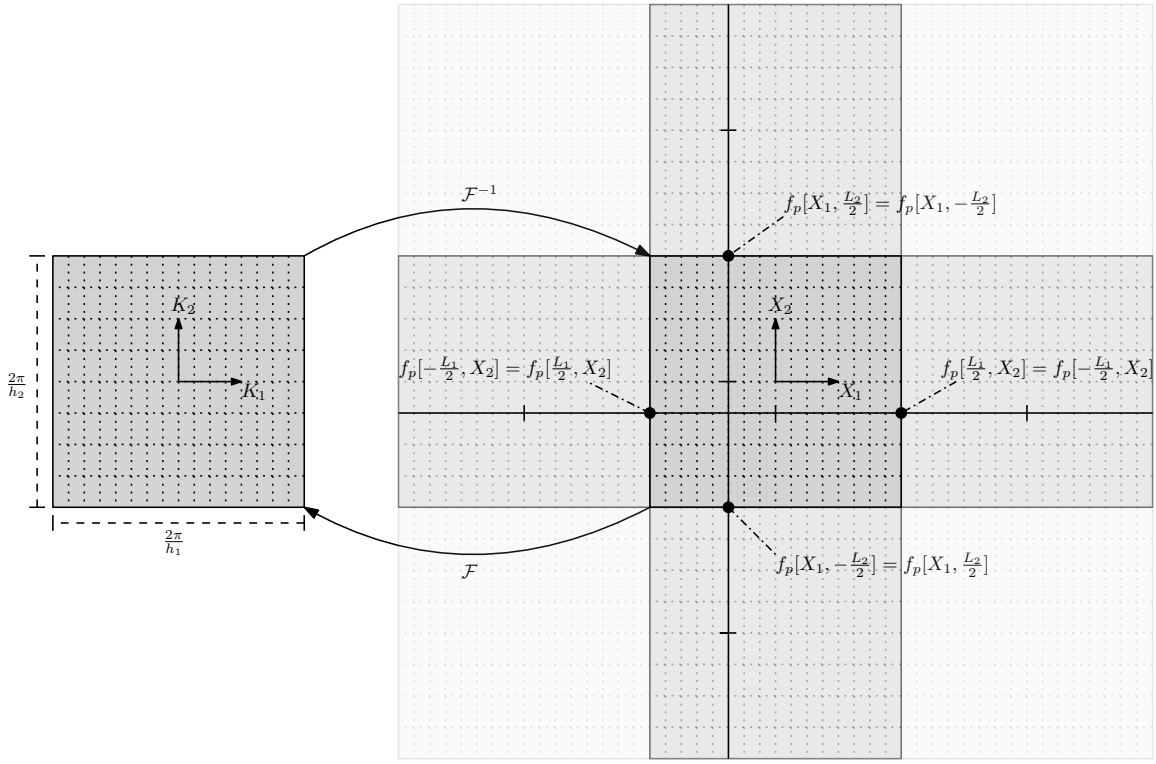

Figure 4.2: $L_{1,2}$-periodicity of the spatial grid forced by the bounded, discrete spectral grid.

The spatial and spectral variables $\mathbf{X} = [X_1 \;\; X_2]^\intercal$ and $\mathbf{K} = [K_1 \;\; K_2]^\intercal$ are given by:

$$X_{1,2}[m_{1,2}] = L_{1,2}\frac{m_{1,2}}{N_{1,2}}$$
$$K_{1,2}[l_{1,2}] = 2\pi\frac{l_{1,2}}{L_{1,2}}$$

Hence, we may express the interpolated fields by:

$$f_p[X_1, X_2] = f_s\left[X_1\frac{N_1}{L_1}, X_2\frac{N_2}{L_2}\right] \tag{4.6a}$$
$$\hat{f}_p[K_1, K_2] = \hat{f}_s\left[K_1\frac{L_1}{2\pi}, K_2\frac{L_2}{2\pi}\right] \tag{4.6b}$$

Implementation

The discretized lab-frame dynamical model (3.52), using the shorthand $\hat{(\cdot)}_z^{\,l} = \hat{(\cdot)}_z$, can then be written as:

$$\frac{\partial}{\partial t}\hat{B}_z[\mathbf{K},t] = \left(i\mathbf{K}^\intercal\dot{\mathbf{r}} - \nu|\mathbf{K}|\right)\hat{B}_z[\mathbf{K},t] + \nu|\mathbf{K}|\hat{C}_z[\mathbf{K},t] \tag{4.7}$$

The damping forces (3.49) are given by the double sum:

$$\mathbf{D}(t) = \frac{2b}{L_1L_2}\sum_{K_1}\sum_{K_2}\hat{\psi}^*[\mathbf{K}]\begin{bmatrix} -i\mathbf{K}\left(\hat{B}'_z[\mathbf{K}] + \hat{C}_z[\mathbf{K}]\right) \\ i\mathbf{K}^\intercal\hat{\mathbf{\Gamma}}[\mathbf{K}] \end{bmatrix} \tag{4.8}$$

4.2 Pole Projection Area

A key criteria for designing the sampling grid for the discretized problem, is the area on the sheet surface affected by the controlled field $\mathbf{C}$ - the *Pole Projection Area* (PPA). The intensity of the field exerted, and more importantly the spatial distribution of the field produced by the magnet, govern the spatial area and frequency of significance of the induced fields. We proceed by investigating analytical field distributions according to the magnetic poles used in the existing literature, and the accuracy of their implementation using the DFT.

4.2.1 Analytic Surface Distributions

Recall the surface $\mathcal{P}$ (Figure 3.1) representing a finite surface area of projection from the source of the controlled magnetic field $\mathbf{C}$. The following expression will define the controlled field:

$$\mathbf{C}(\mathbf{x},t) = q(t)\mathbf{P}(\mathbf{x}) \tag{4.9}$$

The controlled variable $q(t)$ scales the strength of the field with spatial distribution

$$\mathbf{P}(\mathbf{x}) = \begin{bmatrix} P_1(\mathbf{x}) \\ P_2(\mathbf{x}) \\ P_z(\mathbf{x}) \end{bmatrix} \tag{4.10}$$

representing the pole projection area $\mathcal{P}$ In (Table 4.1), we use the definitions

$$\Theta(y) = \begin{cases} 0, & y < 0 \\ 1, & y \geq 0 \end{cases} \tag{4.11}$$

$P_{1,2,z}(\mathbf{x})$	$\hat{P}_{1,2,z}(\mathbf{k})$	**Notes**
Disk: $\Theta\big(r - \|\text{diag}\{a,b\}(\mathbf{x}-\mathbf{x}_0)\|_2\big)$	$2\pi e^{-i\mathbf{k}^{\mathrm{T}}\mathbf{x}_0}\frac{rJ_1(r\chi)}{\chi}$	$J_1(\cdot)$ is the 1. order Bessel function, and $\chi = \|\text{diag}\left\{\frac{1}{a},\frac{1}{b}\right\}\mathbf{k}\|_2$.
Rectangle: $\Theta\big(r - \|\cdot\|_\infty\big)$	$\frac{1}{ab}e^{-i\mathbf{k}^{\mathrm{T}}\mathbf{x}_0}\text{sinc}\big(\text{diag}\left\{\frac{1}{2\pi a},\frac{1}{2\pi a}\right\}\mathbf{k}\big)$	sinc$(\cdot)$ is the 2D sine cardinal function.
Gaussian: $\exp\big(-\pi\|\cdot\|_2\big)$	$\frac{1}{ab}e^{-i\mathbf{k}^{\mathrm{T}}\mathbf{x}_0}\exp\big(\frac{-\chi^2}{4\pi}\big)$	2D Gaussian spectrum is also a Gaussian.

Table 4.1: Analytical 2D surfaces in the spatial plane and their spectra. The surfaces are centered at $\mathbf{x}_0$, their size is given by the scalar $r > 0$, and they are scaled by $a > 0$ and $b > 0$ along each axis (see [15].)

for the Heaviside step-function, and

$$\|\mathbf{x}\|_p = \left(\sum_i |x_i|^p\right)^{\frac{1}{p}}$$

for the p-norm - where the infinity-norm is given by the max-norm:

$$\|\mathbf{x}\|_\infty = \max_i |x_i|$$

A monopole distribution will be needed to reproduce the results of Davis and Reitz [6, 7, 10] numerically. Recall from (Section 3.3.3) that a monopole suspended a height h above $z = 0$ and centered at $\mathbf{x}_0$ can be expressed analytically as:

$$\mathbf{P}^{mono}(\mathbf{x}) = \frac{1}{4\pi\big(||\mathbf{x}-\mathbf{x}_0||_2^2 + h^2\big)^{3/2}}\begin{bmatrix}\mathbf{x}\\ -h\end{bmatrix} \tag{4.12}$$

2D FT of (4.12) yields:

$$\hat{\mathbf{P}}^{mono}(\mathbf{k}) = -e^{-i\mathbf{k}^T\mathbf{x}_0}\begin{bmatrix}\frac{i\mathbf{k}}{|\mathbf{k}|}\\ \text{sgn}(h)\end{bmatrix}\frac{e^{-|\mathbf{k}||h|}}{2} \tag{4.13}$$

Note that the right-hand exponential function in (4.13) corresponds to a vertical shift by h, and can be applied to any of the presented spectral surfaces (Table 4.1). For instance, a disk at height h above $z = 0$ is given in the 2D Fourier domain as:

$$\hat{P}^{disk}_{1,2,z}(\mathbf{k}) = 2\pi e^{-i\mathbf{k}^{\mathrm{T}}\mathbf{x}_0}\frac{RJ_1(R\chi)}{\chi}e^{-|\mathbf{k}||h|}$$

4.2.2 FFT Implementation

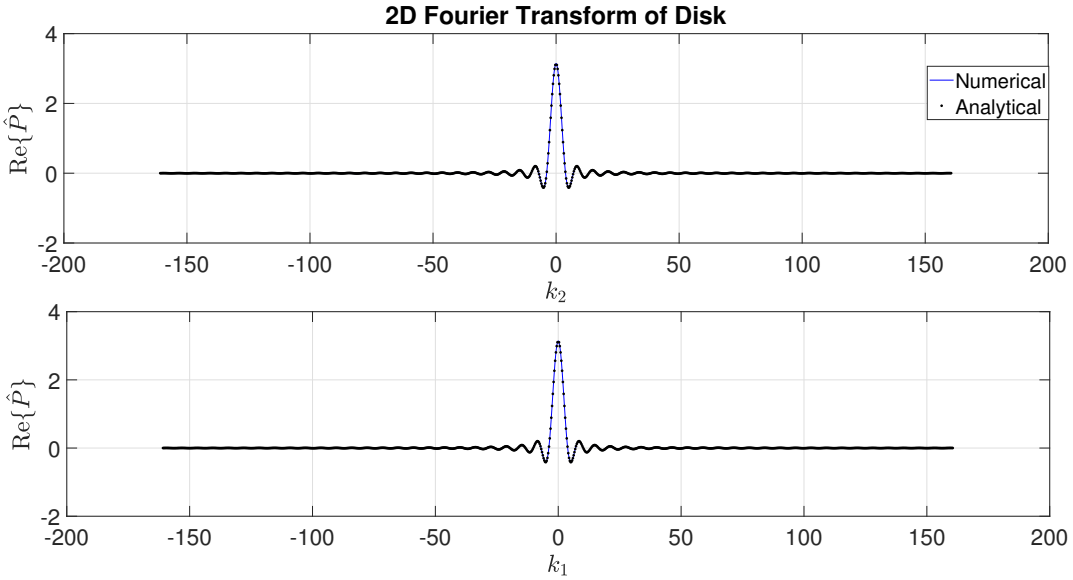

Figure 4.3: Verification of the numerical disk spectrum given by the 2D DFT.

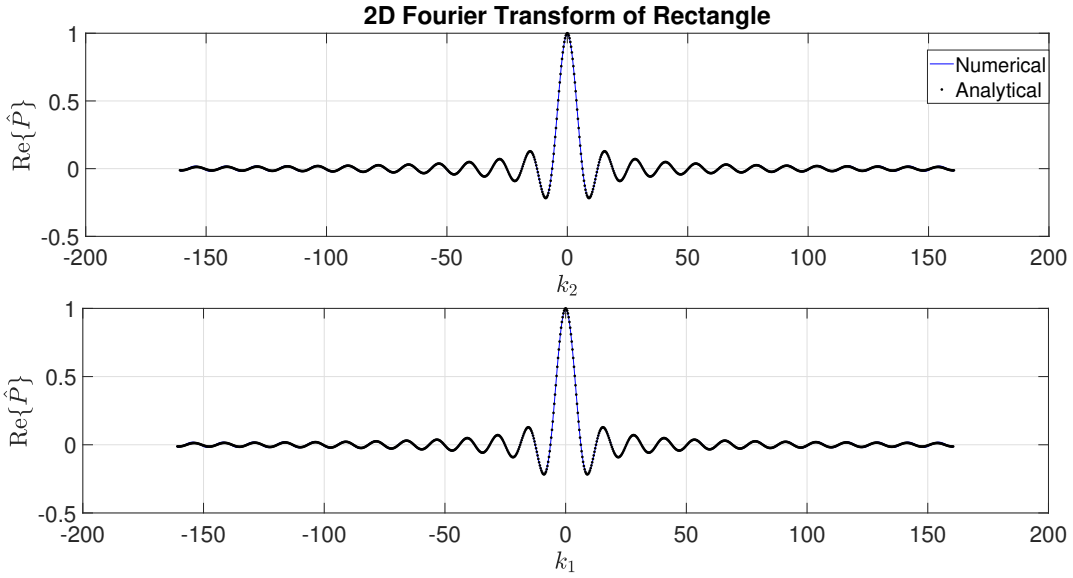

Figure 4.4: Verification of the numerical rectangle spectrum given by the 2D DFT.

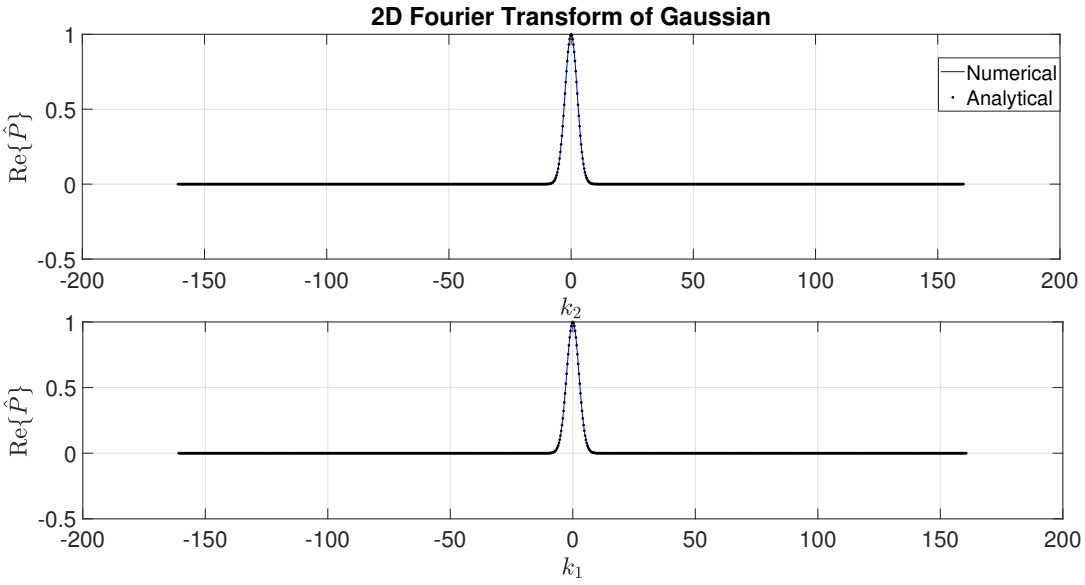

Figure 4.5: Verification of the numerical Gaussian spectrum given by the 2D DFT.

For a sampling grid defined by,

$$(L_1, L_2) = (20, 20)$$
$$(N_1, N_2) = (2^{10}, 2^{10})$$

we find that the error of the numerical solution using FFT is negligible along each spectral axis (Figure 4.3-4.5) for each of the PPA shapes presented in (Table 4.1) of unit radius. It was observed that smaller grid resolutions were sufficient for the FFT of the Gaussian distribution, while the unit rectangle and disk shapes were more computationally demanding.

Discontinuous vs. Continuous Pole Shapes

From the spatial and spectral plane pairs (Figure 4.6-4.8), it is clear that the increased resolution requirements on the sampling grid for the disk and rectangle shapes is partly due to aliasing. Since these PPAs are defined by the discontinuous Heaviside step-function (4.11), whereas the Gaussian is a continuous distribution in space, their frequency distribution extends further into the spectral plane. The step-function is known to have a Fourier transform which magnitude has asymptotic decay rate $(k_{1,2})^{-1}$, much slower than the exponential decay rate for the Gaussian. Neither distribution is band-limited in the Fourier domain, hence the Nyquist frequency is infinite and some degree of aliasing is unavoidable - but negligible

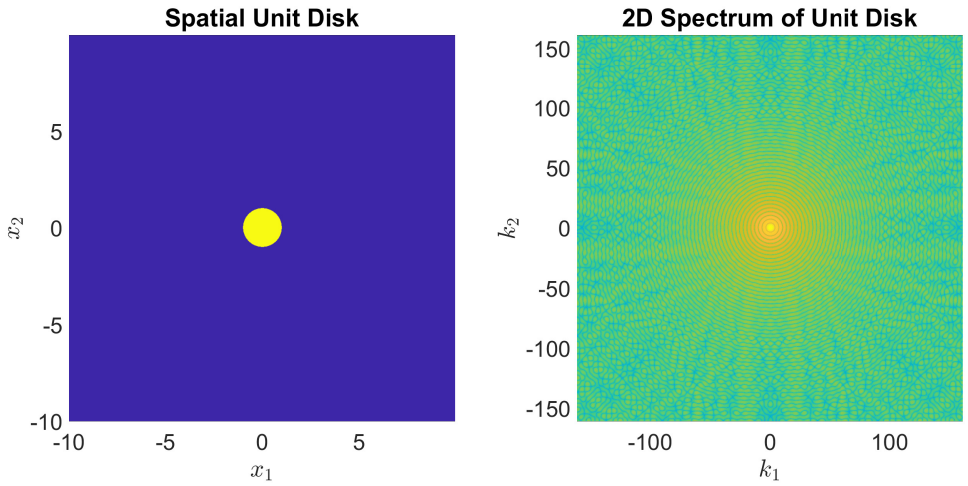

Figure 4.6: Spatial and spectral discretizations of a disk-shaped projection with $r = 1$.

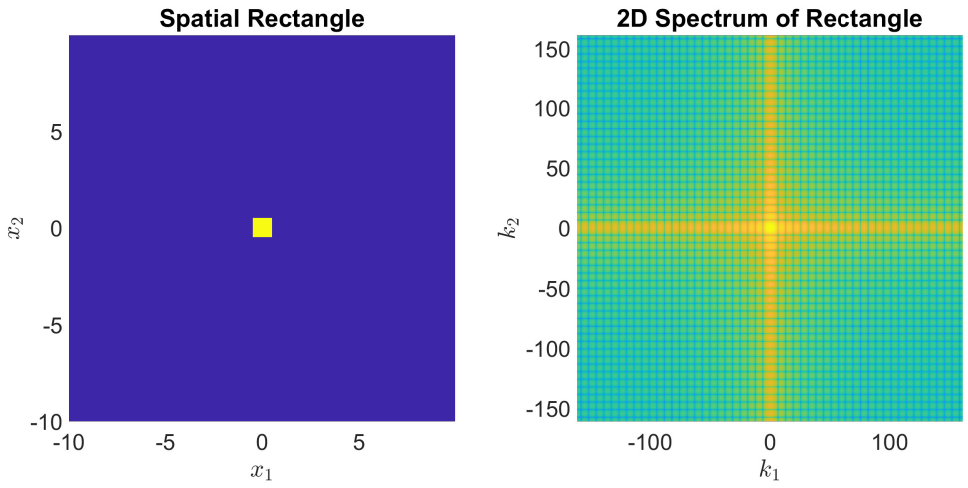

Figure 4.7: Spatial and spectral discretizations of a rectangular projection with $r = 1$.

for high resolution grids. Our inability to capture every frequency component of the PPAs manifests itself as pixellation of the shapes in space, and is the most noticeable in the disk shape.

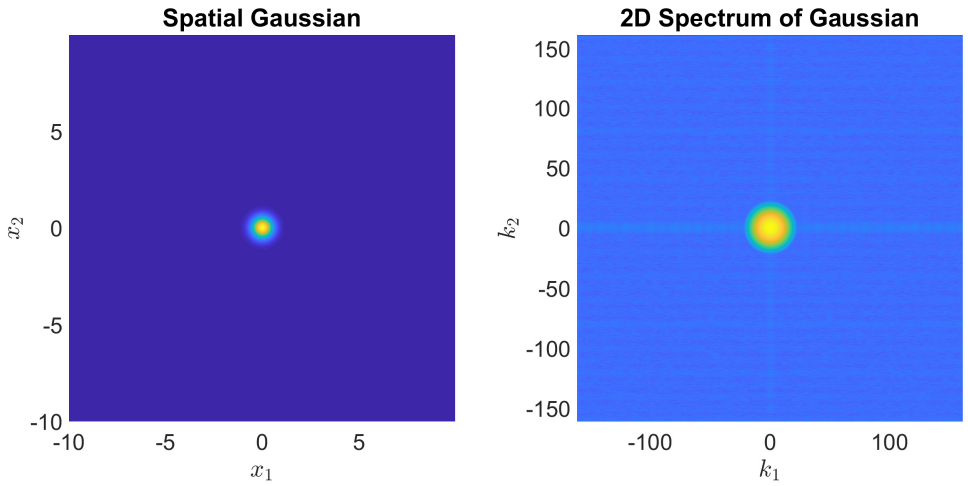

Figure 4.8: Spatial and spectral discretizations of a Gaussian projection.

The *Gibbs-Wilbraham Phenomenon* is another detrimental effect of FTs of discontinuous functions (See for example [23]). The infinite series of sinusoids approximating the discontinuous jump converges with a significant overshoot, leading to ringing artifacts along each spectral axis $k_{1,2}$ - apparent in the spectral cross-sections of the disk and rectangle (Figure 4.3 and 4.4).

Continuous PPA Design

The Gibbs-Wilbraham phenomenon and spatial aliasing form two arguments towards the use of continuous pole distribution functions. A third argument is that PPAs in reality do not (in general) mirror the shape of the face of the magnet pole, due to fringing of the magnetic field lines. Hence, continuous approximations of the disk and rectangle shapes may be used to emulate this. The Heaviside step-function can be expressed continuously by the *logistic* approximation:

$$\Theta(y) \approx \tilde{\Theta}(y) = \frac{1}{2} + \frac{1}{2}\tanh(\alpha y), \quad \alpha > 0 \tag{4.14}$$

Where the parameter α dictates the sharpness of the curve. The logistic Heaviside function yields the following continuous approximations for the disk and rectangle PPAs:

$$\tilde{P}^{\text{disk}}_{1,2,z}(\mathbf{x}) = \frac{1}{2} + \frac{1}{2}\tanh\left(\alpha\Big[r - \|\text{diag}\{a,b\}(\mathbf{x}-\mathbf{x}_0)\|_2\Big]\right) \tag{4.15}$$

$$\tilde{P}^{\text{rect}}_{1,2,z}(\mathbf{x}) = \frac{1}{2} + \frac{1}{2}\tanh\left(\alpha\Big[r - \|\text{diag}\{a,b\}(\mathbf{x}-\mathbf{x}_0)\|_\infty\Big]\right) \tag{4.16}$$

Alternatively, a convolution with a smoothing function such as the Gaussian can be used:

$$\tilde{P}_{1,2,z}(\mathbf{x}) = P^{Gauss}_{1,2,z}(\mathbf{x}) * P_{1,2,z}(\mathbf{x}) \Rightarrow \hat{\tilde{P}}_{1,2,z}(\mathbf{k}) = \hat{P}^{Gauss}_{1,2,z}(\mathbf{k})\hat{P}_{1,2,z}(\mathbf{k}) \tag{4.17}$$

4.3 Inverse DFT Periodicity

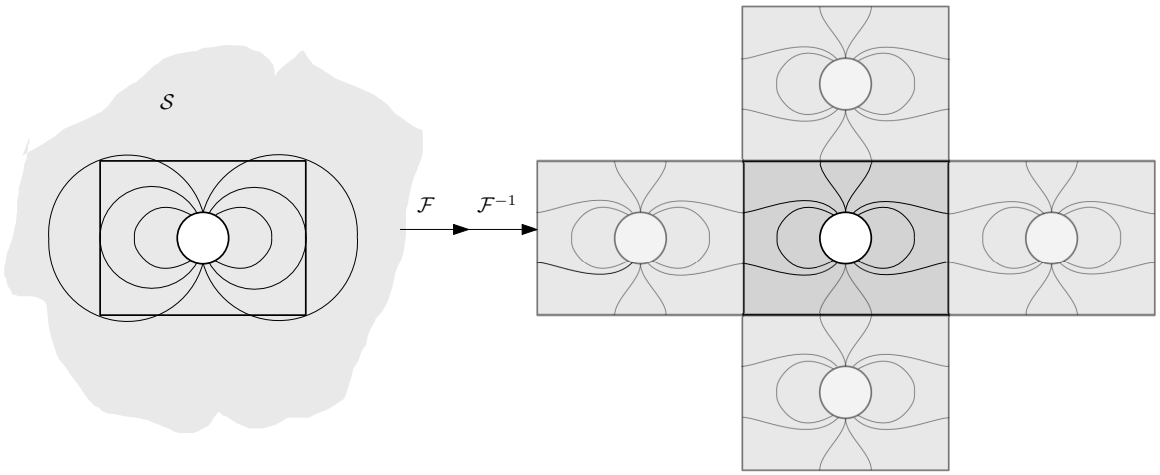

Figure 4.9: Periodic interference of eddy currents.

As previously stated, the DFT (4.5) imposes a periodicity on its inverse transform (IDFT). Let us consider a disk shaped magnetic PPA in which a nonzero controlled field is affecting the sheet. The sheet is moving with a velocity $\mathbf{v}$ relative to the PPA - this describes an ECB system. A section of the sheet with the PPA fixed at its center is being sampled through a grid parametrized by lengths $L_{1,2}$ and resolutions $N_{1,2}$. Periodic boundaries of this configuration implies that the rectangular section with the centered PPA is surrounded by infinitely repeating identical ECB systems (Figure 4.2): The IDFT of the configuration is $L_{1,2}$-periodic about its respective axes. At first glance, this periodicity does not seem like it can be attributed to a physical process. It is also easy to see how the periodicity can lead to unphysical results if the grid is not large enough to contain the induced eddy-current return paths (Figure 4.9). This would lead to interference between the actual ECB with the surrounding imagined ECBs. Specifically, eddy-currents will flow through the sides of the rectangular section as if converging to or diverging from surrounding systems. Thus, the periodicity is generally considered negligible at best - for a properly designed sampling grid, and detrimental at worst. In the following subsection we will investigate some periodic configurations where we can possibly exploit the periodicity of the IDFT.

4.3.1 Periodic ECB Configurations

By considering the grid a planar mapping of the points of a periodic surface, the periodic boundary conditions of the IDFT are satisfied, while describing a physical system. A not so

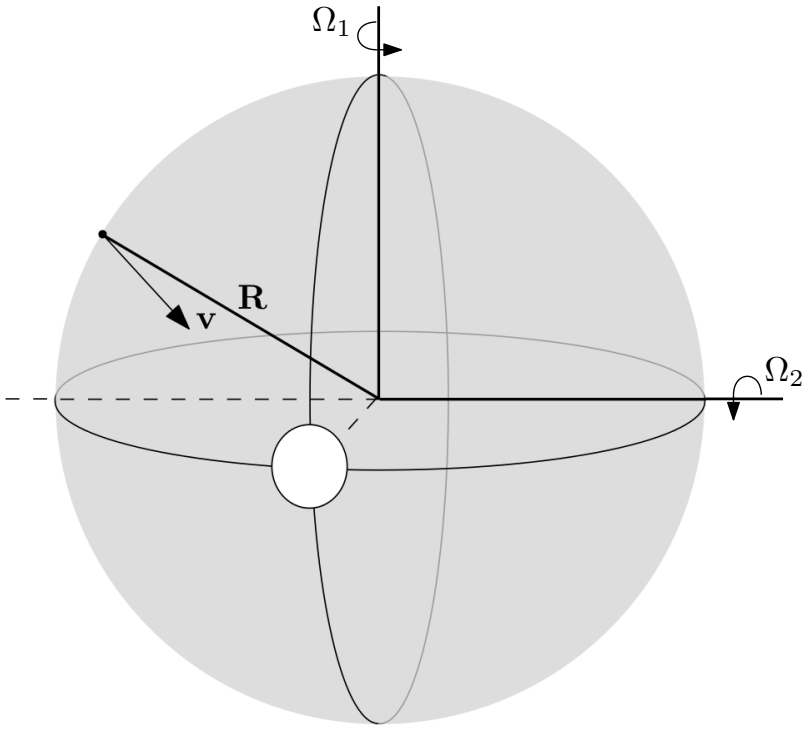

Figure 4.10: Moving sheet represented by a spheroid rotating about two of its axes.

useful example is when the real world application being represented by the FET is periodic in both planar directions. In this case, the periodic grid could represent a spheroid (Figure 4.10). Consider instead the case where the sheet is only moving along the x_1-axis, and L_2 is chosen large enough such that the effect of the imposed periodicity along the x_2-axis is negligible. In this case, the resulting system will be a strip of length L_1 and height L_2, L_1-periodic along x_1. "Connecting" the ends of the strip would yield a planar, rotating ring-surface (Figure 4.11) with mean circumference equal to L_1. With this perspective, one can argue that the solution of the ECB system in linearly translating strips can be extended to rotating disks under the right circumstances. The braking torque can be calculated directly from the drag force:

$$M(t) = D_1(t)R \tag{4.18}$$

We must reconcile, however, that neither the sphere nor ring shapes are isometric to the plane [24, ch.1]. This means that the transformation visualized in (Figure 4.11) is not continuous, i.e. it cannot be done without stretching or tearing the strip. The planar representations of such shapes typically have significant distortions, such as close to the poles for the sphere, which the rectangular sampling grid cannot account for.

While the goal of this section is simply to convince the reader that the periodicity of the

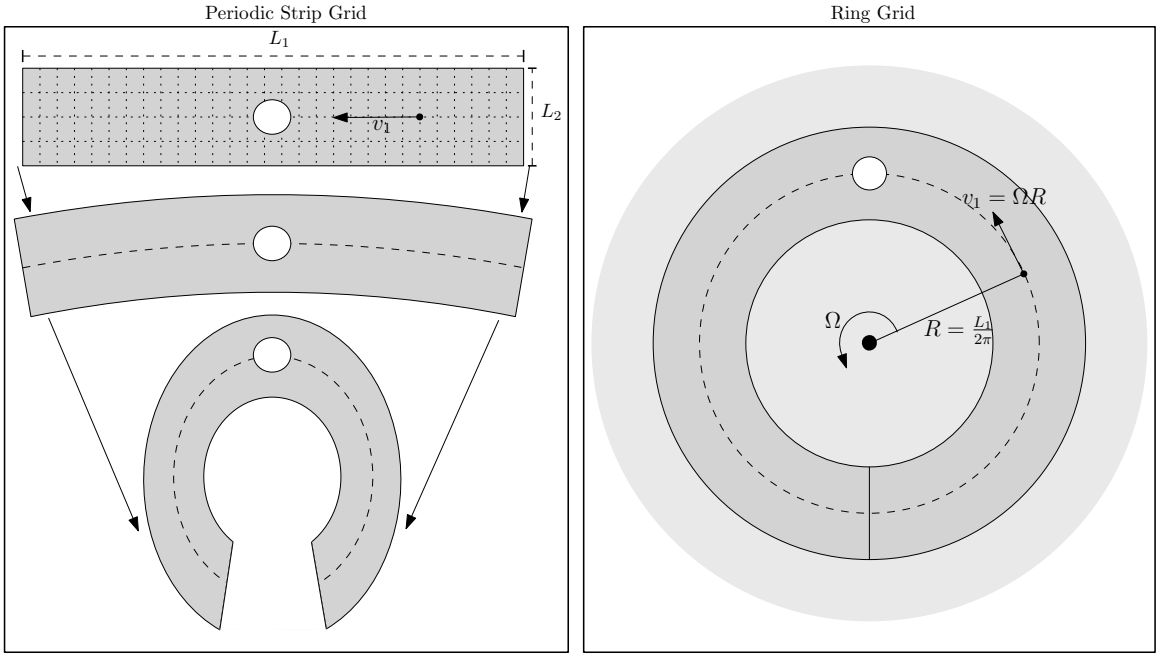

Figure 4.11: Sampling grids in the form of long, periodic strips describing a ring of finite radius on a larger rotating conductive sheet.

solution can be exploited to extend the ECB solution from the linear case to rotating disks, a realizable case is desirable. Consider instead the case where the periodic strip is folded inwards such that it forms a cylinder (Figure 4.12). The cylinder is isometric to the plane, hence the points on the cylindrical surface correspond to the points on the strip. This permits the interpretation of the periodic strip as the surface of a cylinder rotating about a fixed axis. The braking torque generated about this axis can be found by (4.18).

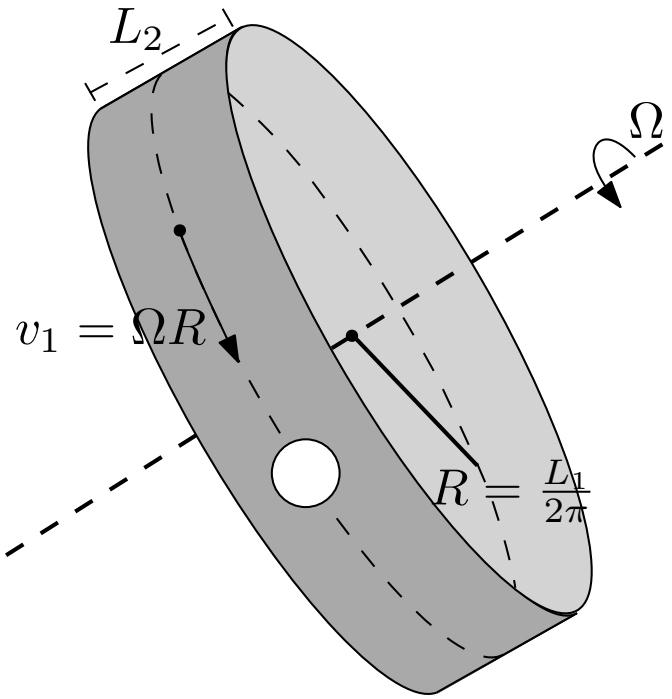

Figure 4.12: Periodic strip in the form of a rotating cylinder.

Chapter 5

ECB Model Analysis and Simulation

In this chapter, the spectral numerical method is applied to the derive ECB model and its accuracy is examined in detail for several configurations. The numerical solution is found to agree with existing stationary braking force models, and frequency analysis of the dynamic behaviour yields some interesting findings regarding its phase, bandwidth and the existence of accelerating input frequencies. The latter two are validated by simulation of the penultimate discrete model.

5.1 Implementation and Validation

Recall, the discrete ECB model seen from the magnet:

$$\frac{\partial}{\partial t}\hat{B}_z[\mathbf{K},t] = \left(i\mathbf{K}^\intercal\dot{\mathbf{r}} - \nu|\mathbf{K}|\right)\hat{B}_z[\mathbf{K},t] + \nu|\mathbf{K}|\hat{C}_z[\mathbf{K},t] \tag{5.1a}$$

$$\hat{\psi}[\mathbf{K},t] = \frac{1}{b\mu_0|\mathbf{K}|}\left(\hat{B}_z[\mathbf{K},t] - \hat{C}_z[\mathbf{K},t]\right) \tag{5.1b}$$

$$\mathbf{D}(t) = \frac{2b}{L_1L_2}\sum_{K_1}\sum_{K_2}\hat{\psi}^*[\mathbf{K},t]\begin{bmatrix}-i\mathbf{K}\hat{B}_z[\mathbf{K},t]\\ i\mathbf{K}^\intercal\hat{\mathbf{\Gamma}}[\mathbf{K},t]\end{bmatrix} \tag{5.1c}$$

For simplicity, the succeeding solutions are based on the sheet translation of constant velocity along only the x_1-axis:

$$\mathbf{r} = \begin{bmatrix}r_1(t)\\0\end{bmatrix}, \quad \dot{\mathbf{r}} = \begin{bmatrix}v_1\\0\end{bmatrix}$$

The numerical solutions of (4.8) presented in this chapter were implemented in MATLAB using the functions *fftn()* and *ifftn()* - forward and inverse FFT algorithms generalized to n-dimensional DFTs, based on the FFTW library [25]. We aim to make an assessment of the numerical solution based on the error percentage,

$$e = \frac{|D_{numeric} - D_{analytic}|}{|D_{analytic}|} \cdot 100\% \tag{5.2}$$

to establish the optimal sampling grid parameters.

5.1.1 Stationary Solution

We begin by investigating the stationary behaviour of the numerical solution of (5.1). Note that since the translation of the sheet seen from the magnet is only along the x_1-axis, the braking force is contained in the drag-component of the damping vector, D_1. We are not concerned with the lift force D_z. Hence, the stationary discrete model being implemented is given by:

$$\bar{\hat{B}}_z[\mathbf{K}] = \frac{\nu|\mathbf{K}|}{iK_1v_1 - \nu|\mathbf{K}|}\hat{C}_z[\mathbf{K}] \tag{5.3a}$$

$$\bar{D}_1 = \frac{2b}{L_1L_2}\sum_{K_1}\sum_{K_2}\bar{\hat{\psi}}^*[\mathbf{K}](-iK_1\bar{\hat{B}}_z[\mathbf{K}]) \tag{5.3b}$$

Where the vertical controlled field is is of constant strength and centered at $\mathbf{x}_0 = \mathbf{0}$:

$$\hat{C}_z[\mathbf{K}] = q\hat{P}_z[\mathbf{K}]$$

We have a wide selection of well documented analytical and empirical results on which to base our stationary analysis (Section 2.3). We have shown that Reitz' [6] stationary drag force model agrees with the analytical solution of the stationary ECB monopole system (3.57):

$$\bar{D}_1^{mono} = \frac{q^2}{16\pi h^2\mu_0}\left(\frac{v_r}{1 + v_r^2 + \sqrt{1+v_r^2}}\right) \tag{5.4}$$

Thus, we may use this analytical result as source of validation for the numerical solution with vertical controlled field:

$$\hat{C}_z^{mono}[\mathbf{K}] = q\hat{\mathbf{P}}_z^{mono}[\mathbf{K}] = -\text{sgn}(h)q\frac{e^{-|\mathbf{K}||h|}}{2} \tag{5.5}$$

After evaluating whether the numerical solution (5.3) agrees with analytical models or not, we proceed by investigating the physical properties of the magnetic field and eddy-currents.

In particular, we expect to find a significant demagnetization for high values of v_1, and in-plane currents that form loops in/out of the PPA. A disk shaped PPA configuration will be used for this purpose, which most theoretical [12], experimental [13], and numerical results are based on. As monopoles do not exist in nature (2.1), existing literature on induced fields and currents with the monopole configuration is limited to theoretical results [7].

Since the FT of the monopole distribution is a relatively simple expression, analytical solution of the damping force integral (3.49) is possible. The same cannot be said for the disk pole expression:

$$\hat{C}_z^{disk}[\mathbf{K}] = 2\pi q \frac{RJ_1(R\chi)}{\chi} e^{-|\mathbf{K}||h|} \tag{5.6}$$

To the knowledge of the author, there exists no analytical stationary braking force models for the disk shaped magnet that captures the asymptotic behaviour for low and high speeds. However, recall that the linear model(s) derived in [8, 9, 12],

$$\bar{D}_1^{linear} = \pi\sigma r^2 d B_0^2 c v_1 \tag{5.7}$$

accurately predict(s) the linear behaviour of the ECB for a disk shaped PPA of radius r and small values of v_1. A naive approach is to extend (5.4) to disk shaped PPAs by fitting its 1. order Taylor Expansion about $v_1 = 0$ [2],

$$\bar{D}_1^{mono} = \frac{q^2}{16\pi h^2 \mu_0}\left(\frac{v_r}{2} + \mathcal{O}(2)\right) \approx \frac{q^2}{16\pi h^2 \mu_0} \cdot \frac{v_r}{2} \tag{5.8}$$

to the linear model (5.7) by matching parameters:

$$\begin{aligned} q^2 &= 16\pi^2 h^2 (2r)^2 c B_0^2 \\ \Rightarrow \bar{D}_1^{disk} &= \frac{4\pi r^2 c}{\mu_0} B_0^2 \left(\frac{v_r}{1 + v_r^2 + \sqrt{v_r^2 + 1}}\right) \end{aligned} \tag{5.9}$$

We will refer to (5.9) as the analytical model for the ECB with a disk shaped PPA, where we use a controlled field with zero fringing:

$$\mathbf{C}^{disk}[\mathbf{X}] = q \begin{bmatrix} 0 \\ 0 \\ P_z^{disk}[\mathbf{X}] \end{bmatrix} \tag{5.10}$$

A final point of validation of our solution is the critical recession angle (2.20) according to [12]:

$$\angle \boldsymbol{\nu}_{cr} = \sqrt{2c\xi}\sqrt{\frac{r}{l_g}} \tag{5.11}$$

Where the airgap length l_g is given by the sum of the sheet thickness and the suspension height of the magnet:

$$l_g = d + h \tag{5.12}$$

5.1.2 Dynamic Solution

We may proceed with the dynamic analysis once the numerical method for the stationary case is in order. We introduce the temporal forward and inverse Fourier Transforms,

$$\mathcal{F}_t\big(f(t)\big) = \int_{-\infty}^{\infty} f(t)e^{-i\omega t}dt = f^{(\omega)}(\omega) \tag{5.13a}$$

$$\mathcal{F}_t^{-1}\big(f^{(\omega)}(\omega)\big) = \frac{1}{2\pi}\int_{-\infty}^{\infty} f^{(\omega)}(\omega)e^{i\omega t}d\omega = f(t) \tag{5.13b}$$

in order to investigate the ECB solution frequency response. Applying (5.13) to the net magnetic field dynamics:

$$\begin{aligned}
\frac{\partial}{\partial t}\hat{B}_z &= (ik_1v_1 - \nu|\mathbf{k}|)\hat{B}_z + \nu|\mathbf{k}|\hat{C}_z \\
&\quad\ \mathcal{F}_t(\cdot) \Downarrow \\
i\omega\hat{B}_z^{(\omega)} &= (ik_1v_1 - \nu|\mathbf{k}|)\hat{B}_z^{(\omega)} + \nu|\mathbf{k}|\hat{C}_z^{(\omega)} \\
\hat{B}_z^{(\omega)} &= \frac{\nu|\mathbf{k}|}{i(\omega - k_1v_1) - \nu|\mathbf{k}|}\hat{C}_z^{(\omega)} \\
\Rightarrow \hat{\psi}^{(\omega)} &= \frac{1}{b\mu_0|\mathbf{k}|}\left(\frac{\nu|\mathbf{k}|}{i(\omega - k_1v_1) + \nu|\mathbf{k}|} - 1\right)\hat{C}_z^{(\omega)} \\
&= \frac{1}{b\mu_0|\mathbf{k}|}\left(\frac{-i(\omega - k_1v_1)}{i(\omega - v_1k_1) + \nu|\mathbf{k}|}\right)\hat{C}_z^{(\omega)}
\end{aligned}$$

Where the controlled field FT is given by:

$$\hat{\mathbf{C}}^{(\omega)} = \begin{bmatrix}\hat{\mathbf{\Gamma}}^{(\omega)} \\ \hat{C}_z^{(\omega)}\end{bmatrix} = q^{(\omega)}\begin{bmatrix}\hat{P}_1 \\ \hat{P}_2 \\ \hat{P}_z\end{bmatrix}$$

In existing publications on ECBs, little attention has been paid to the nature of the force dynamics. Thus, unlike the stationary case, we do not have any analytical results on which to base our analysis. In our case, an analytical solution to the frequency ECB response requires solving:

$$\begin{aligned}
\mathbf{D}^{(\omega)} &= \frac{2b}{(2\pi)^2}\int_{\mathbb{R}^2}\hat{\psi}^{(\omega)*}\begin{bmatrix}-i\mathbf{k}\hat{B}_z^{(\omega)} \\ i\mathbf{k}^\intercal\hat{\mathbf{\Gamma}}^{(\omega)}\end{bmatrix}d\mathbf{k} \\
&= \frac{2b}{(2\pi)^2}\int_{\mathbb{R}^2}\frac{1}{b\mu_0|\mathbf{k}|}\frac{i(\omega - k_1v_1)}{-i(\omega - k_1v_1) + \nu|\mathbf{k}|}\hat{C}_z^{(\omega)*}\begin{bmatrix}-i\mathbf{k}\frac{\nu|\mathbf{k}|}{i(\omega - k_1v_1) + \nu|\mathbf{k}|}\hat{C}_z^{(\omega)} \\ i\mathbf{k}^\intercal\hat{\mathbf{\Gamma}}^{(\omega)}\end{bmatrix}d\mathbf{k}
\end{aligned}$$

Separated into in-plane drag-, and lift-forces:

$$D_{1,2}^{(\omega)} = \frac{2b}{(2\pi)^2}\int_{\mathbb{R}^2}\frac{1}{b\mu_0|\mathbf{k}|}\frac{(\omega-k_1v_1)k_{1,2}\nu|\mathbf{k}|}{(\omega-k_1v_1)^2+\nu^2|\mathbf{k}|^2}|\hat{C}_z^{(\omega)}|^2 d\mathbf{k} \tag{5.14a}$$

$$D_z^{(\omega)} = \frac{2b}{(2\pi)^2}\int_{\mathbb{R}^2}\frac{1}{b\mu_0|\mathbf{k}|}\frac{-(\omega-k_1v_1)\left(k_1\hat{C}_1^{(\omega)}+k_2\hat{C}_2^{(\omega)}\right)}{(\omega-k_1v_1)^2+\nu^2|\mathbf{k}|^2}\hat{C}_z^{(\omega)*}d\mathbf{k} \tag{5.14b}$$

Solution attempts of (5.14) both by hand and by the help of digital computing tools such as Wolfram Mathematica were unsuccessful, even for the monopole distribution. Nevertheless, the integrands holds useful information about the force vector dynamics. An interesting property of the in-plane drag forces is that their frequency response is purely real valued. This means that the transfer function from the controlled field (input) to the in-plane drag forces (output) is zero-phase, and we expect the drag forces to be able to follow a reference trajectory without lagging behind - a desirable trait. In general, the same cannot be said for the lift force - which phase depends on the distribution of the controlled field. For a monopole (4.13), the lift-force FT integrand is given by:

$$f_z^{(\omega)} = \frac{\text{sgn}(h)}{4b\mu_0|\mathbf{k}|^2}\frac{-i(\omega-k_1v_1)\,(k_1^2+k_2^2)}{(\omega-k_1v_1)^2+\nu^2|\mathbf{k}|^2}e^{-2|\mathbf{k}||h|}|q^{(\omega)}|^2 \tag{5.15}$$

Integration over the real plane $\mathbf{k}\in\mathbb{R}^2$ will not change the phase properties.

T-symmetry of D

T-symmetric or *time-reversal invariant* functions are functions that are even in time:

$$g(-t) = g(t)$$

Consider the real-valued, time-varying current density and magnetic field vectors:

$$\mathbf{J}(\boldsymbol{\xi},t),\quad \mathbf{B}(\boldsymbol{\xi},t)$$

In classical physics, it is well documented that **J** and **B** are *odd* in time,

$$\mathbf{J}(-t) = -\mathbf{J}(t),\quad \mathbf{B}(-t) = -\mathbf{B}(t)$$

however: Due to the cross product term of these vectors in (2.8), the Lorentz force is T-symmetric:

$$\mathbf{f}(\boldsymbol{\xi},-t) = \mathbf{S}(\mathbf{J}(-t))\mathbf{B}(-t) = \mathbf{S}(\mathbf{J}(t)\mathbf{B}(t) = \mathbf{f}(\boldsymbol{\xi},t)$$

Since this property is preserved for the volume integral of **f** uncovering **D**, the braking forces are necessarily T-symmetric as well:

$$\mathbf{D}(-t) = \mathbf{D}(t) \tag{5.16}$$

An approximation of the temporal FT of **D** is uncovered by solving the integral (5.14) numerically, and can be used to verify the necessary condition on our solution of the braking force by preservation of its T-symmetry. This is given by the symmetry property of the Fourier transform [15]:

$$g(t) \in \mathbb{R} \Leftrightarrow g^{(\omega)}(-\omega) = g^{(\omega)}(\omega)^*$$

And likewise:

$$g^{(\omega)}(\omega) \in \mathbb{R} \Leftrightarrow g(-t) = g(t)^* \tag{5.17}$$

Since $\mathbf{D}(t)$ is a real valued, T-symmetric vector, it satisfies (5.17). Consequently:

$$\mathbf{D}^{(\omega)}(\omega) \in \mathbb{R}^3 \tag{5.18}$$

Given this consideration, the purely real frequency responses (5.14) is actually expected. However, this does not agree with the result for the frequency response (5.14), which shows a complex-valued lift force.

Parameter	Value	Comments
μ_0	$4\pi \times 10^{-7}\mathrm{Wb}\,(\mathrm{A\ m})^{-1}$	Vacuum permeability
μ	$\simeq 4\pi \times 10^{-7}\mathrm{Wb}\,(\mathrm{A\ m})^{-1}$	Aluminium sheet permeability
σ	$3.77 \times 10^{-7}\mathrm{S\ m}^{-1}$	Aluminium sheet conductivity
d	$2.00 \times 10^{-2}\mathrm{m}$	
r	$1.00\mathrm{m}$	PPA radius for non-monopole configurations
a/b	1.00	Equal axial scaling of the PPA shapes
$\mathbf{x}_0$	$[0\ \ 0]^\intercal$	PPAs centered at the origin
c	0.50	Compensation factor for non-monopole PPAs centered on infinite surface (2.15)
ξ	1.00	Unitary proportionality factor
q	$1.00 \times 10^{-2}\mathrm{Wb}$	Constant controlled field strength
$\angle\boldsymbol{\nu}$	45^o	Fixed speed $v_1 = \nu$
Δt	$1.00 \times 10^{-4}\mathrm{s}$	

Table 5.1: Mathematical constants and parameters used for the ECB system during stationary and dynamical analysis, and simulation.

5.2 Stationary Analysis

For the following numerical analysis, we let a *square* sampling grid be defined by,

$$(L_1, L_2) = (L, L) \tag{5.19a}$$
$$(N_1, N_2) = (N, N) \tag{5.19b}$$

reducing the dimension of the analysis. All parameters of the system are given by (Table 5.1), unless otherwise stated. Please note that the parameters values used are not entirely realistic - there are few applications that warrant a magnetic PPA of radius $1\mathrm{m}$, for instance. The parameters are presented strictly for transparency, and were chosen with no real world application in mind. We are concerned with validating our solution with analytical models, and not verification with experimental results for the time being. Objectives of the following stationary analysis is: (*i*) Force/speed curve validation with analytical models, (*ii*) establishing the limitations of the numerical method, (*iii*) verification of physical properties.

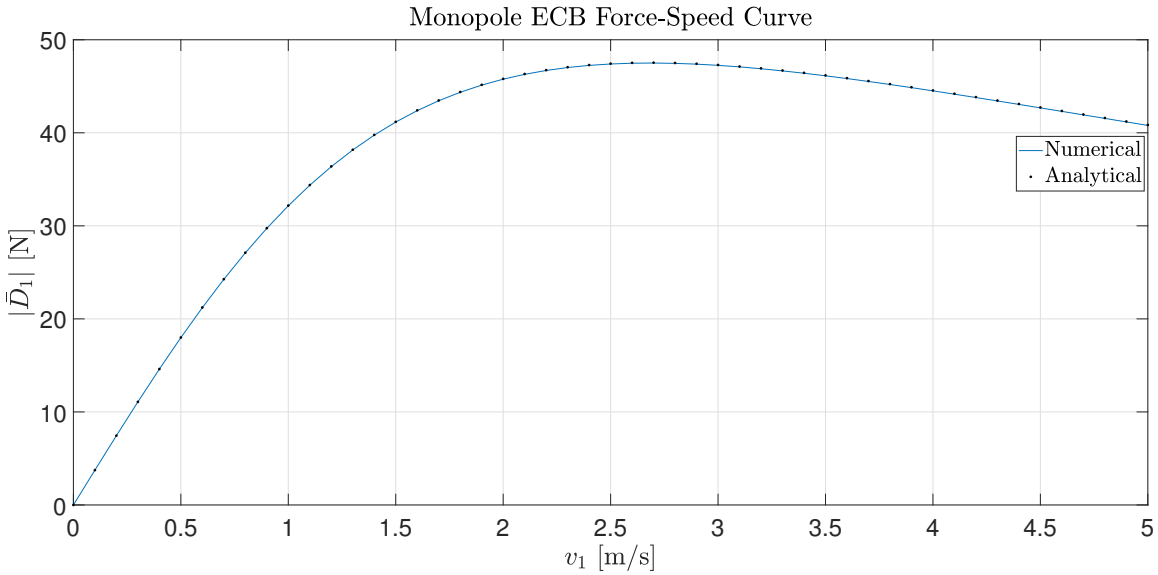

Figure 5.1: Validation of the force-speed curve of the analytical stationary monopole ECB. The monopole is suspended at $h = 0.10\text{m}$ and the sheet velocity is $v_1 = \nu$.

5.2.1 Numerical Analysis

The most important result of the numerical analysis is presented in (Figure 5.1), where for a sampling grid defined by,

$$(L_1, L_2) = (20, 20)\,, \quad (N_1, N_2) = \left(2^8, 2^8\right)$$

the numerical drag force solution agrees with the analytical result for monopoles (5.4). However, we observe that the same sampling grid does not in general lead to accurate solutions for varying monopole heights. In order to investigate the impact of the sampling grid parameters on the numerical accuracy according to (5.2), we let L and N be iterated over a range of values.

Firstly, the impact of the grid step-size

$$H = \frac{L}{N} \tag{5.20}$$

was investigated for an arbitrary set of small to large monopole heights
$h \in \{0.01\text{m}, 0.10\text{m}, 1.00\text{m}\}$. It is clear from (Figure 5.2) that the impact of L and N must be investigated individually, as the same values of H lead to differing results, especially apparent for the larger pole height. H seems to be a good predictor of the numerical accuracy for small heights, however.

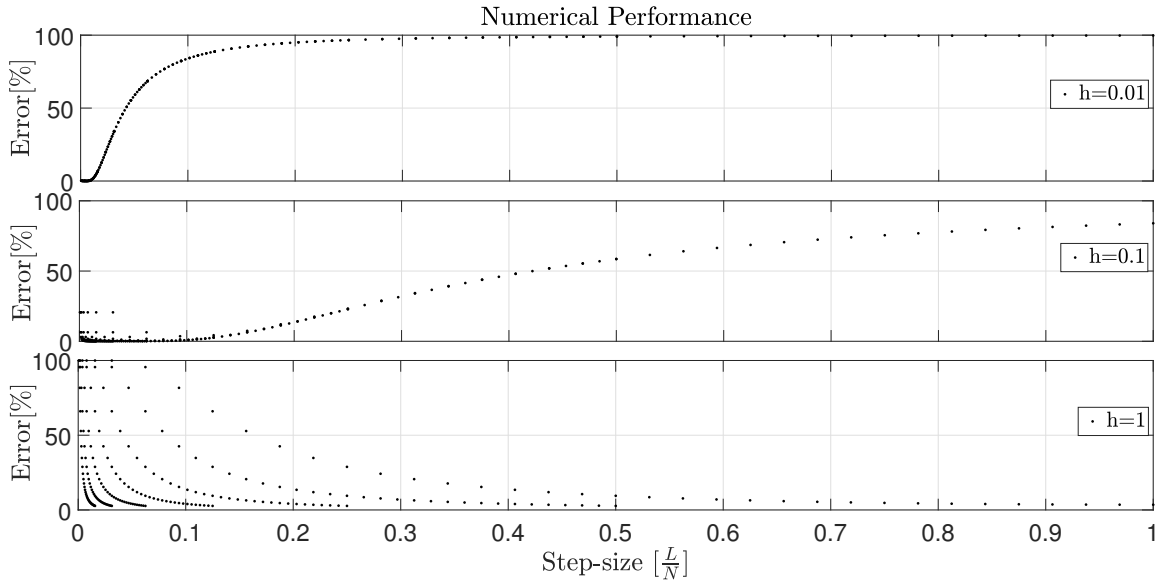

Figure 5.2: Numeric error scatter plot for the stationary monopole ECB system at fixed $v_1 = \nu$ and various heights, for a range of sampling grid parameters.

We find that L and N may be chosen according to color scale plots (Figure 5.3), unique to each pole height, for instance we can see that (close to) minimal sampling grid resolution required for an accurate numerical solution for $h = 0.10\mathrm{m}$ is given by:

$$(L, L) = (6, 6)\,, \quad (N, N) = \left(2^6, 2^6\right) \tag{5.21}$$

The significance of the magnetic pole elevation on the requirements on the parameters of the numerical method could make it unsuitable for applications where this is a time-varying parameter, such as in magnetic levitation. We find by investigating corresponding color scale error plots for various heights, that larger h require larger spatial dimensions L while smaller h require small step-sizes. Applications where h is time-varying therefore require L large enough for its upper magnitude threshold, and step-sizes small enough for its lower magnitude threshold. This potentially puts extremely high requirements on the resolution N, resulting in slow computations which partly defeats the purpose of the spectral numerical method. Interestingly, the requirements on the sampling grid are hardly affected by the relative velocity of the sheet and magnet (Figure 5.4) - consistent for the various pole heights.

As previously stated, the specific sampling grid

$$(L_1, L_2) = (20, 20), \quad (N_1, N_2) = (2^8, 2^8)$$

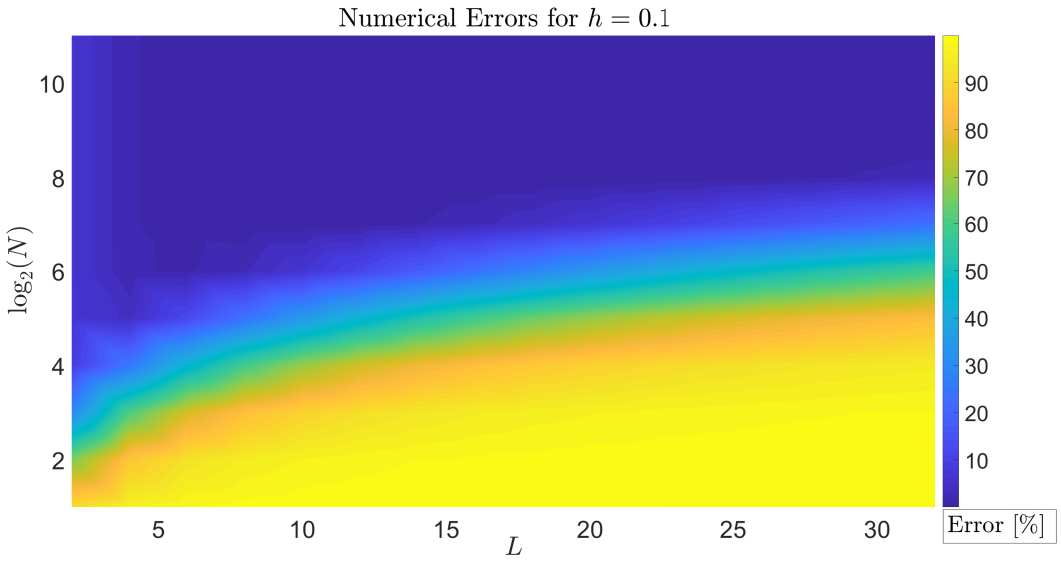

Figure 5.3: Color scale plot showing the numeric error of the monopole ECB system at fixed height for a range of sampling grid parameters.

happens to yield a valid numerical solution of the brake force for monopole height $h = 0.10\text{m}$ (Figure 5.5), but results in a poor approximation for $h = 0.01\text{m}$ (Figure 5.6) and $h = 1.00\text{m}$ (Figure 5.7). An intuitive understanding of why certain sampling grid parameters lead to poor approximation (Figure 5.2) of the braking force can be gained by investigating the underlying stationary field-, and stream-functions for these cases.

The characteristics of a well designed sampling grid for a given pole height can be seen in (Figure 5.5). Significant return paths of the induced currents are contained in the bounded spatial plane, and the same goes for the significant frequency components of its corresponding magnetic field. We can see that L might be unnecessarily large and/or N is slightly too small, as the solution is close to having significant aliasing. Regardless, this is not reflected in the braking force (Figure 5.1).
Severe aliasing is present for the lowest pole elevation (Figure 5.6), however. It is clear that the closer to the sheet surface the monopole is placed, the smaller an area it affects. As a result, induced currents are circulating a smaller region of the sheet, with higher density. This corresponds to large spatial frequency components, as evident in (Figure 5.6). For the current sampling grid, the solution is aliased heavily, manifesting as pixelation and distortion of the current return paths.
Finally, the opposite effect can be seen for the largest pole elevation (Figure 5.7). The induced current return paths are more spread out and circulate further into the plane due to

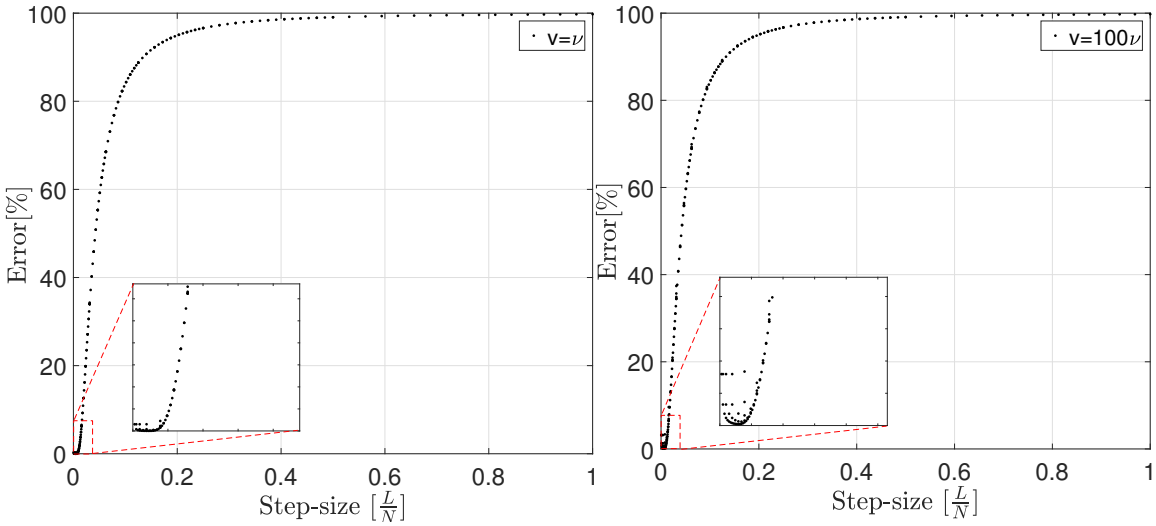

Figure 5.4: Numeric error scatter plot for the monopole system at fixed $h = 0.01\text{m}$ and various velocities, for a range of sampling grid dimensions and resolutions.

the larger area affected by the pole. The current choice of grid dimensions L is too small to capture all significant return paths and as a consequence we observe interference due to the periodic boundary conditions. This corresponds to a spectrum where the frequency resolution is too small to distinguish significant frequency components.
To summarize, there exists no single sampling grid design suitable for all values of h because of the inverse relationship between the spatial and spectral planes (i.e. uncertainty principle).

We now turn our attention to the stationary drag force solution for a disk shaped PPA. We find that a sampling grid given by

$$(L_1, L_2) = (50, 80)\,, \quad (N_1, N_2) = \left(2^8, 2^8\right) \tag{5.22}$$

yields a solution that agrees with the analytical model (Figure 5.8) for a disk pole placed directly onto the sheet surface. The square sampling grid was replaced with a larger, rectangular grid that ensuring that significant current return paths do not diverge along the x_2-axis in our solution, which was found to worsen the numerical accuracy (Figure 5.7). The PPA of radius $r = 1.00\text{m}$ is larger than that of the monopole, which is why the required dimensions of the sampling grid have increased. Despite the concerns regarding aliasing in (Section 4.2.2), the discontinuous disk PPA was used - with negligible consequences.

A validation attempt was made of the critical recession angle (2.20) according to the theoretical results in [12]. The result (Figure 5.9) shows that the critical recession angle of

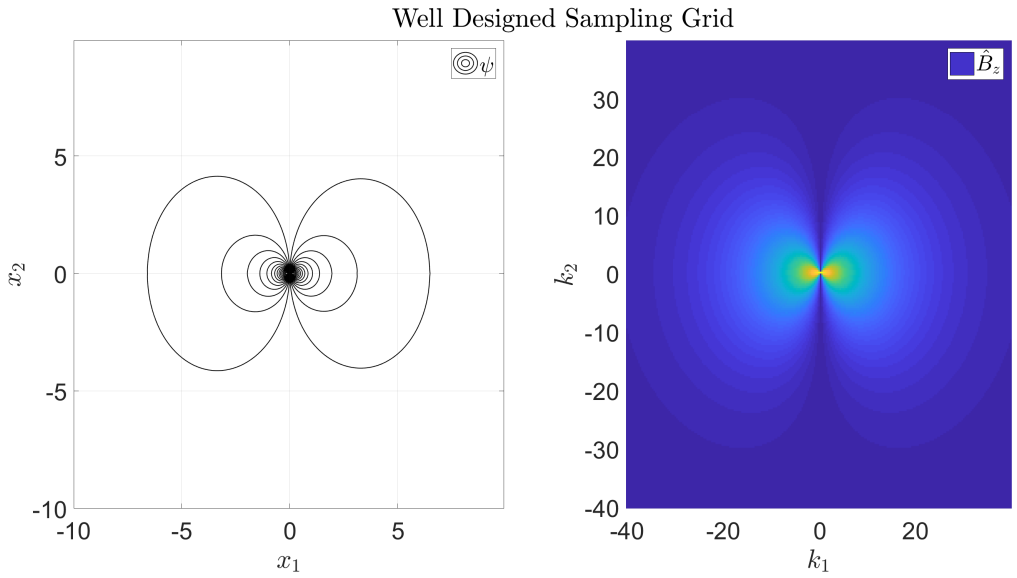

Figure 5.5: Stationary induced current return paths (left) and their induced magnetic field spectrum (right) for $h = 0.10\text{m}$.

the numerical solution not only does not agree with the theoretical result, but does not vary with either the PPA radius or the air-gap length.

5.2.2 Stationary Eddy Current Behaviour

The stationary behaviour of the in-plane eddy currents (Figure 5.10) and the magnetic field they generate (Figure 5.11) was investigated for various sheet velocities: (*i*) Near standstill, (*ii*) $v_1 = \nu$, and (*iii*) high velocity. Please note that the sheet is moving from right to left relative to the fixed PPA.
We observe that for very low velocities (*i*), the eddy currents form return paths that are symmetrical about both axes in the plane, and their induced magnetic fields are negligible compared to the external field of the PPA. This corresponds to a dominant linear behaviour of the drag force, which can be seen in (Figure 5.8) and which agrees with the findings in [8, 9] where the assumption of symmetrical currents and small induced magnetic fields lead to a linear drag force model (5.7).
As the sheet velocity increases (*ii*), the eddy currents form a sort *tail* behind the PPA - almost as if the disk is moving through water. This is what the eddy currents look like corresponding to the strongest region of the drag-force/speed curve - the induced fields are large enough to create a significant damping force, but not large enough to cause significant demagnetization in the PPA (Figure 5.12).

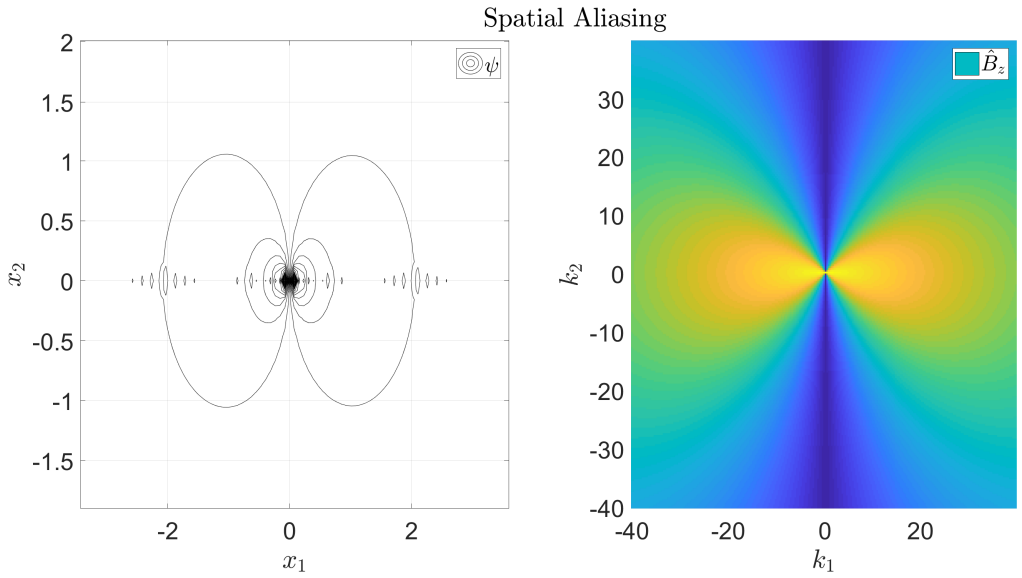

Figure 5.6: Stationary induced current return paths (left) and their induced magnetic field spectrum (right) for $h = 0.01\text{m}$.

The tail grows longer the larger the relative velocity (*iii*) between the sheet and pole, and for a periodic surface it will eventually return to the PPA from the other side. The net magnetic field is nearly entirely demagnetized in this case, and is spread out over most of the sheet length. As a result the drag forces are approaching zero, as predicted by [8, 12] and verified experimentally in [13]. See (Figure 2.4) for an experimental result with which to compare the demagnetization observed in the numerical solution (Figure 5.12).

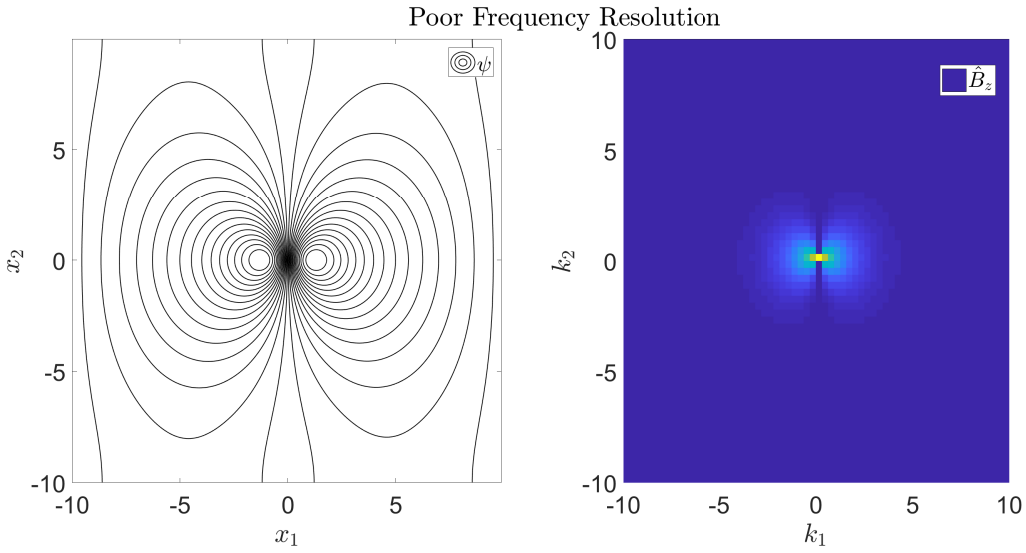

Figure 5.7: Stationary induced current return paths (left) and their induced magnetic field spectrum (right) for $h = 1.00\text{m}$.

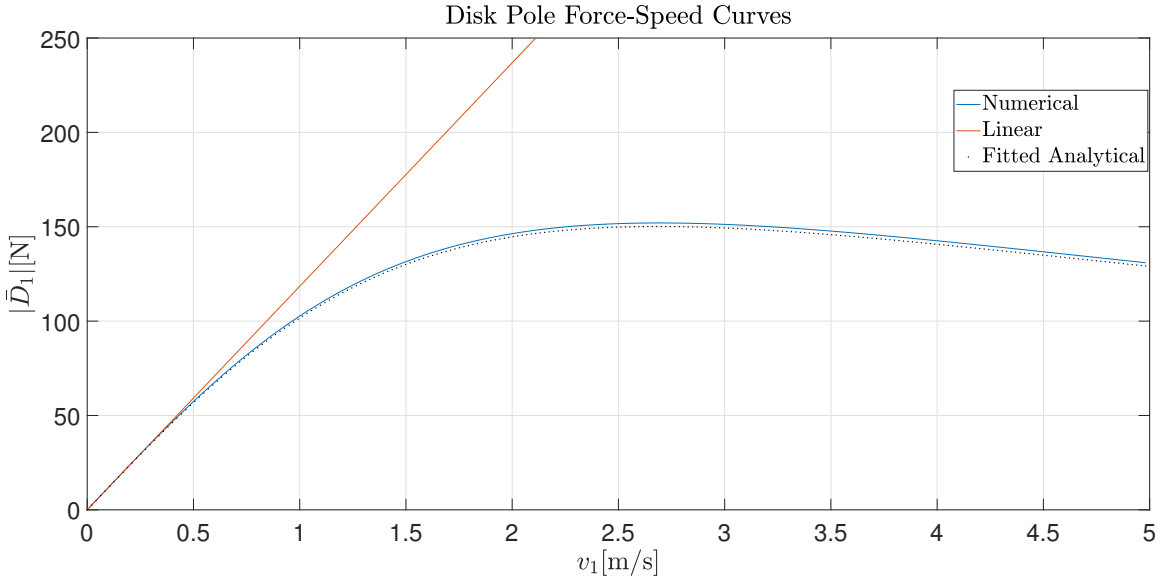

Figure 5.8: Disk pole drag force validation for $h = 0.00\text{m}$.

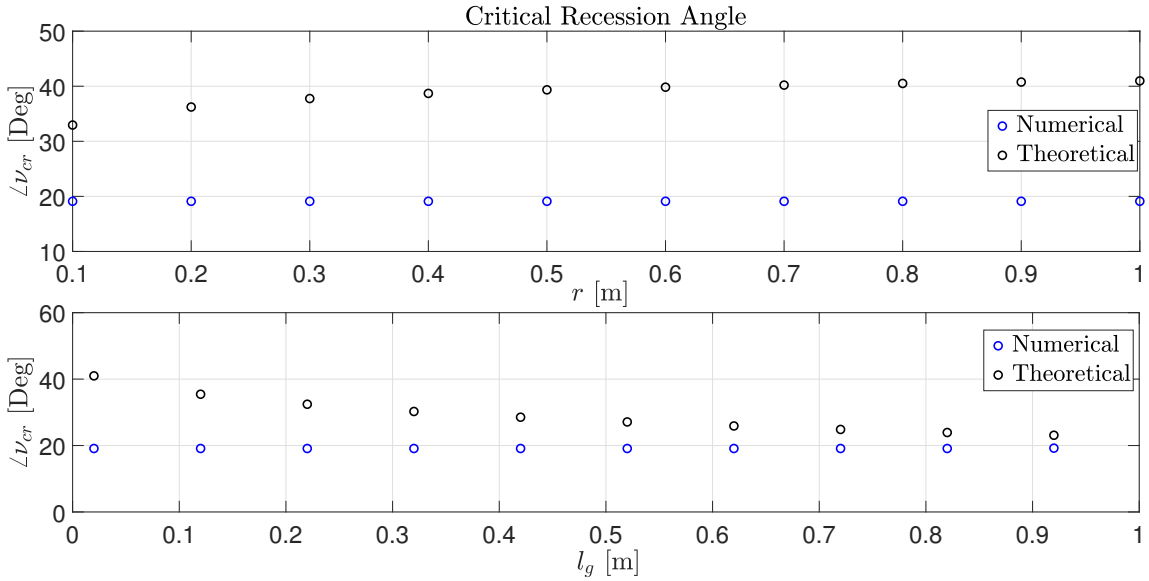

Figure 5.9: Critical image recession angle for a range of disk PPA radii and air-gap lengths.

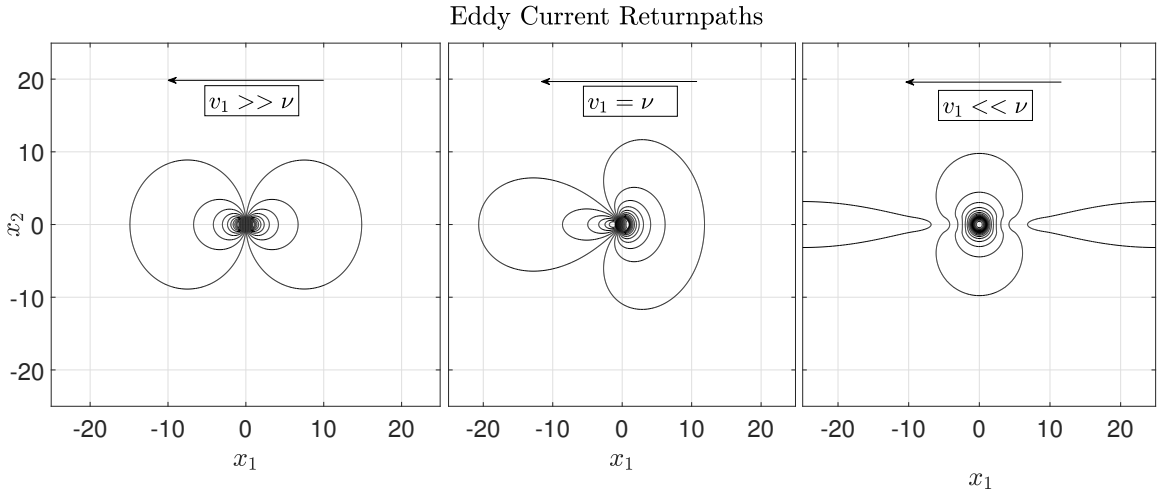

Figure 5.10: Stationary eddy current return paths for various sheet velocities and a disk PPA.

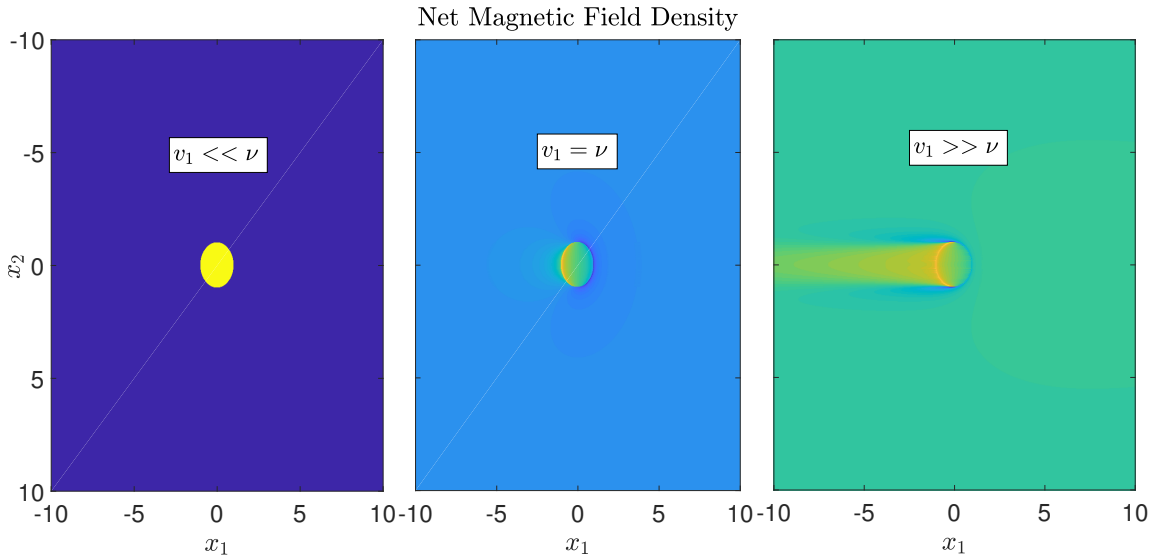

Figure 5.11: Net magnetic fields for various sheet velocities and a disk PPA.

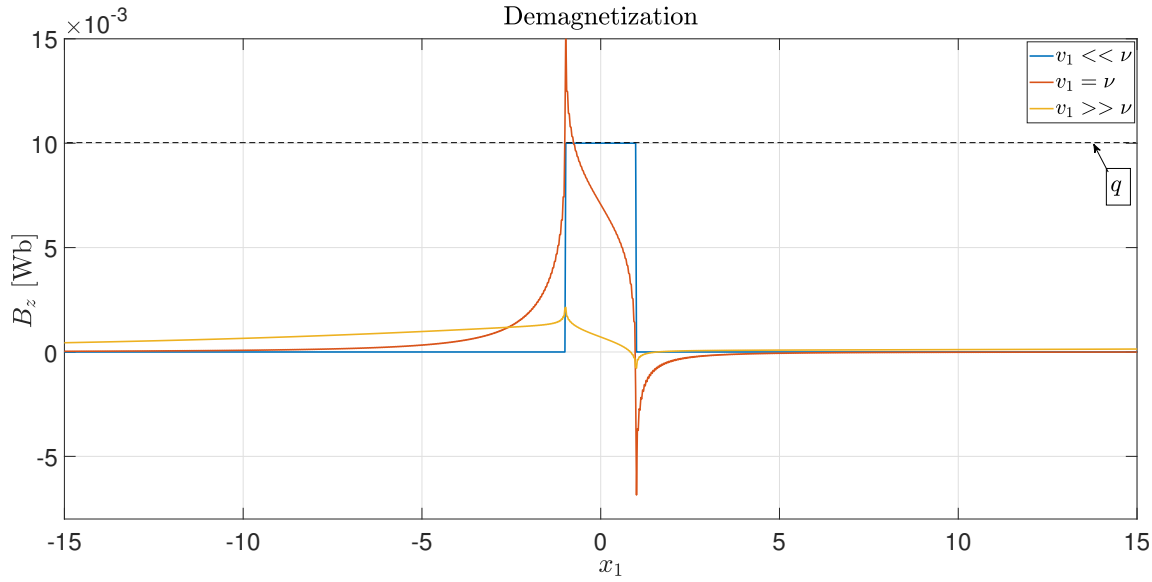

Figure 5.12: Transverse cross-section of the net magnetic fields for a disk PPA.

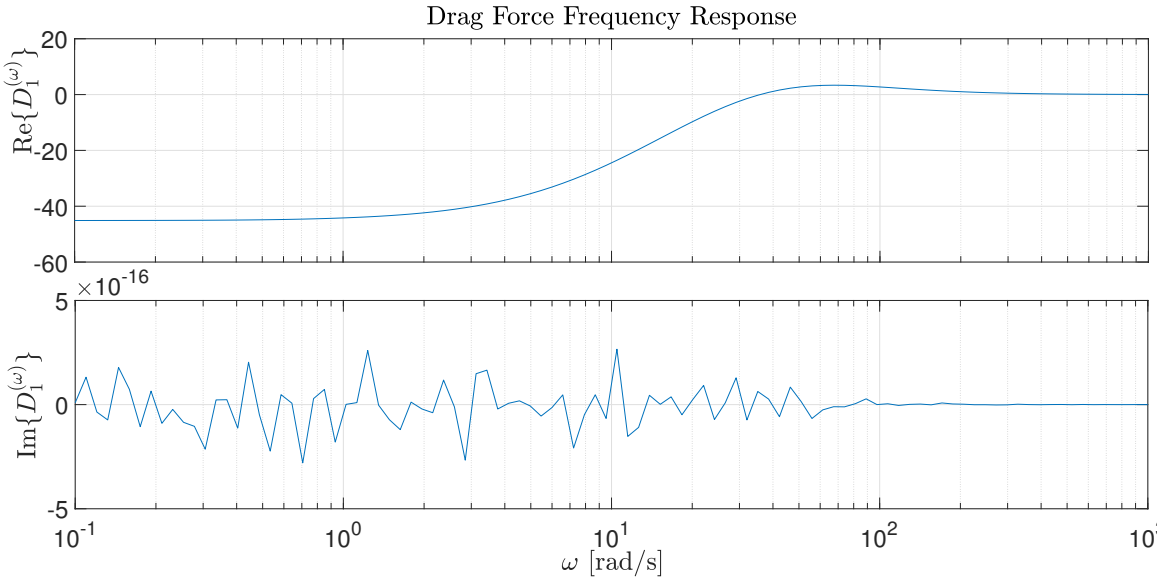

Figure 5.13: Real and imaginary parts of the drag force frequency response.

5.3 Dynamic Analysis Results

$D_1^{(\omega)}$ seems to be entirely real-valued (Figure 5.13), as the values of the imaginary part corresponds to the numerical error of the FFT. Hence, the frequency response of the ECB has zero phase, and its magnitude is contained in its real part. This is expected due to the T-symmetry of the ECB force vector (5.18), and agrees with the findings in (Section 5.1.2). This property is found to be consistent regardless of sheet velocity, pole shape, and sampling grid design.

We observe (Figure 5.14) that the bandwidth frequency ω_b of our solution increases with the sheet velocity. This means that the response time of the ECB is reduced for higher velocities, and the range of input frequencies that result in a stationary response of the drag force increases. Clearly, considerations on the frequency response of the ECB should include the effect of the sheet velocity. The frequency/velocity response of the drag force was visualized in (Figure 5.15-5.16). The frequency response of the ECB can be classified as a sort of zero-phase low-pass filter with a damped ripple effect in its stop-band.

We also find that the bandwidth frequency is higher for the monopole configuration than for the disk and rectangle PPAs. Judging by the slightly lower bandwidth of the rectangular PPA, which area is equal to $4r^2$ compared to the disk PPA with area πr^2, the bandwidth seems to be related to the size of the PPAs and not their shape.

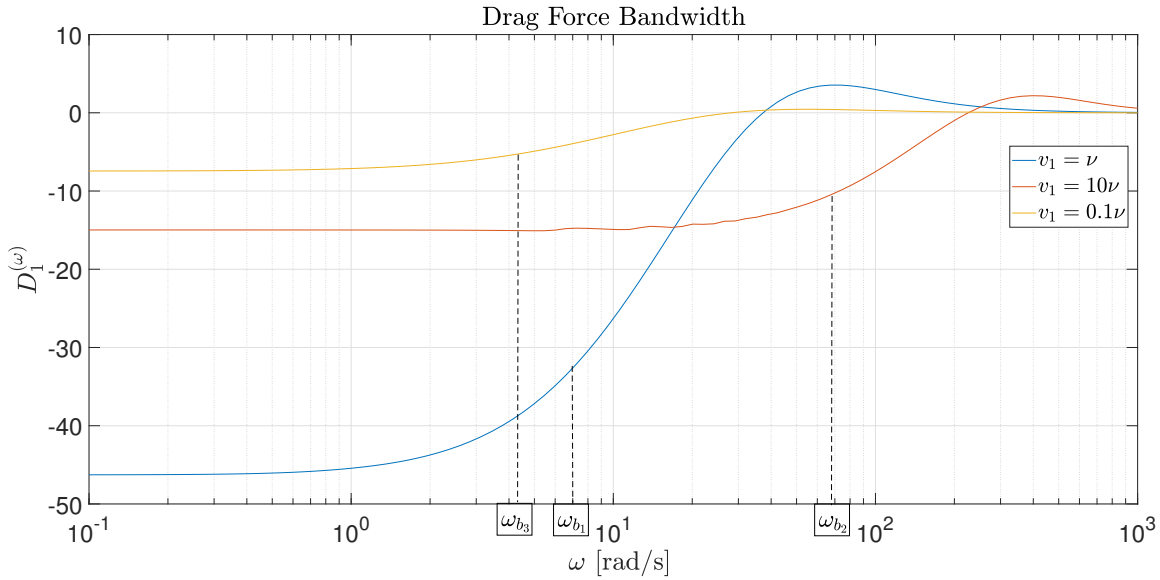

Figure 5.14: Drag force frequency response for various sheet velocities showcasing its impact on the bandwidth.

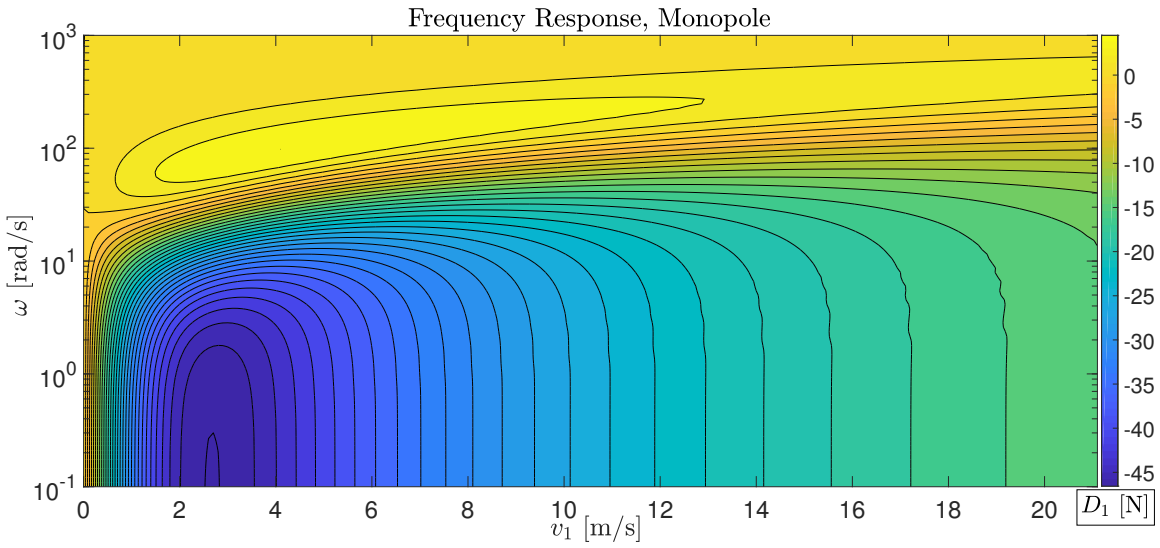

Figure 5.15: Contour plot of the frequency/velocity response of the drag force with a monopole at $h = 0.10\text{m}$.

Karakoc et al[26] investigated the effect on the ECB braking torque for alternating controlled magnetic fields. It was found that for low frequencies, a higher braking torque than

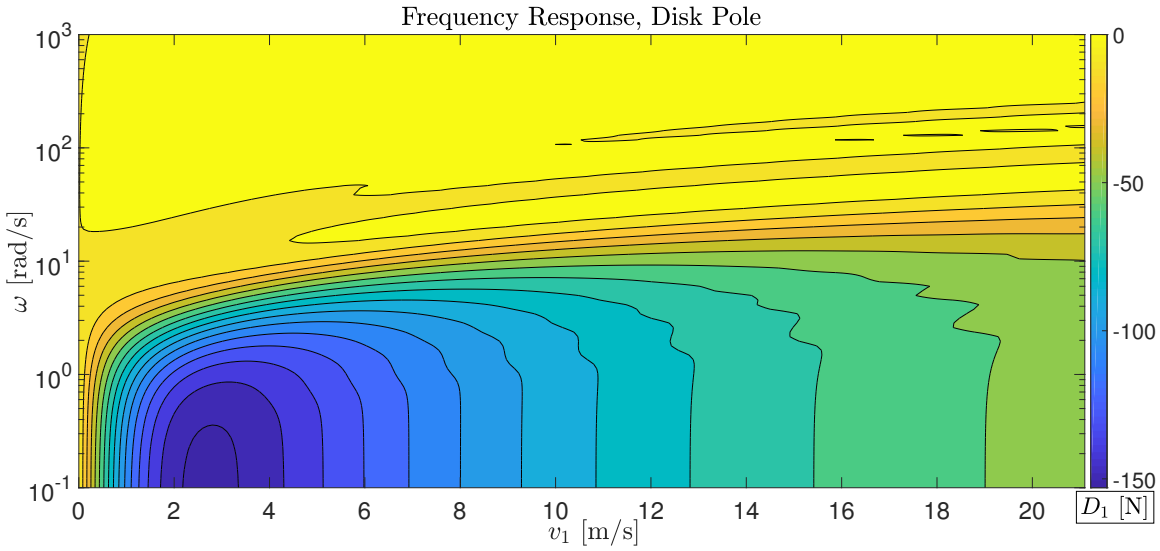

Figure 5.16: Contour plot of the frequency/velocity response of the drag force with a disk PPA of $r = 1.00\text{m}$.

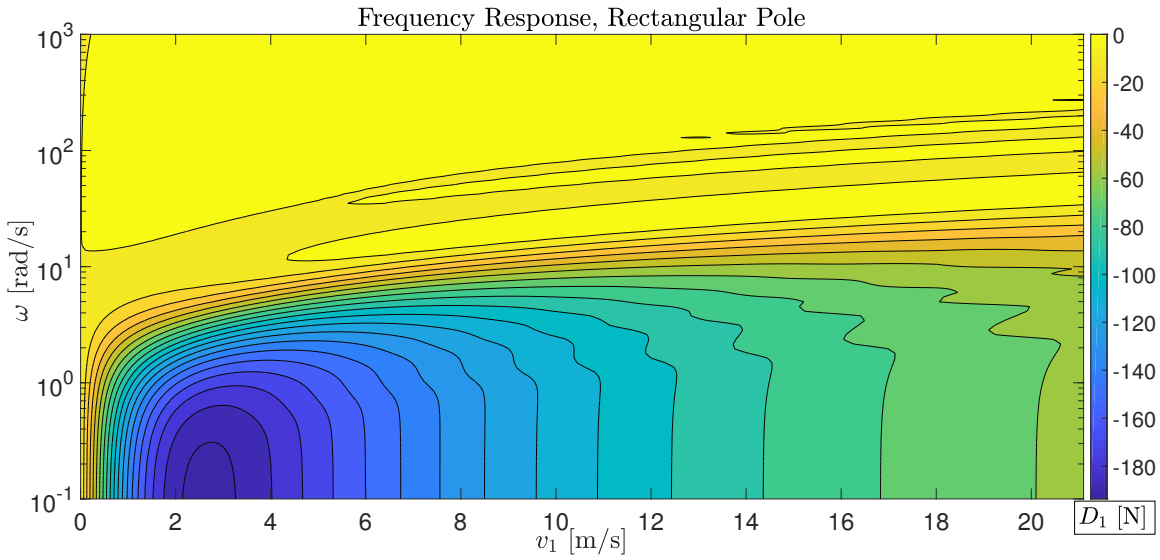

Figure 5.17: Contour plot of the frequency/velocity response of the drag force with a rectangular PPA of $r = 1.00\text{m}$.

that of the stationary controlled field can be generated. This is not reflected in the magnitudes of the frequency responses presented in this section, however - as we would expect to see some manner of resonance peak in the low region of the frequency response. We

instead observe that for slowly varying inputs, the magnitude of the drag force response is equivalent to the stationary response. [26] also found that for input frequencies above a certain threshold, the resulting braking torque decays to zero. This agrees with the findings in (Figure 5.14-5.17).

Perhaps the most interesting finding, although not particularly useful at first inspection, is the existence of frequency and velocity combinations that yield a small accelerating "drag" force in positive x_1 direction (Figure 5.14-5.15) due to the ripple. Cross-validation with disk, (5.16) and rectangle (5.17) shaped PPAs shows that this is consistent - although it is weaker (relatively) for the latter configurations. This property would permit the propulsion of a moving (no ripple effect for zero velocity) conductive body exclusively through the use of an external, vertical magnetic field oscillating at just the right frequency. The highest peak in (Figure 5.15) illustrates the relationship between the propelling input frequency and the sheet velocity. This phenomenon was also observed in [27], where certain AC frequencies of the controlled fields lead to an angular acceleration of a conductive disk. While the scope of the figure seems to show that the sheet can be accelerated indefinitely by choosing input frequencies according to the curve of this peak, further investigation into the high frequency/velocity range shows that as the braking force magnitude decays, so does the magnitude of the ripples. While the accelerating force seems insignificant, it is currently used for acceleration in linear magnetic levitation applications.

5.4 Time Discretization and Simulation

On top of the spatial discretization for the spectral method, time-stepping by a *sampling time* Δt is necessary in order to implement the dynamical ECB model. The continuous net magnetic field dynamics (3.52) are discretized in time as follows:

$$\begin{aligned} &\frac{\partial}{\partial t}\hat{B}_z(t) = A\hat{B}_z(t) + B\hat{C}_z(t) \\ &\qquad\Downarrow \\ &\hat{B}_z[j+1] = F\hat{B}_z[j] + G\hat{C}_z[j], \;\; j = \{0,1,2,...\} \end{aligned} \tag{5.23}$$

Where discrete-time system and control matrices F and G are given by:

$$\begin{aligned} F(\mathbf{k}) &= e^{A\Delta t} = e^{(ik_1v_1 - \nu|\mathbf{k}|)\Delta t} \\ G(\mathbf{k}) &= \left(\int_0^{\Delta t} F d\tau\right) B = \frac{1}{A}(F-1)B = \frac{(e^{(ik_1v_1-\nu|\mathbf{k}|)\Delta t}-1)\nu|\mathbf{k}|}{ik_1v_1 - \nu|\mathbf{k}|} \end{aligned}$$

Function values at discrete time values T can be interpolated by the relation:

$$\hat{f}_p[T] = \hat{f}[j\cdot\Delta t], \;\; T = \{0, \Delta t, 2\cdot\Delta t, ...\}$$

The penultimate dynamical model, discrete in time and space, for the ECB drag force simulations reads:

$$\hat{B}_z[\mathbf{K}, T+\Delta t] = F[\mathbf{K}]\hat{B}_z[\mathbf{K},T] + G[\mathbf{K}]\hat{C}_z[\mathbf{K},T] \tag{5.24a}$$

$$\hat{\psi}[\mathbf{K},T] = \frac{1}{b\mu_0|\mathbf{K}|}\hat{B}_z[\mathbf{K},T] \tag{5.24b}$$

$$D_1[T] = \frac{2b}{L_1L_2}\sum_{K_1}\sum_{K_2}\hat{\psi}^*[\mathbf{K},T](-iK_1\hat{B}_z[\mathbf{K},T]) \tag{5.24c}$$

Similar to the sampling grid design (Section 5.2), choosing the sampling time Δt is a non-trivial problem. In particular, Δt is desired to be small enough to avoid aliasing, but large enough to avoid unnecessarily slow simulations. The frequency response analysis (Section 5.3) gives us a good idea of the significant frequencies contained in the output D_1, and consequently the sampling time required to capture these. For a realistic range of sheet velocities, we find according to the Nyquist sampling theorem that a sampling frequency of

$$\frac{1}{\Delta t} > 2\cdot 2\pi\cdot 10^3 \text{rad s}^{-1} \tag{5.25}$$

is sufficient to include not only the drag force bandwidth, but also the significant ripple effects in its stop-band.

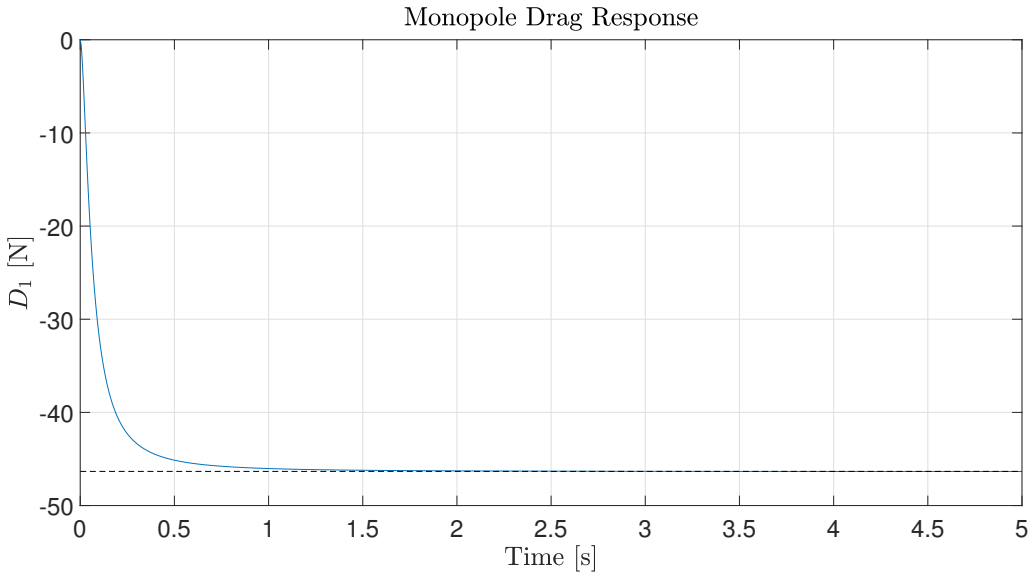

Figure 5.18: Drag force time-series for a monopole at $h = 0.10\text{m}$.

5.4.1 Simulation

Choosing the same system parameters as in the stationary and dynamical analyses according to (Table 5.1), a few simulations are executed in order to validate that the time-stepped dynamics behave as expected. In particular, we expect to see the drag force simulations converge to stationary values agreeing with static models with time constants given by the sheet velocity, that an accelerating output can be generated for certain combinations of sheet velocity and input frequency (Section 5.3), and that the phase error between a reference signal and the output drag force will be zero.

The step response transient of the time-stepped drag force solution is presented in (Figure 5.18 and 5.19) for the monopole and disk pole configurations, respectively. For both cases we find that the stationary behaviour of the discrete dynamical solution agrees with the findings in (Section 5.2). Likewise, the sheet velocity has a clear impact on the response time (Figure 5.19), agreeing with the dynamical analysis (Section 5.3). The reduced stationary value for higher velocities makes it seem like the velocity has a more dramatic impact on the response time than in reality. Still, (Figure 5.14 and 5.19) show a definitive connection between the response time and the sheet velocity.

While the drag force time-series seems like a first-order response for smaller sheet velocities (Figure 5.19), we observe periodic and damped dips in the drag force magnitude

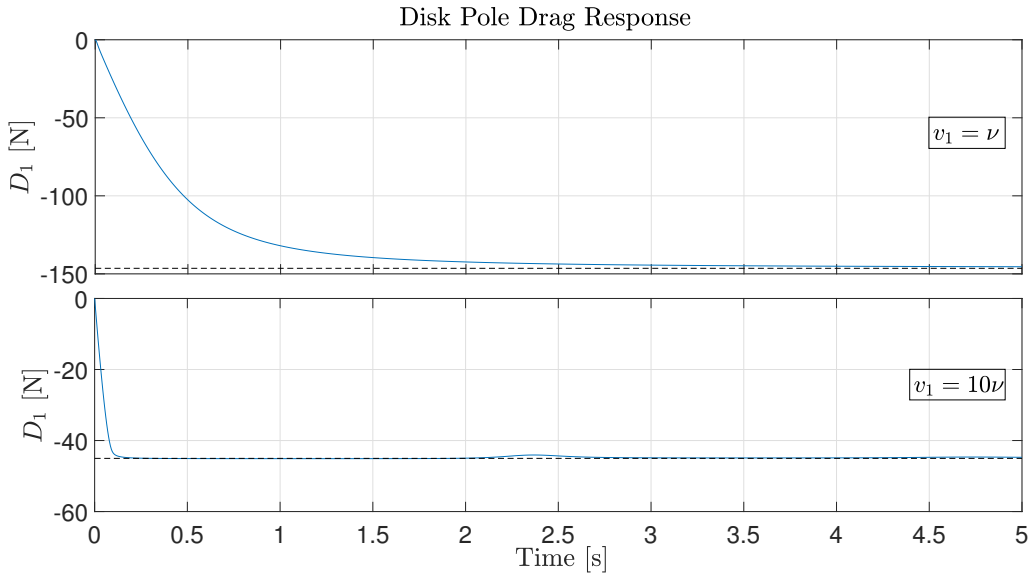

Figure 5.19: Drag force time-series for a pair of sheet velocities, with a disk shaped PPA.

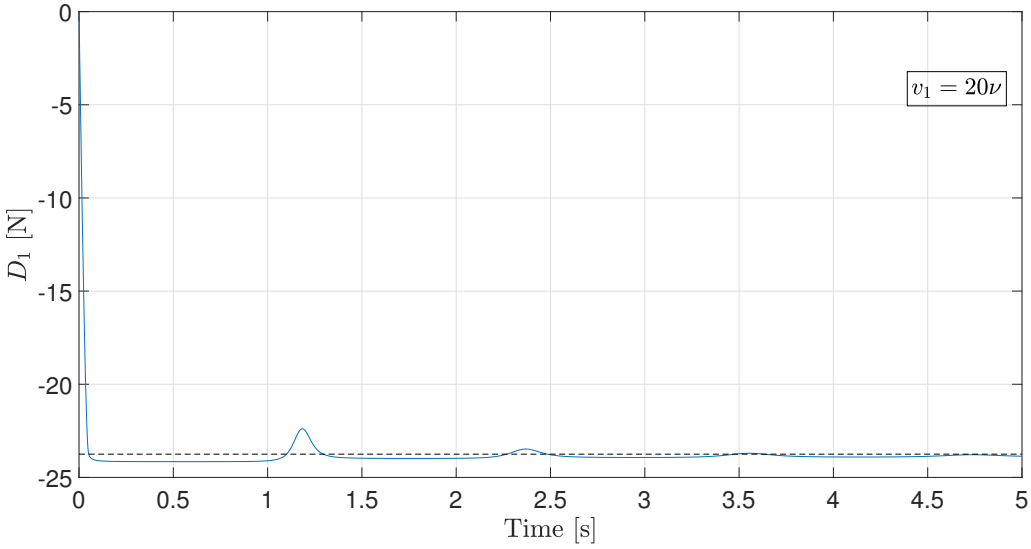

Figure 5.20: Periodic "dips" in the drag force transient.

for high sheet velocities (Figure 5.20). This behaviour is caused by the periodicity of the solution, as induced fields and currents return to the PPA before fully decaying - and grows more significant for larger v_1. For the latter time-series we have a sheet length of $L_1 = 50\text{m}$, and a velocity of $v_1 = 20\nu \approx 42.22\text{m s}^{-1}$. Thus we can see that each dip coincides with

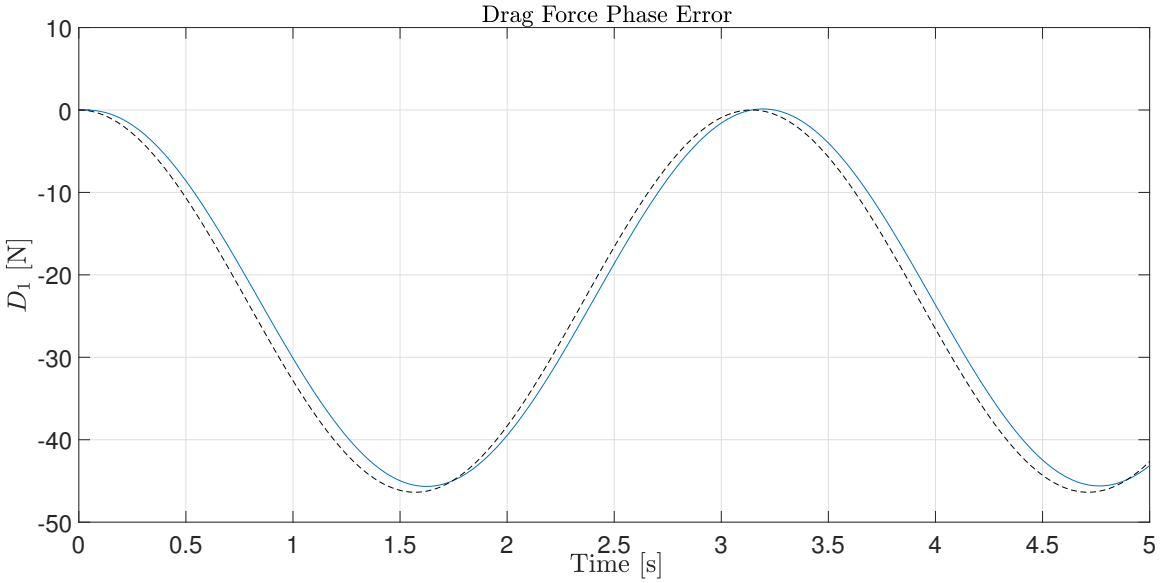

Figure 5.21: Phase comparison between the solution and the reference signal corresponding to input $q(t) = 0.01\sin(t)$ for a monopole configuration at $h = 0.10\text{m}$.

the period for a volume element to move one "cycle" of length L_1:

$$t_n = \frac{nL_1}{v_1} \approx n \cdot 1.18\text{s}, \quad n = 1, 2, 3 \ldots \tag{5.26}$$

While it is an unphysical result for linear (non-periodic) applications, this property of our solution could prove useful for rotating systems where this behaviour is present. Despite this behaviour, we observe that the time-series converge to their expected values, but take a longer time to settle.

We can see from (Figure 5.21) that the zero-phase findings in (Section 5.1.2 and 5.3) are not supported by the time-stepped solution. The solution lags behind the reference signal corresponding to a slowly varying sinusoidal input with a constant phase error. Time-stepping is known to introduce phase errors, but reducing the sampling time to values as low as $\Delta t = 10^{-5}\text{s}$ had no impact on the phase error.

Extracting the stream-function at a few time instances during the drag-force transient (Figure 5.19) for $v_1 = \nu$, and plotting its contours (Figure 5.22), we uncover the transient behaviour of the eddy current return paths in the plane - approaching the stationary shape shown in (Figure 5.10).

A monopole configuration was implemented with sinusoidal field strength oscillation at

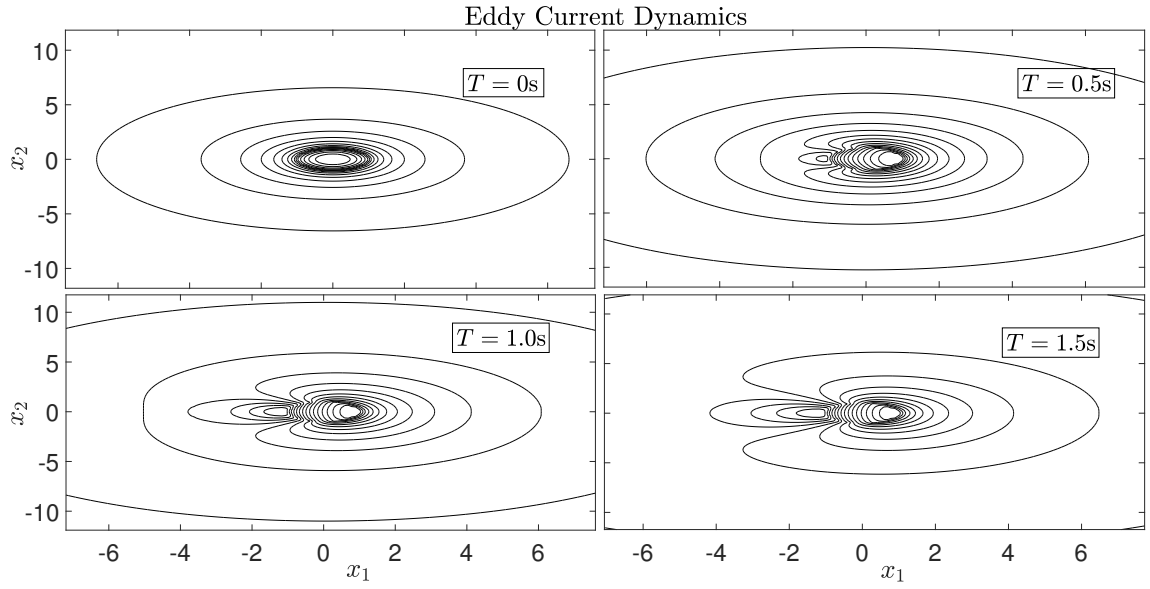

Figure 5.22: The eddy current dynamics corresponding to the low-speed ($v_1 = \nu$) step-response in (Figure 5.19).

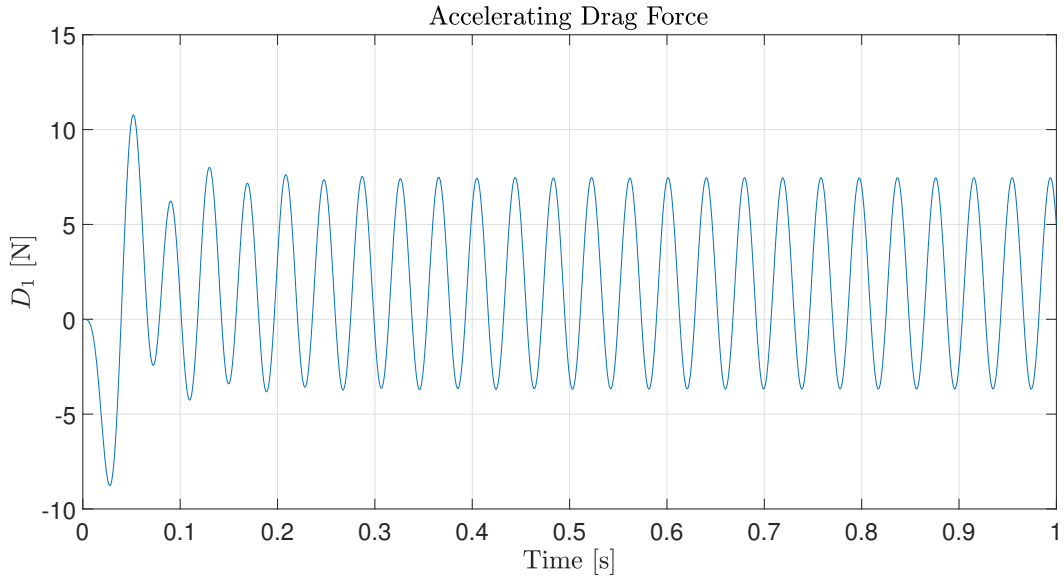

Figure 5.23: For a monopole with strength given by $q(t) = 0.01\sin(80t)$, the drag force output of the ECB is net positive for a fixed sheet velocity $v_1 = \nu$.

an accelerating frequency for $h = 0.10$m and $v_1 = \nu$ according to (Figure 5.15). The result (Figure 5.23) shows that the time-stepped solution validates the findings in (Section 5.3)

- the solution may produce a small force of propulsion with an oscillating magnetic field perpendicular to the movement of a conductor.

Chapter 6

Engineering Applications

In this chapter, a few applications for which our model is well suited are demonstrated briefly: Due to its ease of implementation, efficiency and accuracy, we look into the possibility of using the model for development and optimization of control methods and configurations for real world ECB systems.

6.1 ECB Controller Design

For the following engineering applications of the ECB model, all parameters are given by (Table 6.1) unless otherwise stated. Key changes include the reduction of the sheet dimensions and PPA size to a more realistic scale, and the exclusive use of disk shaped PPAs.

State of the art real time automatic control of the output force of ECB systems is generally limited to the approximate, stationary drag force models presented in (Section 2.3) paired with robust control methods. This limitation is caused by (*i*) FEM numerical solutions are far too slow to be utilized in real time applications, (*ii*) the input/output nonlinearity

$$D_1 \propto |q|^2 \tag{6.1}$$

complicates controller design as the braking force magnitude can only be reduced passively.

We can summarize the literature study on real time control of ECBs conducted in [2] as follows: Optimal torque control of an ECB mechanism on the wheel(s) of ground vehicles minimizing braking distance was investigated by Lee and Park [28], followed by Anwar

Parameter	Value	Comments
μ_0	$4\pi \times 10^{-7}\text{Wb}\,(\text{A m})^{-1}$	Vacuum permeability
μ	$\simeq 4\pi \times 10^{-7}\text{Wb}\,(\text{A m})^{-1}$	Aluminium sheet permeability
σ	$3.77 \times 10^{-7}\text{S m}^{-1}$	Aluminium sheet conductivity
d	$2.00 \times 10^{-2}\text{m}$	
r	$1.00 \times 10^{-2}\text{m}$	PPA radius for non-monopole configurations
a/b	1.00	Equal axial scaling of the PPA shapes
$\mathbf{x}_0$	$[0.00\text{m}\ \ 0.00\text{m}]^\intercal$	Single PPA placement
$\mathbf{x}_0^-$	$[-1.25r\ \ 0.00\text{m}]^\intercal$	Trailing adjacent PPA placement
$\mathbf{x}_0^+$	$[1.25r\ \ 0.00\text{m}]^\intercal$	Leading adjacent PPA placement
τ_q	$1.00 \times 10^{-2}\text{s}$	First order actuator time constant
q	$1.00 \times 10^{-2}\text{Wb}$	
h	0.00m	
c	0.50	Compensation factor for non-monopole PPAs centered on infinite surface (2.15)
$\angle\boldsymbol{\nu}$	45^o	Fixed speed $v_1 = \nu$
(L_1, L_2)	$(5.00\text{m}, 8.00\text{m})$	Sheet dimensions
(N_1, N_2)	$(2^{10}, 2^{10})$	
Δt	$1.00 \times 10^{-4}\text{s}$	

Table 6.1: Mathematical constants and parameters used for the ECB system during demonstration of engineering applications.

and Zheng [29]. These publications investigate the use of ECBs in *Anti-lock Braking Systems* (ABS) applications. Song [30] investigates the use of ECB for control of the angular motion of rotating disks, and proposes a hybrid hydraulic-ECB - due to the low braking force output of the ECB at low speeds. [28–30] share a similar approach to ECB control. Variants of the linear drag force model (5.7) were used as approximate braking force models in conjunction with a robust discontinuous control algorithm - the *Sliding Mode Controller* (SMC). Good reference torque tracking is consistent for each of the three publications, as well as performance issues associated with the control algorithm.

On the other hand, E. Simeu and D. Georges [31] successfully designed and implemented a continuous feedback linearization control algorithm based on a modification of (5.7) to include magnetic hysteresis, which combined with state/parameter estimation yielded quite good experimental results while bypassing the drawbacks of the discontinuous controller used by [28–30].

Linear motion braking force control was investigated by Hong-Je et al.[32], supplementing the 2D finite element analysis conducted in the same publication. Near constant brake force control was achieved experimentally using only a linear feedback controller (PI).

We proceed by showing that these state of the art control algorithms can be implemented in the ECB simulation with ease, motivating its use as a digital test-bed for design of the control law $q(t)$.

6.1.1 Electromagnet Actuator

In the vast majority of the work done on real-time control of ECBs, the manipulated variable is a command voltage $u(t)$ for an electromagnet (RL)-circuit generating $q(t)$. This electrical actuator can be described by the following first order dynamical system:

$$\frac{d}{dt}i(t) = \frac{1}{L_e}\left(-R_e i(t) + u(t)\right) \tag{6.2}$$

With time-constant given by its electrical inductance L_e and resistance R_e:

$$\tau_{RL} = \frac{L_e}{R_e} \tag{6.3}$$

The controlled field strength $q(t)$ can be calculated from the idealized electromotive force and reluctance for an inductor that has N_e windings around a core of length l_c of some ferromagnetic material:

$$q(t) = \frac{\mathcal{F}}{\mathcal{R}} = \frac{N_e i(t)}{l_g}\pi r^2 \tag{6.4}$$

Where the total reluctance is given by:

$$\begin{aligned}\mathcal{R} &= \mathcal{R}_{core} + \mathcal{R}_{gap} + \mathcal{R}_{sheet} \\ &= \frac{l_c}{\mu_c A_{PPA}} + \frac{l_g - d}{\mu_c A_{PPA}} + \frac{d}{\mu_0 A_{PPA}} = \frac{l_g}{\mu_0 \pi r^2}\end{aligned}$$

Where the core permeability μ_c is assumed much larger than μ_0, and fringing effects are neglected such that all cross-sectional areas are equal to the pole projection area of πr^2. The electromechanical models describing the ECB used in the relevant literature is essentially quasi-static, due to the braking force being assumed static apart from a small, electrical time-constant Due to the only ECB dynamics being considered in the literature is that of the electrical circuit controlling the external magnetic field, a quasi-static electromechanical model for the ECB is implied. Noting that this time-constant is significantly smaller

than what we observe in the frequency response analysis (Section 5.3) and in simulations (Section 5.4), and that simulation of (6.2) puts extremely high requirements on the sampling frequency, we choose to consider the controlled field strength $q(t)$ a static variable that we can control directly. It is also reasonable to assume that an outer control-loop ensuring that $q(t)$ follows its trajectory by a robust control algorithm such as the SMC, eliminating the effects of magnetic hysteresis and other uncertainties, will still be significantly faster than the inner ECB loop.

Despite this simplification, we find it necessary to assign $q(t)$ some arbitrary first order dynamics in order to limit its rate of change and switching frequency in the case of the SMC:

$$\dot{q}(t) = -\frac{1}{\tau_q} q(t) + q_d(t) \tag{6.5}$$

Where $q_d(t)$ is the desired input.

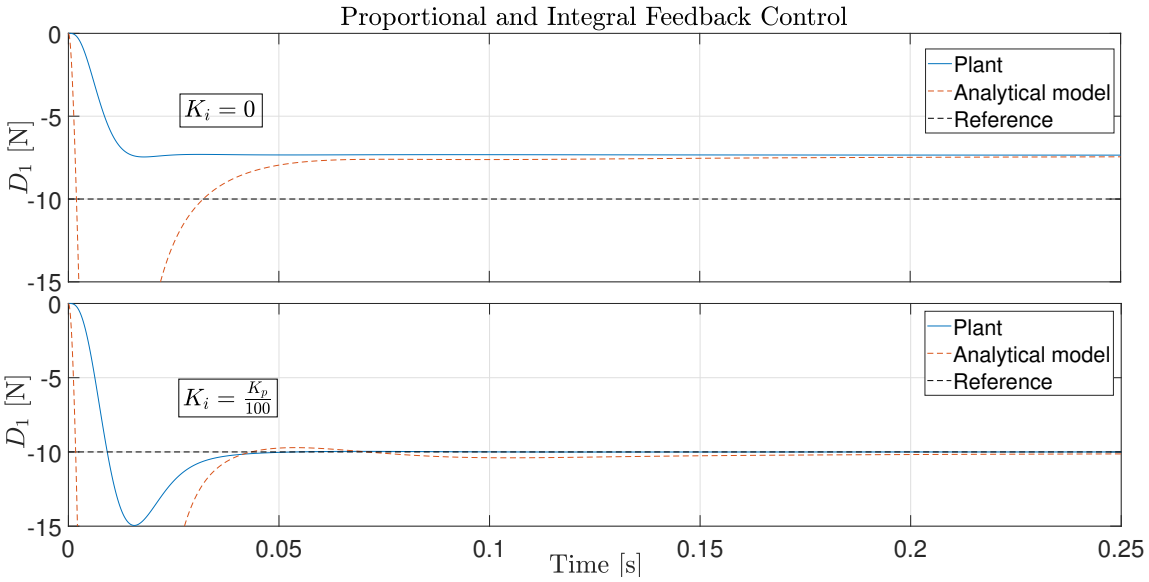

Figure 6.1: Reference tracking comparison for P-, and PI-Controllers. $K_p = 0.05$.

6.1.2 Linear Feedback Control

In general, a scalar state feedback controller is given by,

$$u(t) = -kx(t) \tag{6.6}$$

where the state $x(t)$, if governed by a linear dynamic system, can be replaced by the reference tracking error

$$\tilde{x}(t) = x_d(t) - x(t) \tag{6.7}$$

thanks to the superposition principle. Definition of the root output feedback error,

$$\tilde{y}(t) = \sqrt{|D_{1_d}(t)|} - \sqrt{|D_1(t)|} \tag{6.8}$$

permitted the use of linear feedback control algorithms for simulations of quasi-static ECB models in [2], and proportional feedback control was successfully implemented. A simple P-controller was implemented in order to validate the applicability of linear proportional control schemes for the numerical solution. In [32] a *Proportional Integral* (PI) controller was implemented and shown to perform well, we expect to see the same for the numerical implementation. The PI control law is defined by:

$$q_d(t) = K_p\tilde{y}(t) + K_i \int_{t_0}^{t} \tilde{y}(\tau)d\tau \tag{6.9}$$

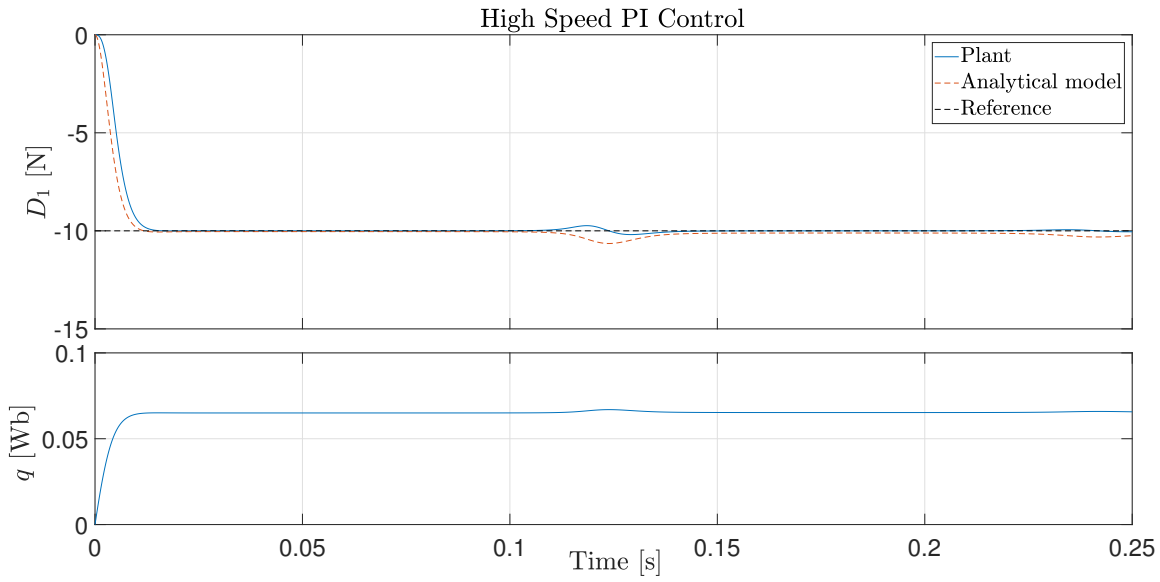

Figure 6.2: PI reference tracking for high sheet velocity, $v_1 = 20\nu$.

The proportional feedback control performance (Figure 6.1) was unsatisfactory, with significant stationary deviation for the given P-gain. We were able to put the numerical solution closer to the reference by increasing K_p, which was accompanied by a large overshoot. We conclude that, barring an error in our implementation, proportional output feedback control is not suitable for the dynamical ECB model despite the success in [2] for quasi-static models. The analytical drag force (5.9) is included to illustrate the difference of response times. The response time of the analytical model is given by τ_q (6.5), which in reality would be much smaller if given by τ_{RL}.

Unsurprisingly, we are able to eliminate the stationary deviation by adding a small integral action to our controller (Figure 6.1). The robustness of the integral action is illustrated in (Figure 6.2), where the same values of K_p and K_i lead to good performance well into the high speed region. The controller is able to reduce the effect of the dips in D_1 due to induced currents returning to the PPA before decaying, but is too slow to eliminate it completely. It is interesting to note that for higher velocities, the quasi-static model becomes a better approximation of the dynamical solution. This is because the response time of the ECB is reduced for higher sheet velocities, as noted in chapter 5, and eventually becomes faster than the first order dynamics of the controlled field. This result is misleading however, as (once again) the time constant of the actuator dynamics is much lower.

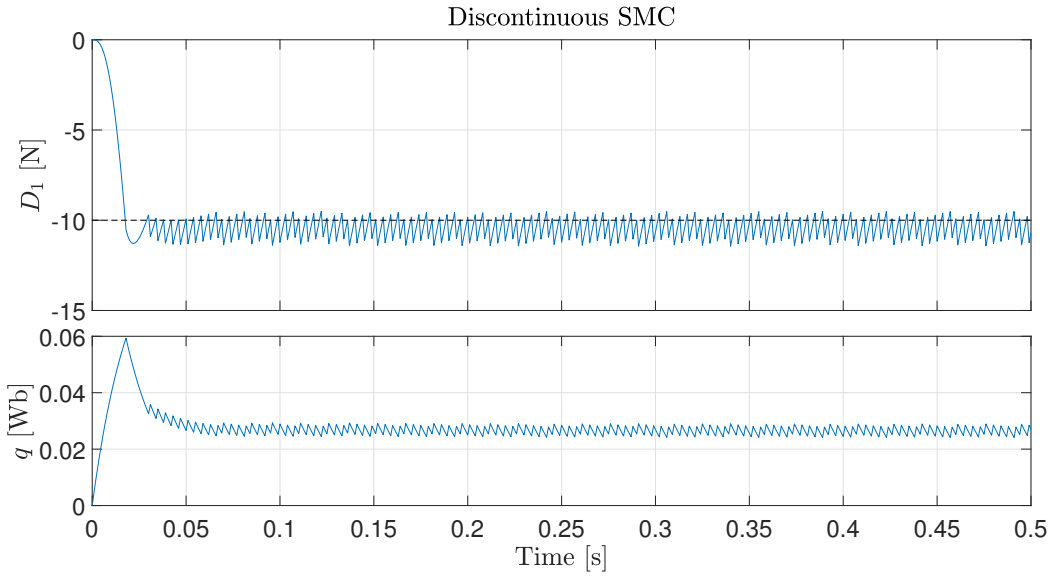

Figure 6.3: Performance of the discontinuous zeroth-order SMC. Gain $M = 0.5$.

6.1.3 Sliding Mode Control

Sliding mode control is well suited to electromechanical systems for its applicability to the switching of transistors in the circuit of a given actuator. For the root output feedback error (6.8), an n-order sliding variable is given (in accordance with [33, 34]) by:

$$s(t) = \left(\frac{d}{dt} + \lambda\right)^{n+1} \tilde{y}(t), \quad \lambda > 0 \tag{6.10}$$

A sliding *surface*, or sliding *mode* corresponds to the system behaviour when $s = 0$. For a first order SMC, this corresponds to the asymptotically stable output error dynamics:

$$\frac{d}{dt}\tilde{y}(t) = -\lambda\tilde{y}(t) \tag{6.11}$$

For which the system *slides* along the line

$$\frac{d}{dt}y_1(t) = y_2(t) = -\lambda y_1(t) \tag{6.12}$$

in the (y_1, y_2)-plane. This is achieved by the controller design:

$$u(t) = -M\text{sgn}(s), \quad M > 0 \tag{6.13}$$

Where M is a (relatively) large, bounded gain forcing the system towards the sliding surface from both sides. The first order SMC was used in [28, 29] to keep the system sliding

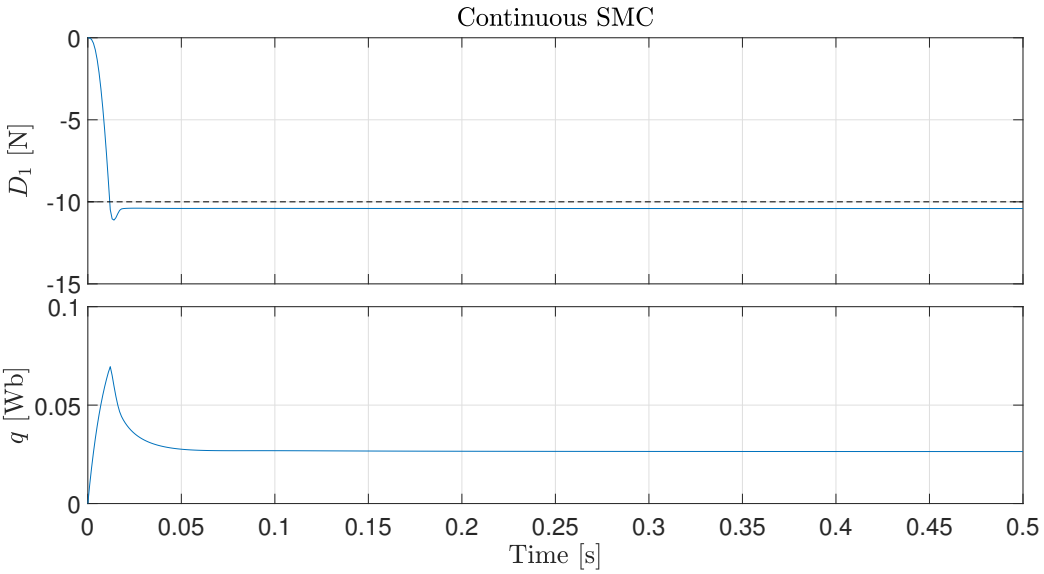

Figure 6.4: Reference tracking of the zeroth-order SMC using a logistic continuous approximation of the step-function. Sharpness $\alpha = 10$

along the surface corresponding to optimal slip-ratio. [29] also conducted a stability analysis of the ECB with a first order SMC, showing asymptotic stability. Note that these results are based on the quasi-static linear approximation (5.7) of the drag force. Based on experimental results in these publications it is reasonable to assume that the stability results in [29] also apply when the eddy current dynamics are introduced.

The discontinuous, switching nature of (6.13) in practice gives rise to an effect called *Chattering*. Chattering is caused by either physical (transistor) or numerical (sampling) limitations on the switching frequency, resulting in high frequency oscillations around $s = 0$. There exists a multitude of chattering prevention/reduction methods, one of which is simply increasing the order of (6.10).

We let a zeroth-order *On/Off*-SMC be given by:

$$s(t) = \tilde{y}(t) = \sqrt{|D_{1_d}(t)|} - \sqrt{|D_1(t)|} \tag{6.14a}$$

$$q_d(t) = -M\Theta(s) \tag{6.14b}$$

Where Θ is the discontinuous Heaviside step-function (4.11). The sign function of general SMC formulations is replaced by the unit-step function because of the inability of the controlled field to reduce the drag force magnitude by reversing the sign of the input. The discontinuous control law described by (6.14) was implemented in our ECB simulation

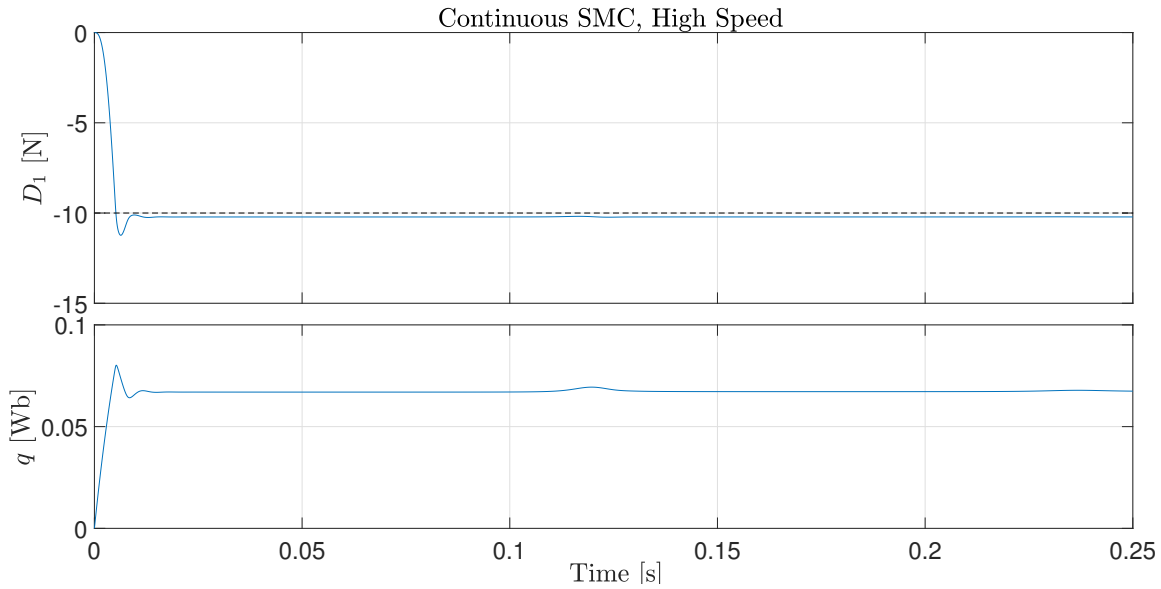

Figure 6.5: High speed ($v_1 = 20\nu$) reference tracking of the logistic SMC.

(Figure 6.3), as well as a continuous approximation using the logistic Heaviside approximation (4.14) as done in [2] (Figure 6.4).

For the discontinuous SMC response, there is a lot of chattering present despite (6.14) being essentially low-pass filtered through first order actuator dynamics. The system remains close to the sliding surface, however. Note that the chattering observed is an artifact of the limited sampling frequency of the numerical method, and that real world applications expect a smaller chattering amplitude due to a potentially higher maximum switching frequency of transistors - implying a system behaviour that slides closer to the sliding surface. Regardless, chattering is generally best avoided due to its damaging effect on actuators. Thus, we turn our attention to the results of the continuous SMC (Figure 6.4).

SMCs with continuous approximations are typically associated with a stationary error in the form of a band of acceptance around the sliding surface, with a width depending on the sharpness α of the approximating curve. This is why the system does not converge to the sliding surface in (Figure 6.4). Robustness of the SMC is demonstrated by time time-series (Figure 6.5), for unchanged gain and sharpness parameters. Unlike the integral action in (Section 6.1.2), the SMC is not associated with a time delay. This allows it to (nearly) eliminate the drag force reducing effect of the returning magnetic fields.

6.2 Pole Configuration and Optimization

Due to saturation effects in electromagnets, as well as heating issues in their circuits, a limited braking force can be generated by a single magnet. If one wants to increase the braking force of their ECB, there is an obvious solution: Add more magnets. The best way to arrange these magnets in space is less trivial, however. It is clear that two magnets placed in a vicinity of each other, and acting on a moving conductor, will induce magnetic fields that interfere with one another. We have already seen what happens to the braking force when the induced magnetic field returns to the PPA (Section 5.4), and similar effects are even more pronounced for numerous working controlled fields.

There is a limited body of work on the impact and optimization of electromagnet design and placement for ECBs. Karakoc et al.[26, 27] optimized the braking torque for a 4 PPA configuration on a rotating disk for many design parameters, including the angular distance between each pole and the frequency of their alternating fields. The torque values were computed using finite element analysis, and it was found that it is possible to place and synchronize a number of PPAs such that the generated torque is *stronger* than the theoretical torque of the same number of independent magnets.

As previously stated, our dynamical solution does not seem to agree with the existence of resonant input frequencies, but it is possible that this would change with the introduction of numerous poles. Due to the efficiency of the numerical method solving our ECB model, as well as the ease of manipulating PPA placements and shapes in the plane, it seems uniquely suited for this application - bypassing the slow FEM. The total controlled field can be expressed as a sum of n independently placed and controlled PPAs:

$$\mathbf{C}(\mathbf{x}, t) = \sum_{i=1}^{n} q_i(t)\mathbf{P}_i\left(\mathbf{x} - \mathbf{x}_{0_i}\right) \tag{6.15}$$

6.2.1 Motivating Example

We consider the controlled field of two disk shaped PPAs adjacently placed along the x_1-axis. Since they are placed along the axis of translation, we will refer to the one on the right hand side of the plane as the *leading* PPA, and the to the other as the *trailing* PPA. The uniform, vertical component of (6.15) with $n = 2$ is given by:

$$C_z(\mathbf{x}, t) = q^+(t)P^{disk}\left(\mathbf{x} - \mathbf{x}_0^+\right) + q^-(t)P^{disk}\left(\mathbf{x} - \mathbf{x}_0^-\right) \tag{6.16}$$

Where superscripts $^+$ and $^-$ refer to the leading and trailing PPAs, respectively. For simplicity, we consider only two cases: (*i*) the adjacent PPA fields are of equal, constant strength

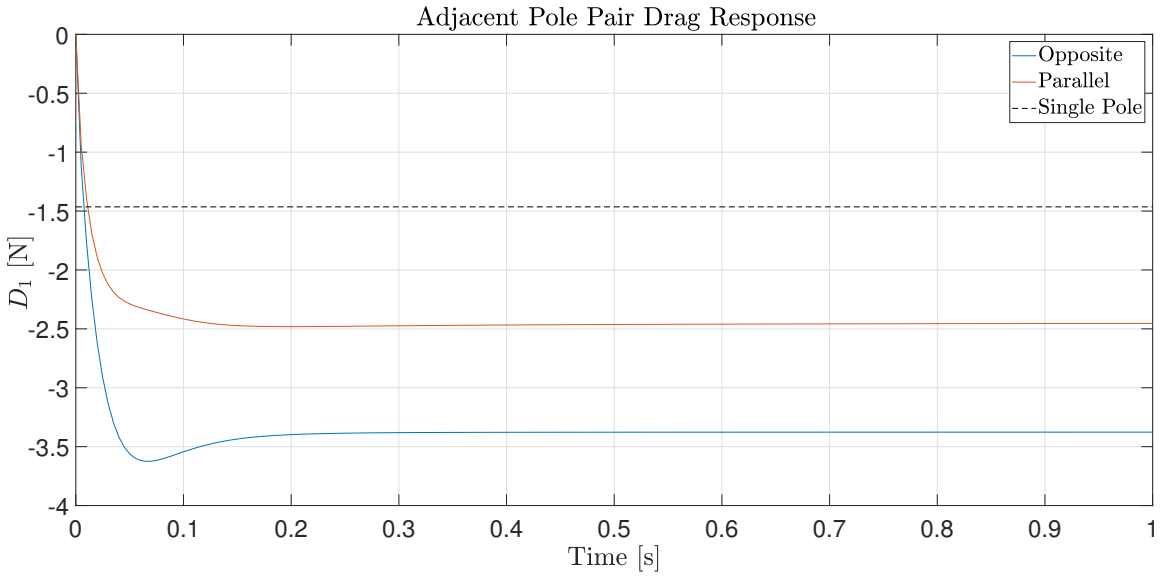

Figure 6.6: Drag force response comparison for the two adjacent pole configurations, with the stationary single pole response.

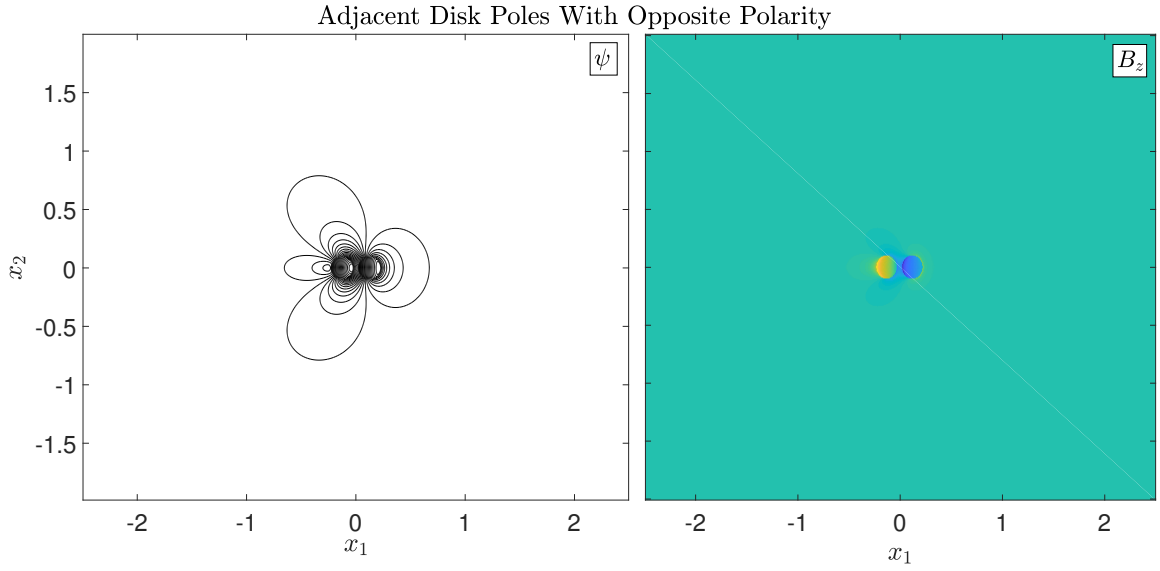

Figure 6.7: Eddy currents and net magnetic fields in the plane for adjacent opposing poles.

q and of opposite polarity, and (*ii*) the fields are of strength q and of parallel polarity:

$$q^+ = q = -q^-, \qquad (i)$$
$$q^+ = q = q^-, \qquad (ii)$$

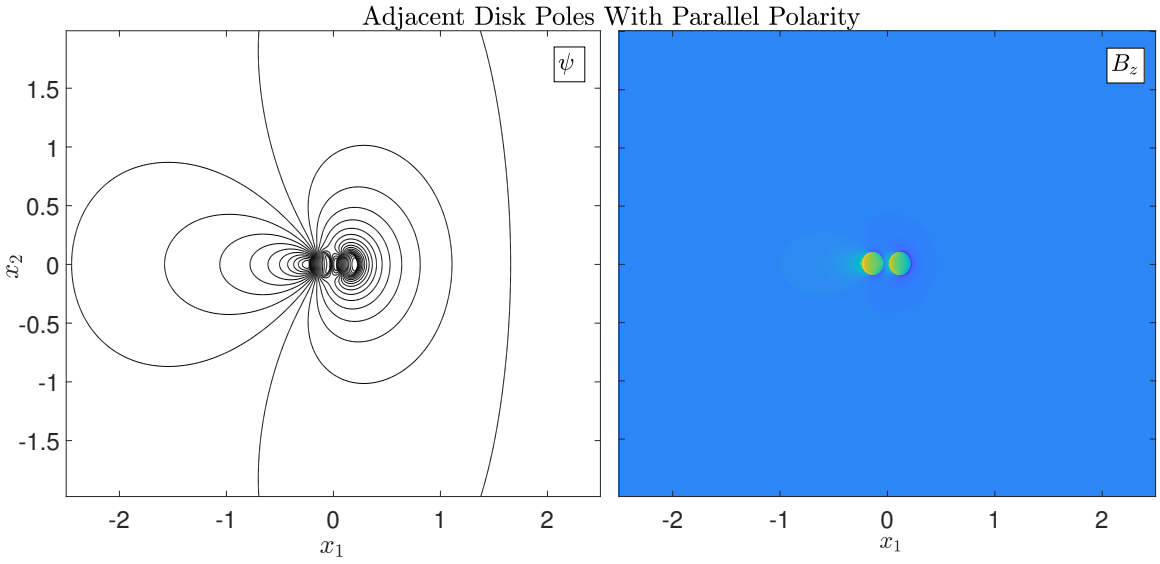

Figure 6.8: Eddy currents and net magnetic fields in the plane for adjacent parallel poles.

Simulation of the cases yielded the drag force responses in (Figure 6.6), where our main observations are: The adjacent PPAs of opposite polarity generate a braking force that is $\approx 15\%$ stronger than the theoretical force of two equivalent magnets placed far apart. Conversely, adjacent PPAs of parallel polarity resulted in a braking force that is $\approx 17\%$ weaker than two independent magnets. This is explained by the interaction of the eddy currents between the adjacent PPAs for the two cases (Figure 6.7 and 6.8). The volume elements leaving the leading PPA carry eddy currents and induced magnetic fields with the same polarity as the leading magnet, which in (*i*) opposes the field of the trailing magnet, and the volume elements experience a decelerating force of repulsion. In (*ii*), the opposite is true. The volume elements leaving the leading PPA are attracted to the trailing PPA, accelerating them.

Chapter 7

Conclusion

The objective of the research carried in the preceding chapters was, briefly put, to evaluate the merit of the analytical dynamical ECB model based on the FET. The spectral numerical realization of the fractional dynamical ECB model was shown to (mostly) agree with established results on the stationary behaviour of ECBs. Most importantly, the stationary behaviour is surprisingly close to that of Additionally, frequency analysis of the dynamical model granted insight into why alternating controlled fields of different frequencies lead to significant changes in the generated forces, which the stationary models can tell us nothing about. A few discrepancies in the solution were noted however: (*i*) Its critical recession angle in its stationary response is constant, instead of varying with the air-gap and size of the PPA as expected. (*ii*) Increased braking force generation for certain frequencies of alternating controlled fields is not supported by our findings. Nevertheless: For its ease of implementation, excellent convergence properties, and satisfactory numerical accuracy, one can argue that the detailed method bridges the gap between time consuming numerical methods (Finite Element Method), and approximate methods.

7.1 Further Work

There remains a multitude of topics to investigate for the presented ECB model and numerical solution. Some of which are:

- Experimental verification of the novel findings in the model analysis are warranted. In particular, we are interested in the accuracy of the response time of the solution, and if it truly reduces with increased sheet velocities.

- Analysis of the simulation execution time should be conducted in order to conclude whether or not the method is efficient enough to be used in real-time applications. The author observed potentially fast behaviour with an un-optimized script focused on error minimization. Optimization of the script running the simulation could allow for real-time applications of the numerical solution.

Bibliography

[1] J.C. Maxwell, *A Treatise on Electricity and Magnetism*. Oxford, England: Clarendon Press, 1873.

[2] L. Rudolfsen, "Modeling and control of eddy-current brakes", Project Thesis, NTNU, 2018.

[3] J.C. Maxwell, "On the induction of electric currents in an infinite plane sheet of uniform conductivity", *Proceedings of the Royal Society of London*, vol. 20, pp. 159–168, 1871 - 1872. DOI: 10.1098/rspl.1871.0038.

[4] A. Sommerfeld, "Über verzweigte potentiale im raum", *Proceedings of the London Mathematical Society*, vol. 28, pp. 395–429, 1897. DOI: 10.1112/plms/s1-28.1.395.

[5] R. Rüdenberg, *Energie der Wirbelströme in elektrischen Bremsen und Dynamomaschinen*, ser. Sammlung elektrotechnischer Vorträge. Verlag Enke, Stuttgart, 1906.

[6] J. Reitz, "Forces on moving magnets due to eddy currents", *Journal of Applied Physics*, vol. 41, no. 5, pp. 2067–2071, 1970. DOI: 10.1063/1.1659166.

[7] L. Davis and J. Reitz, "Eddy currents in finite conducting sheets", *Journal of Applied Physics*, vol. 42, no. 11, pp. 4119–4127, 1971. DOI: 10.1063/1.1659742.

[8] W. Smythe, "On eddy currents in a rotating disk", *Electrical Engineering*, vol. 61, no. 9, pp. 681–684, 1942. DOI: 10.1109/EE.1942.6436528.

[9] D. Scheiber, "Braking torque on rotating sheet in stationary magnetic field", *The Proceedings of the Institution of Electrical Engineers*, vol. 121, no. 2, pp. 117–122, 1974. DOI: 10.1049/piee.1974.0021.

[10] L. Davis, "Drag force on a magnet moving near a thin conductor", *Journal of Applied Physics*, vol. 43, no. 10, pp. 4256–4257, 1972. DOI: 10.1063/1.1660905.

[11] K. Lee and K. Park, "Modeling eddy currents with boundary conditions by using coulomb's law and the method of images", *IEEE Transactions on Magnetics*, vol. 28, no. 2, pp. 1333–1340, 2002. DOI: 10.1109/20.996020.

[12] J. Wouterse, "Critical torque and speed of eddy current brake with widely separated soft iron poles", *IEE Proceedings B (Electric Power Applications)*, vol. 138, no. 4, pp. 153–158, 1991. DOI: 10.1049/ip-b.1991.0019.

[13] W. Zimmermann, "Rechnung und versuch bei der scheibenförmigen wirbelstrombremse", *Archiv für Elektrotechnik*, vol. 10, no. 3-4, pp. 133–154, 1921. DOI: 10.1007/BF01578439.

[14] M. Pedersen, "Eddy current braking on thin sheets of infinite extent", Unpublished, 2019.

[15] Several Authors, *Fourier transform — Wikipedia, the free encyclopedia*, [Online; accessed 12-May-2019]. [Online]. Available: https://en.wikipedia.org/wiki/Fourier_transform.

[16] G. Arfken, H. Weber, and F. Harris, *Mathematical Methods for Physicists, Seventh Edition*. Waltham, Massachusetts: Academic Press, 2012.

[17] M. Pedersen, "Fractional inflow dynamics", *AHS Specialists' Conference on Aeromechanics Design for Transformative Vertical Flight*, pp. 66–78, 2018.

[18] C. Bucur and E. Valdinoci, *Nonlocal Diffusion and Applications*, ser. Lecture Notes of the Unione Matematica Italiana. Springer, 2016, vol. 20.

[19] J. Bigeon, J. Sabonnadiere, and J. Coulomb, "Finite element analysis of an electromagnetic brake", *IEEE Transactions on Magnetics*, vol. 19, no. 6, pp. 2632–2634, 1983. DOI: 110.1109/TMAG.1983.1062848.

[20] M. Hecquet, P. Brochet, L. Jin, and P. Delsalle, "A linear eddy-current braking system defined by finite element method", *IEEE Transactions on Magnetics*, vol. 35, no. 3, pp. 1841–1844, 1999. DOI: 10.1109/20.767391.

[21] M. Hofmannn, T. Werle, R. Pfeiffer, and A. Binder, "2d and 3d numerical field computation of eddy-current brakes for traction", *IEEE Transactions on Magnetics*, vol. 36, no. 4, pp. 1758–1763, 2000. DOI: 10.1109/20.877784.

[22] L. Trefethen, *Spectral methods in MATLAB*. SIAM, 2000.

[23] E. Hewitt and R. Hewitt, "The gibbs-wilbraham phenomenon: An episode in fourier analysis", *Archive for History of Exact Sciences*, vol. 21, pp. 129–160, 2 1979. DOI: 10.1007/BF00330404.

[24] S. Hyde, Z. Blum, T. Landh, S. Lidin, B. Ninham, S. Andersson, and K. Larsson, *The Language of Shape, First Edition*. Amsterdam: Elsevier, 1997.

[25] M. Frigo and S. Johnson, "Fftw: An adaptive software architecture for the fft", *Proceedings of the 1998 IEEE International Conference on Acoustics, Speech and Signal Processing, ICASSP '98 (Cat. No.98CH36181)*, vol. 3, pp. 1381–1384. 1998. DOI: 10.1109/ICASSP.1998.681704.

[26] K. Karakoc, E. Park, and A. Suleman, "Improved braking torque generation capacity of an eddy current brake with time varying magnetic fields: A numerical study", *Finite Elements in Analysis and Design*, vol. 59, pp. 66–75, 2012. DOI: 10.1016/j.finel.2012.05.005.

[27] ——, "Optimized braking torque generation capacity of an eddy current brake with the application of time-varying magnetic fields", *IEEE Transactions on Vehicular Technology*, vol. 64, pp. 1530–1538, 4 2014. DOI: 10.1109/TVT.2013.2286097.

[28] K. Lee and K. Park, "Optimal robust control of a contactless brake system using an eddy current", *Mechatronics*, vol. 9, no. 6, pp. 615–631, 1999. DOI: 10.1016/S0957-4158(99)00008-2.

[29] S. Anwar and B. Zheng, "An antilock-braking algorithm for an eddy-current-based brake-by-wire system", *IEEE Transactions on Vehicular Technology*, vol. 56, no. 3, pp. 1100–1107, 2007. DOI: 10.1109/TVT.2007.895604.

[30] J. Song, "Performance evaluation of a hybrid electric brake system with a sliding mode controller", *Mechatronics*, vol. 15, no. 3, pp. 339–358, 2005. DOI: 10.1016/j.mechatronics.2004.09.005.

[31] E. Simeou and D. Georges, "Modeling and control of an eddy current brake", *Control Engineering Practice*, vol. 4, no. 1, pp. 19–26, 1996. DOI: 10.1016/0967-0661(95)00202-4.

[32] R. Hong-Je, K. Jong-Soo, K. Do-Hyun, R. Geun-Hie, K. Yong-Ju, and W. Chung-Yuen, "Design and analysis of an eddy current brake for a high-speed railway train with constant torque control", *Conference Record of the 2000 IEEE Industry Applications Conference*, pp. 277–281, 2000. DOI: 10.1109/IAS.2000.881123.

[33] J.E. Slotine and W. Li, *Applied Nonlinear Control*. Englewood Cliffs, New Jersey: Prentice-Hall inc., 1991.

[34] H. Khalil, *Nonlinear Systems, Third Edition*. Englewood Cliffs, New Jersey: Prentice-Hall inc., 2002.